Numerical simulation of sensible and latent thermal energy storage systems.

Centre Tecnològic de Transferència de Calor
Departament de Màquines i Motors Tèrmics
Universitat Politècnica de Catalunya

Santiago Torras Ortiz
Doctoral Thesis

Numerical simulation of sensible and latent thermal energy storage systems.

Santiago Torras Ortiz

TESIS DOCTORAL

presentada al

Departament de Màquines i Motors Tèrmics
E.T.S.E.I.A.T.
Universitat Politècnica de Catalunya

para la obtención del grado de

Doctor por la Universitat Politècnica de Catalunya

Terrassa, December, 2015

Numerical simulation of sensible and latent thermal energy storage systems.

Santiago Torras Ortiz

Directores de la Tesis

Dr. Joaquim Rigola Serrano

Dr. Carles Oliet Casasayas

Dr. Jesús Castro González

Tutores

Dr. Carlos David Pérez-Segarra

Dr. Assensi Oliva Llena

Tribunal Calificador

Dr. Cristóbal Cortés Gracia
Universidad de Zaragoza

Dr. Antonio Lecuona Neumann
Universidad Carlos III de Madrid

Dr. Francesc Xavier Trias Miquel
Universitat Politècnica de Catalunya

A mis padres, Bella y Santiago,

a mi hijo, Sebastián y

y mi amada esposa, Maria Andrea.

Acknowledgements

Quisiera aprovechar este espacio para agradecer a todos aquellas personas que sin su apoyo este trabajo no hubiera sido posible.

Al profesor Assensi Oliva, director del Centro Tecnológico de transferencia de calor (CTTC), quien me dió la oportunidad de realizar los estudios de doctorado en dicho centro. Además, por su ayuda a lo largo de esto años y por su entusiasmo en todo lo que se realiza dentro del centro.

Al profesor Carlos David Pérez-Segarra, por su dedicación y entrega con la que trabaja, además de su guía en muchos aspectos de esta Tesis.

Al profesor Joaquim Rigola, por su orientación y supervisión en toda la Tesis, por su gran habilidad a la hora de organizar los tiempos y objetivos de dedicación de mi trabajo y también por motivarme continuamente y transmitirme entusiasmo en situaciones de inquietud. La ambición de este proyecto es en parte, mérito suyo.

Al profesor Carles Oliet, por sus valiosos aportes en esta Tesis, su orientación y sus ayudas varias, su rigurosidad para trabajar que muchos hemos sufrido y por introducirme y guiarme en el área experimental, además por su inestimable apoyo.

Al profesor Jesús Castro, por su dedicación y paciencia, así como por su conocimientos y experiencia, que le han permitido guiarme en el desarrollo del trabajo propuesto en la simulación numérica del prototipo del acumulador para sistema de propulsión criogénica.

Y porque es un lujo haberlos tenido como tutores y directores de Tesis.

Dentro del CTTC he tenido también la oportunidad de trabajar con gente muy talentosa. A Ivette Rodríguez y Oriol Lehmkuhl, les debo agradecer su orientación en puntos cruciales que han facilitado la obtención de resultados de esta Tesis. A Nicolas Ablanque, por su gran apoyo durante todos estos años de doctorado, su interés por cualquier duda que pudiera tener y por tener siempre un momento para ayudarme. Sergio Morales, por su gran apoyo y disposición para ayudarme en los modelos de flujo bifásico. Al Jordi Chiva y Guillermo Oyarzún por su valiosa ayuda en temas relacionados a la programación y son claves en este proyecto. A Guillem Colomer con quien compartí durante la elaboración de la interfase gráfica del STEScode. A Octavi y Ramiro por su inestimable ayuda con los problemas informáticos con mi computadora y el clúster. A Manolo, por su soporte y ayuda en el montaje experimental y su disposición para enseñar.

A mis compañeros de sala (la guardería), por donde han pasado muchas personas de diferentes nacionalidades y de quienes he aprendido siempre algo (Fei, Mohamed, Hamdi, Lluis, JoanF y muchos otros), pero en especial a lo que hemos compartido todo este tiempo juntos Nico y Alex, gracias por soportarme y darme su amistad. A mis compañeros de otras salas o nuevos de la guarderia: Deniz, Lalo, Hao, Eugenio, Juan, Hector, y Rash con quienes he disfrutados durante estos años.

Mis compañeros del café (Farnos, Calafa, López, Lluis y Aleix), que con todos estos años y grandes momentos compartidos como bodas, partidas de airsoft, fiestas, paseos, tertulias, hemos hecho una gran amistad, les doy gracias por saber escuchar y darme apoyo.

Mi banda Latina (Leslye, Mariana, Sole, Willy, Fede, Pedro) con quienes ha surgido una gran amistad y espero que dure mas allá de la distancia, gracias, os quiero!.

A la Termosecta, por los grandes momentos de gloria y sufrimiento que hemos vivido durante tanto años, en especial a los Directores técnicos Willy y Aleix y al gran capitán Xavi, que nos anima a darlo todo cada partido. A los compañeros de los equipos Cataluña y Resto del Mundo, por esos grandes enfrentamientos.

A todo el conjunto de miembros del CTTC que colaboraron de forma directa o indirecta en el desarrollo de esta Tesis. Compañeros me siento muy orgulloso de trabajar con ustedes, por ser grandes investigadores y tener siempre la disposición para ayudarnos los unos a los otros.

En el terreno más personal, quiero agradecer: a mis amigos Venezolanos, a los que tengo cerca (MariaL, Jessenia, MariaT y Oli) por estar siempre, nos hemos divertido. A quienes están lejos y a pesar de no tener siempre contacto (Rebe, Cesar, Yonnathan y Diego), cuando nos reencontramos es como como si no nos hubiéramos separado nunca.

A mi familia en Cataluña los Raventós, quienes de una forma u otra nos han ayudado a sentirnos como en casa. Francesc y Marta gracias, por su apoyo y afecto inestimables durante todos estos años.

Para terminar quiero aprovechar este espacio para agradecerle a las personas que más quiero. A mi familia (los Torras, los Ortiz y los Matheus) por su apoyo incondicional y cariño, os quiero!!!. Muy especialmente a mis padres, por su amor y apoyo en todo momento en cualquier decisión que he tomado. Es algo que valoro infinitamente y que siempre tendré en cuenta. Papa por transmitirme entusiasmo y ser de gran ayuda en estos últimos meses y te lo agradezco. A ti mami, te mereces una mención especial, siempre has sido mi ejemplo y se que esta distancia que nos separa ha sido larga y dura, sirvan estas líneas como prueba de que este trabajo también está dedicado a ti.

A mi hijo Sebastían, gracias por dar tanta alegría y energía a nuestras vidas, y hacer que al llegar a casa el mundo se detenga y todo lo no tan bueno se quede afuera.

A ti Maria Andrea, por ser mi compañera en este largo viaje, sin ti no hubiera sido capaz de terminarlo, este triunfo es de ambos, lo hemos logrado!!!. Gracias por estar siempre a mi lado, creer en mí y darle significado a todo, Te Amo!.

Santiago Torras Ortiz

Contents

Acknowledgements **9**

Abstract **13**

1 Introduction **15**
1.1 Prologue . . . 15
1.1.1 Thermal storage systems in drain water heat recovery device . 16
1.1.2 Thermal storage systems in a in-space cryogenic propulsion system . . . 18
1.1.3 Thermal storage systems in concentrated solar power . . . 21
1.2 Background . . . 22
1.3 Objectives and Outline . . . 23
1.4 Applicability . . . 24
References . . . 25

2 Drain Water Heat Recovery Storage-type Unit for Residential Housing **33**
2.1 Introduction . . . 34
2.2 Numerical Model . . . 37
2.2.1 Numerical Simulation of In-Tank Free Convection . . . 38
2.2.2 Numerical Simulation of In-Tube Single-Phase Flow . . . 39
2.3 Experimental Setup . . . 43
2.3.1 Test Section . . . 45
2.3.2 Experimental Procedure . . . 46
2.4 Results . . . 47
2.4.1 Test Conditions . . . 47
2.4.2 Mesh refinement studies and Boundary Conditions used in the numerical simulations . . . 47
2.4.3 Extraction Process results . . . 50
2.4.4 Storage Process results . . . 59
2.5 Concluding Remarks . . . 63
References . . . 65

3 Numerical Modelling and Experimental Validation of a Thermal Energy Accumulator for Propulsion Systems Under Cryogenic Conditions **69**
3.1 Introduction . . . 71
3.2 Mathematical Model & Numerical Implementation . . . 75
3.2.1 Numerical simulation of the fluid inside the tube . . . 75
3.2.2 Numerical simulation of fluid inside the tank . . . 76

3.2.3 Numerical simulation of the solid tube . . . 77
3.2.4 Numerical simulation of the gas contained . . . 78
3.2.5 Coupled resolution . . . 78
3.3 Experimental validation . . . 81
3.3.1 Results of case A . . . 86
3.3.2 Results of case B . . . 87
3.3.3 Results of case C . . . 92
3.3.4 Results of case D . . . 101
3.4 Concluding Remarks . . . 107
References . . . 109

4 Parametric study of two-tank TES systems for CSP plants 113
4.1 Introduction . . . 114
4.2 Mathematical Model . . . 117
4.2.1 Molten salt global model . . . 117
4.2.2 Gas ullage model . . . 119
4.2.3 Tank walls and insulation . . . 119
4.2.4 Foundation (simplified zonal model) . . . 120
4.3 Definition of the cases and parametric studies . . . 122
4.3.1 Definition of the reference case . . . 122
4.3.2 Operating conditions . . . 123
4.3.3 Parameter candidates . . . 126
4.4 Parametric study . . . 128
4.4.1 Effect of meteorological data . . . 128
4.4.2 Effect of the insulation thickness . . . 131
4.4.3 Effect of the configuration of the foundation . . . 136
4.5 Conclusions . . . 144
References . . . 147

5 Conclusions and further work 149
5.1 Conclusions . . . 149
5.2 Further Work . . . 151
References . . . 152

A STEScode 155
A.1 STEScode . . . 155
A.1.1 A brief sample of the STEScode: . . . 158

B Main publications in the context of this thesis 171

Abstract

This thesis aims at studying different sensible and latent thermal energy storage (TES) systems. Numerical simulation is an indispensable tool for the design, evaluation and optimization of thermal equipment, in addition to the experimental techniques. Numerical tools were developed, adapted and implemented within a general purposes platform for their evaluation. Different levels of analysis have been carried out, i) within the field of Computational Fluid Dynamic and Heat Transfer (CFD&HT), the coupling between the heat conduction in solid parts and single flow/two phase flow 1D inside the tube, has allowed the accurate transient simulation of the complex heat transfer and fluid dynamics phenomena presented; ii) within thermal energy management, storage tank in CSP like a whole system has been studied; iii) it is interesting to highlight that numerical models have been experimental validated by mean of experimental results from the literature or with specific facilities carried out within the experimental infrastructure developed during this Thesis for validation purposes.

All the contents of the main chapters of this Thesis, apart from the Introduction and Conclusions, have been submitted (chapters 2 and 3) or are going to be submitted (chapter 4) to international journals, and thus, they are written in order to be self-contained. For this reason, some concepts and equations are repeated throughout different chapters.

In chapter 2, numerical and experimental tools have been used to design and study the performance of a specific drain water heat recovery storage-type. The device has been built and a experimental unit has been constructed. The experimental unit provides data to study the storage capacity and the delivering energy process of the DWHR storage device. The experiments have generated the data for the boundary conditions definition and results for validation of the numerical simulations. The numerical simulation has been performed within the NEST platform, where the different elements of the DWHR storage are linked to solve the system. Different internal flow rates and operational temperatures have been studied. From the results obtained it can be said that the device shows interesting heat recovery and storage capacities, while the numerical platform shows promising comparison results against the experiments. This numerical platform will be applicable to future versions of DWHR storage (geometric configuration and operational condition).

In chapter 3, a methodology for the resolution of Computational Fluid Dynamics and Heat Transfer (CFD&HT) problems in a Low Temperature Accumulator (LTA) prototype of a Low Thrust Cryogenic Propulsion (LTCP) system is proposed. The numerical model has been performed within the NEST platform. Two numerical models have been adapted, one to solve the thermal and fluid-dynamic behaviour of the two-phase flow inside ducts working under cryogenic conditions, and another to

solve the solid-liquid phase change phenomena using a fixed-grid enthalpy model. The thermal energy storage tank considered is formed by different elements: the two fluids (water and air) inside tank, the tube and the in-tube fluid (nitrogen), which interact with each other through their boundary conditions. Experiments from the literature have been used for the validation of the models proposed. In these experiments, different combinations of single-phase/two-phase (evaporation) flow of the fluid (LN_2/N_2) inside the tube together with different combinations of single-phase (liquid water) / two-phase (water-ice, in process of freezing or melting) of the fluid inside the tank. An acceptable agreement between experiments and numerical results was observed. The experimental validation under different working conditions of the cryogenic flow and/or the PCM material, shows the possibilities of this model for design optimization and prediction purposes of such type of devices.

In chapter 4, a numerical models for the simulation of the two-tank thermal energy storage system in concentrating solar power plants has been developed. The numerical simulation has been performed within the NEST platform, where the different elements of the two-tank storage are linked to solve the system. Some elements of the system have been specifically developed. The mathematical model considers the transient behaviour of the molten salt fluid, the gas ullage, the tank walls and insulation, different configuration of the foundation, radiation exchange between the salt and the tank walls in the ullage. A parametric study of the two-tank storage system has been done, in order to identify the most important parameters on TES system, in order to improve the design and increase the performance of the plant. A part of this work has been used to develop an in-house software called STEScode. This software is based on a modular object-oriented methodology, and allows the detailed thermal and fluid dynamic analysis of sensible TES systems for designing purposes and with a reasonable computational effort.

To accomplish these goals, some obstacles have to be overcome. Some of the challenging arising issues involve the generation of suitable and affordable meshes, the implementation and validation of different in-house code and coupling of different domains (fluid and solid) with important adjustments for the study of cases with different flow physics like time steps and thermal development.

In conclusion, the implementations and general contributions of the present Thesis together with the previous existent multi-physics computational code, has proved to be capable to perform successful numerical simulations of the behaviour of storage systems of different realistic applications.

Chapter 1

Introduction

1.1 Prologue

Developing efficient and inexpensive energy storage devices is as important as developing new energy sources. Thermal energy is necessary in many domestic, commercial and industrial applications and, therefore, must be generated, stored and used efficiently to take advantage both economically and environmentally.

Thermal energy storage (TES) systems aims to accumulate thermal energy at high or low temperatures, in order to be used later. TES can reduce time or mismatch between energy generation and energy demand, and consequently considered a key aspect in a wide range of applications for different sectors in engineering, such as chemical industry, solar energy systems, food industry, industrial processes, refrigeration, among others. They can also reduce peak demand, energy consumption and CO_2 emissions, while increasing overall efficiency of energy systems.

The performance of a TES system device is characterized by different parameters such as the storage capacity and time, the heat transfer rates during charging and discharging process and the storage efficiency.

There are three main types of TES systems: thermochemical heat storage, sensible heat storage and latent heat storage. The thermochemical energy storage is produced when a chemical reaction with high energy involved in the reaction is used to store energy. The thermochemical storage entails an endothermic reversible reaction, which can be reversed when required to release heat. The sensible heat storage is when the energy is stored increasing or decreasing the temperature of the storage medium (e.g. water, oil, molten salts, fire brick, rocks, etc.). TES systems based on sensible heat storage offer a storage capacity that is limited by the specific heat of the storage medium. These type of equipment are widely used in thermal systems because of their simplicity and low cost. The choice of the storage medium depends largely on the temperature level of the application. The most popular sensible storage medium in the low-to-medium temperature range is water, which has a number

of residential and industrial applications, such as solar domestic hot water and space heating [1–4]. Within the high temperature range, there are several materials that are extensively used as storage mediums such as oils, concrete and molten salts [5]. These substances are mainly used in solar power plants [6–8]. The third storage system mentioned above, latent heat storage, uses different materials, e.g. water/ice, paraffins [9] and salt hydrates [10]. Although liquid-vapour phase change usually results in greater latent energy changes, solid-liquid transitions are usually preferred due to their lower changes in density [11]. Materials used for latent heat storage are called phase change materials (PCM). PCM can be used for both short-term (daily) and long-term (seasonal) energy storage, using a variety of techniques and materials. The latent heat storage has the advantages of compactness and they can store and deliver energy an almost constant temperature. PCMs are being used or studied in several thermal storage applications. Some examples are the integration of PCM to building walls in order to achieve thermal comfort in buildings lowering the cooling and heating demand [12, 13], others application can be found in solar collectors [14] and in concentrating solar power plants [15].

Optimum design of TES systems needs adequate predicting methods. In this sense, considering the complexity of these thermal systems, numerical simulations play an essential role in many technological applications. Next section is dedicated to this important issue.

1.1.1 Thermal storage systems in drain water heat recovery device

The drain water heat recovery (DWHR) is designed to recover the residual energy from the hot or warm drain water, and this recover energy is used to preheat the incoming cold water. This interesting technology is an efficient and low-cost way of recovering thermal energy for its reutilization in typical building processes, as space heating and sanitary hot water generation. The residential sector accounts for 26% of the total energy consumption in the USA. Of this, 37% is electricity for lighting, cooling, and appliances. The remaining energy used is attributed to heating: 45% for space heating and 24% for water heating [16]. Therefore, residential water heating accounts for 4% of the total national energy demand. In other countries like the UK, the residential sector representing a 29% of total energy consumption in the country. Of this, 65% for space heating and 16% for water heating [17]. Thus, the energy used for heating water represents a significant part of the total energy which is consumed in a typical household. There are many works, e.g. Boait et al. [18] and Leidl et al. [19], where different technologies are analysed in order to save energy used to heat domestic water, including solar water heating (SWH), gas boilers, heat pumps, immersion heaters and drain water heat recovery.

There are different types of DWHR systems. Authors like Cooperman et al. [20] classified them into two types: on-demand and storage. For the on-demand type, the

warm drain water flows down in the inner pipe while simultaneously the incoming cold water flows up in the external coiled tube. This type of DWHR is referred to as a gravity film heat exchanger. In the storage type described by Cooperman, the warm drain water flows through the heat exchanger heating the clean water into the tank for future use.

In the literature there are some studies on the DWHR systems, most of them of the falling film heat exchanger, also known as a vertical inline drain water heat recovery heat exchanger. Zaloum et al. [21] demonstrated that the use of vertical exchanger is justified when the movement of the two media is simultaneous. They conducted their experiments on eight different film exchangers to determine the effect of flow rate, temperature and configuration in heat recovery performance. In the different film exchangers, the maximum heat recovered is reached at the lowest flow rates (using the same flow rates for the two media), while the other parameters showed no significant effect on the heat recovery efficiency. McNabola et al. [22] and Wong et al. [23] analysed the efficiency of using the DWHR in a horizontal position. Both authors used a simple single-pass counter-flow heat exchanger installed horizontally beneath the shower drain.

In works [24, 25] the DWHR are implemented in heat pump systems, and specific numerical models have been developed to their analysis. Wallin et al. [26] experimentally studied the performance of this type of device in a heat pump system. In their work, the exchanger had the capacity to recover more than 25% of the energy available in the drain water for the investigated flow rates (as an evaporator to recover waste heat from shower water).

Ni et al. [27] analysed the potential saving of incorporating a DWHR in heat pump system to reclaim heat from residential wasterwater for space heating, space cooling and domestic water heating. A numerical model was developed for the comparison of annual energy consumption and drinking water savings between the water energy-recovery system and the conventional building energy system.

Heat exchangers with coiled pipe are used in many applications such as the nuclear industry, refrigeration, food industry, etc. This is because the coiled pipe has higher heat transfer coefficients in comparison with a straight tube [28], while it also allows a more compact structure. The modification of the flow in the coiled pipe is due to the centrifugal forces, where the curvature of the tube produces a secondary flow field with a circulatory movement (Dean [29, 30]).

There is a considerable amount of work focused on the internal heat transfer in coiled pipe. Works carried out since the end of the decade of the 50s have generated interesting correlations based on experimental data. Some examples can be found in Ito [31], Seban et al. [32], Rogers et al. [33], Schmidt [34] and Gnielinski [35]. The generated correlations have been widely used for the internal heat transfer in coiled pipe. Numerical investigation were performed to understand the heat transfer in

laminar flow in coiled pipes by Dravid et al. [36].

However, there is little information in the literature about the external heat transfer in coiled pipe. Ali conducted experimental studies for coiled pipes immersed in water [37] and glycerol-water [38]. From his studies, Ali developed a correlation to evaluate the outside heat transfer. Xin and Ebadian [39] conducted experimental investigations of the outside heat transfer for natural convection from coiled pipes in air. Subsequently, they investigated the effect of the Prandtl number and geometrical parameters on the outside heat transfer from the coiled pipes immersed in air, water and ethylene-glycol [40].

A similar configuration to the one studied in this Thesis, but used in another type of applications, can be seen in the works by Prabhanjan et al. [41] and Fernández-Seara et al. [42]. They worked with coiled pipes immersed in water and the fluid inside the coiled pipe was water. In addition, these authors combine experimental and numerical studies. Prabhanjan et al. developed a model to predict the outlet temperature of a fluid flowing through a helically coiled heat exchanger. Fernández-Seara et al. developed a numerical model in order to predict the heat transfer process and pressure drop in a helically coiled heat exchanger. Both works described above the temperature of the fluid within the tank is maintained constant.

1.1.2 Thermal storage systems in a in-space cryogenic propulsion system

Since the beginning of the space travel, rockets propelled by chemical propulsion systems are the most widely used technology in spacecraft propulsion to overcome Earth's gravity. These technologies are capable of producing the magnitude of thrust necessary. In these systems the energy to generate the thrust is obtained by chemical reactions by forcing a gas from the rear of the vehicle at very high speed through a supersonic de Laval nozzle. However, once in orbit, this propulsion system has a significant limitation, due to its relatively low specific impulse (I_{SP}) if they are compared with other emerging technologies such as electric propulsion [43, 44]. The chemical propulsion has a fixed amount of energy per unit mass, which limits the achievable exhaust velocity or specific impulse. However, because the rate at which the energy can be supplied by the propellant is independent of their mass, it implies that a very high powers and thrust levels can be achieved [45].

The spacecraft usually have a second propulsion system with a higher I_{SP} and thus being able to travel in space. This system is called in-space propulsion, and it is the technology capable of generating the thrust necessary for a spacecraft to travel through space. Actually, the main objective of this technology is to allow the propulsion of the spacecraft to move from one orbit to another or make minor corrections. There are different in-space propulsion technologies, and its use is condi-

tioned by the mission, because there is no single propulsion technology that benefit all missions or mission types. Each technology has drawbacks and advantages. The requirements for in-space propulsion vary widely according to their intended application [46–48].

There are many institutions/agencies involved in the identification, development and use of new technological candidates. Some of them are: the European Space Agency (ESA), the National Aeronautics and Space Administration (NASA), and other space related organizations all over the world. These agencies define a master plan or roadmap that takes into account a wide range of technologies, which can be found in process of developing technologies for the next years, which are potential candidates for use on future space travels [47, 48].

ESA's master plan [47] and the NASA's roadmap [48] propulsion technology divide the propulsion technology in the space into different groups. The division is based on the physics of the propulsion system and how it derives thrust, as well as its technical maturity. The technologies include systems that operate through chemical reactions to heat and expand a propellant to provide thrust (liquid and solid propellants, liquid cryogenic, etc.), propellant storage and transfer, among others.

The In Space Propulsion-1 (ISP-1) project [49] was initiated with the objective of improving the knowledge and the techniques which are necessary for future space missions that are related with cryogenic propulsion. The ISP-1 project does not focus on the early launch phase, but on the technologies involved in the subsequent phases of a space mission, once the spacecraft has already been placed in orbit. The idea of using cryogenic propulsion is because toxic propellants with poor propulsion performance are frequently used. The cryogenic propulsion, on the other hand, produces non–toxic/harmless exhaust gases and the specific impulses are much higher. Cryogenic liquids are liquefied gases that are kept in their liquid state at very low temperatures. These liquids are extremely cold and have boiling points less than -150°C . All cryogenic liquids are gases at normal temperatures and pressures. The cryogenic liquids most used are: liquid hydrogen (LH_2), liquid oxygen (LO_X), liquid nitrogen (LN_2), liquid methane (LCH_4), among others. Nowadays, cryogenic propulsion based on LO_X propellant is a mature field and a core technology [50]. In-space cryogenic fluid management has been of interest to NASA since the 1960s for scavenging cryogenic propellants [51]. LO_X/LH_2 also powered the upper stages of the Saturn V and Saturn IB rockets, as well as the Centaur upper stage, the United States' first LO_X/LH_2 rocket (1962). Plans for integrated cryogenic propellant flight demonstrations have been carried out since the end of the decade of the 1980s, such as COLD-SAT [52]. The COLD-SAT studies was conducted in the early 1990s [52] and summarized by NASA in 1998 [53]. The COLD-SAT was intended to provide sufficient data on the storage and handling of cryogens (specifically liquid hydrogen) in the low gravity environment of space to enable future space systems to be

confidently and efficiently designed. For its part, ESA worked on the first Ariane launcher as early as 1974, using a cryogenic technology of combining liquid oxygen and liquid hydrogen. The Ariane rocket family has evolved over the years to meet the demands of the market. For over 30 years, Ariane rockets have been the mainstay of European space launch capabilities. The reliability and versatility of Ariane rockets has allowed them to become one of the worlds premier commercial satellite launchers. The HM7B is a European cryogenic upper stage rocket engine used in Ariane rocket family. The development of HM7 engine begun in 1973 on a base of HM4 rocket engine [54]. It was designed to power a third stage of newly constructed Ariane 1, the first launch system for ESA. The HM7 will be replaced by Vinci as an upper-stage engine for Ariane 5 [55]. Vinci is currently under development. The Soviet Union did not even test a (LH_2) upper stage until the mid-1980s [56]. The Russians are now designing their Angara rocket family with liquid-hydrogen upper stages [57].

The basic system studied in the ISP-1 project is the low thrust cryogenic space propulsion (LTCP) system, that is mainly composed of hydrogen and oxygen propellant tanks, propellant pumps, a fuel cell, heat accumulators, a main combustion chamber, attitude control thrusters and, a fuel cell cooling circuit. One of the components, the heat accumulator, stores the thermal energy from the fuel cell that provides electrical energy to the whole system. This thermal energy is employed for the pressurization of the propellant tanks and gasification of the propellant to the combustion chamber. Two different types of heat accumulators are present in the LTCP system: the High Temperature Accumulator (HTA) and the Low Temperature Accumulator (LTA). The HTA provides the thermal energy for the self-pressurisation of the hydrogen tank and the LTA provides thermal energy for the self-pressurisation of the oxygen tank [58]. The fuel cells have an operating optimum temperature at about +80°C.

The base idea of this kind of in-space propulsion system is the Low Cost Cryogenic Propulsion (LCCP) concept [59], which was previously patented by Société Nationale d'Études et de construction de moteurs d'Aviation (SNECMA) [60]. The aim of saving energy by heat accumulators starts from the fact that on the one hand, a cooling of the fuel cells is necessary, which provide electrical energy for the spacecraft, and therefore also some sort of cooling device is needed. On the other hand, thermal energy is necessary during the engine operation, especially at the starting of the engines, in order to: i) pressurise the tanks themselves by the help of vaporization of their corresponding propellant and; ii) a better combustion in the combustion chamber. However, the refrigeration needs of the fuel cell are not coincident in general with the needs of propellant gasification. For this reason, energy storage is of special interest.

1.1.3 Thermal storage systems in concentrated solar power

Concentrated solar power (CSP) plants are experiencing considerable growth in recent years. They are based on well-proven technology for providing a considerable part of renewable electricity [61]. CSP uses renewable solar resource to generate electricity while producing very low levels of greenhouse-gas emissions. Thus, it has strong potential to be a key technology for mitigating climate change. There are four main CSP systems that perform the conversion of solar energy into electricity: parabolic troughs, power towers, linear Fresnel reflectors and parabolic dishes, which can be categorised by the way they focus the solar rays and the technology used to receive the solar energy (see for instance [62, 63]). Although they have different characteristics, the operating principle is the same. Reflector elements concentrate the solar rays into a receiver, where a heat transfer medium is heated, and use to drive a steam turbine.

Thermal energy storage (TES) systems can be considered a key aspect for concentrated solar power plants, as they provide not only dispatchable electricity but also stability to the electricity network in case of high fraction of renewable production or intermittences due to weather conditions. Today, the two-tank system employing molten salt are the most used configuration [6, 64], which make profit of the sensible energy changes of a heat transfer fluid (molten salt) under a temperature difference. The two-tank storage systems are subdivided into direct and indirect systems. In a direct system, the heat transfer fluid also serves as the storage medium, while in an indirect system, a second medium is used for storing the heat [8]. For instance, Gemasolar plant (located in Fuentes de Andalucia, near to Seville, Spain) has a power tower technology [65]. Its storage system is based on two-tank direct system. As an example of the two-tank indirect system is Andasol I [64]. This solar thermal power plant is located in Guadix, Granada (Spain), and the solar field is based on parabolic trough technology.

In the two-tank storage systems there are significant design considerations that must be taken into account, namely, avoiding the salt freezing by controlling the heat losses, and storage optimization (aspect ratio, design of the inlet ports, etc.). A profound knowledge of the thermal and fluid-dynamic phenomena present inside storage tanks is required to reduce/control heat losses and design optimization. Efforts made for integrating this technology within demonstration and commercial plants can be found in Refs. [64, 65]. In addition to the accumulative experience acquired in the sector, optimization techniques based on computational fluid dynamic and heat transfer (CDF&HT) are becoming an important tool. One of the few CFD&HT simulations carried out for these tanks was conducted by Schulte-Fischedick et al. [66]. In their work, they coupled a CFD simulation using a RANS model for evaluating the molten salt behaviour with a finite element method for the tank walls. More recently, Rodríguez et al. [67] presented a methodology for studying the molten salt TES by

coupling different levels of modelisation in which the molten salt was evaluated using large eddy simulation (LES).

1.2 Background

The present Thesis has been developed within the framework of the collaborations between Termo Fluids S.L. and the Heat and Mass Transfer Technological Center (CTTC) of the Technical University of Catalonia (UPC). CTTC is centred on two principal research lines, one dedicated to the mathematical formulation, numerical resolution and experimental validation of fluid dynamics and heat and mass transfer phenomena and, at the same time, the application of the acquired know-how from the basic studies into the thermal and fluid dynamic optimisation of thermal systems and equipment. Termo Fluids S.L. is a spin-off which was born 9 years ago from members of the CTTC that is owner of NEST and TermoFluids source code. This company is devoted to the development of new numerical methods and software tools for High Performance Computing (HPC) in Computational Fluid Dynamics and Heat Transfer (CFD&HT) and to the optimization of thermal systems and their equipment.

Thanks to this collaborative work, a new software platform, called NEST was developed. This platform has been used to implement different models for studying thermal energy storage systems. The platform allows the linking between different elements to perform a specific thermal system. Multiple levels of modelling can be implemented to obtain different levels of analysis. NEST has been involved in many industrial projects, such as to improve the energy efficiency in domestic refrigerator [68] and building [69]. More research projects that used the NEST platform can be found in [70].

Several Thesis and scientific papers on the subject of solar energy, thermal storage systems of heat exchangers and refrigerant systems have been published by researchers of the CTTC in the past, e.g. [71–77]. Alex Ivancic [71] worked in the resolution of natural and forced convection problems applied to cylindrical storage devices. Ivette Rodríguez [72] worked in the numerical resolution of storage devices for solar thermal systems in the low-to-medium temperature range. Theses of Miquel Costa [73] and Barbara Vidal [74], dealing with the fixed-grid modelling of solid-liquid phase change in structured meshes. Later, Pedro Galione [75] developed and implemented a numerical model for the simulation of solid-liquid phase change phenomena in a highly parallel, CFD platform using unstructured meshes. In addition, a study of a tank filled with solid and/or PCM materials forming a packed bed through which a heat transfer fluid flows have been done. In this Thesis, numerical simulations of thermal storage systems emphasis on latent energy storage has been studied. Furthermore, Sergio Morales [76] and Nicolas Ablanque [77] have worked

in the development of two-phase flows models using the quasi-homogeneous formulation and the two-fluid model. All these theses have served as a very good starting point for the work carried out in this Thesis.

1.3 Objectives and Outline

The main objective of this Thesis is the numerical resolution of heat transfer and fluid flow problems and its application to study the unsteady behaviour of thermal energy storage (TES) systems. Three different systems have been considered, covering a wide range of working conditions (from very low cryogenic temperature to very high temperature CSP plant) and applications (from domestic/residential to renewable or aerospace industry). In that sense, i) for residential heat recovery systems in the low-to-medium temperature range; ii) a thermal accumulator used in a in-space cryogenic propulsion system in the low temperature range and; iii) the two-tank thermal energy storage system in concentrating solar power (CSP) plants in the high temperature range. The Thesis is divided into five chapters.

Chapter 2 is devoted to present the methodology employed for the resolution of Computational Fluid Dynamics (CFD) and Heat Transfer problems in a drain water heat recovery (DWHR) storage-type unit for residential housing. The study of the performance of this device has been carried out using both numerical and experimental tools. The numerical simulation has been performed using the NEST platform [78], where the different elements of the DWHR storage are linked to solve the system. The discretisation of the governing equations based on finite volume techniques (FVM) is presented. Numerical techniques such as the discretisation schemes, boundary conditions implementation and solution procedure for incompressible and transient flow problems are shown. Special empirical correlations have been implemented to be used in the numerical resolution of the single-phase flow inside the coiled pipe. An experimental infrastructure has been developed to analyse the whole system. Different internal flow rates and operational temperatures have been studied. The numerical results are compared against experimental results. The numerical simulations performed predict reasonably the transient behaviour of the DWHR storage device. The contents of this chapter have been submitted to an international journal.

Chapter 3 focuses the attention on a Low Temperature Accumulator prototype used in an in-space cryogenic propulsion system. The numerical simulation has been carried out using the NEST platform [78], where the different elements of the thermal accumulator are linked to solve the whole system. In this chapter, two numerical models have been adapted, one used to solve the two-phase flow inside ducts working under cryogenic conditions, and another to solve the PCM using a fixed-grid enthalpy model developed by Galione et al. [11]. The numerical analysis is based

on: i) a one-dimensional and transient resolution of the governing equations for the fluid flow of propellant; ii) a multi-dimensional and transient resolution of the governing equations in the region occupied by the PCM, incorporating a model for the turbulence to solve the convection phenomena involved; iii) the solid elements are modelled considering a multidimensional and transient treatment of the thermal conduction equation. The numerical results are compared against experimental results from the literature. The experimental validation under different working conditions of the cryogenic flow and/or the PCM material shows the possibilities of this model for design optimization and prediction purposes. The contents of this chapter have been also submitted to an international journal.

Chapter 4 is focused on the development of a numerical model for the simulation of the two-tank thermal energy storage system in concentrating solar power (CSP) plants. The numerical simulation has been performed using the NEST platform [78], where the different elements of the two-tank storage are linked to solve the system. Some elements of the system have been specifically developed. The mathematical model considers the transient behaviour of the molten salt fluid, the gas ullage, the tank walls and insulation, different configuration of the foundation, radiation exchange between the salt and the tank walls in the ullage. A parametric study of the two-tank storage system has been done, in order to identify the most important parameters on TES system. From the work by Rodríguez et al. [67] and the work presented in this chapter, an in-house software called STEScode has been developed. The STEScode is based on a modular object-oriented methodology, and allows the detailed thermal and fluid dynamic analysis of sensible TES systems for designing purposes and with a reasonable computational effort. The contents of this chapter are going to be submitted to an international journals.

A final chapter with the conclusions of the studies carried out in this Thesis is presented. The guidelines for future research work in these applied areas are also suggested.

1.4 Applicability

A significant part of the present work has been developed within the framework of different research projects between the CTTC and the industry. Specifically:

- SEILA - New technologies for an efficient, ecologic and intelligent washing system for textiles of the future. Research Project C07973, ref. CEN-20091005. The company involved in the project was Fagor Electrodomésticos, during the period 2010-2012.
- In Space Propulsion 1. Research Project, ref. 218849, ISP-1; European Comission, Directorate-General XII. The companies involved in the project were:

Snecma, Astrium, AVIO, Mikroma, Alcimed, Bonatre, during the period 2009-2012.

- TESCONSOL - Thermal storage for concentrating solar power plants. Research Project Q-00023, ref. CEN-20091005. The company involved was EIT-KIC InnoEnergy, during the period 2011-2014.

References

[1] M.K. Sharp, R.I. Loehrke. Stratified thermal storage in residential solar energy applications. *Energy*, 3:106–113, 1979.

[2] R. Cònsul, I. Rodríguez, K. Claramunt, A. Oliva. Thermal stratification improvements in thermal storage tanks: Numerical analysis of directed inlet mass flow rates strategies. In *Proceedings of the 5th ISES Europe Solar Conference (EUROSUN 2004)*, 2004.

[3] I. Rodríguez, A. Oliva, C.D. Pérez-Segarra. Numerical study of the transient convection inside solar domestic hot water storage tanks. In *Proceedings of the 6th ISES Europe Solar Congress (EUROSUN 2006)*, 2006.

[4] S. Alizadeh. An experimental and numerical study of thermal stratification in a horizontal cylindrical solar storage tank. *Solar Energy*, 66:409–421, 1999.

[5] A. Gil, M. Medrano, I. Martorell, A. Lázaro, P. Dolado, B. Zalba, L.F. Cabeza. State of the art on high temperature thermal energy storage for power generation. Part 1—Concepts, materials and modellization. *Renewable and Sustainable Energy Reviews*, 14:31–55, 2010.

[6] U. Herrmann, B. Kelly, H. Price. Two-tank molten salt storage for parabolic trough solar power plants. *Energy*, 29:883–893, 2004.

[7] D. Kearney, B. Kelly, H. Price. Thermal storage commercial plant design study for a two-tank indirect molten salt system. Technical Report NREL/SR-550-40166. National Renewable Energy Laboratory, Colorado, USA, 2016, www.nrel.gov.

[8] M. Medrano, A. Gil, I. Martorell, X. Potau, L.F. Cabeza. State of the art on high-temperature thermal energy storage for power generation. Part 2—Case studies. *Renewable and Sustainable Energy Reviews*, 14:56–72, 2010.

[9] Rubitherm Technologies. http://www.rubitherm.eu/.

[10] B. Zalba, J.M. Marín, L.F. Cabeza, H. Mehling. Review on thermal energy storage with phase change: materials, heat transfer analysis and applications. *Applied Thermal Engineering*, 23:251–283, 2003.

[11] P.A. Galione, O. Lehmkuhl, J. Rigola, A. Oliva. Fixed-grid modeling of solid-liquid phase change in unstructured meshes using explicit time schemes. *Numerical Heat Transfer*, 65:27–52, 2014.

[12] Y. Zhang, G. Zhou, K. Lin, Q. Zhang, H. Di. Application of latent heat thermal energy storage in buildings: State-of-the-art and outlook *Building and Environment*, 42:2197–2209, 2007.

[13] A. de Gracia, L.F. Cabeza. Phase change materials and thermal energy storage for buildings. *Energy and Buildings*, 103:414–419, 2015.

[14] H. Mehling, L.F. Cabeza, S. Hippeli, S. Hiebler. PCM-module to improve hot water heat stores with stratification *Renewable Energy*, 28:699–711, 2003.

[15] H. Michels, R. Pitz-Paal. Cascaded latent heat storage for parabolic trough solar power plants. *Solar Energy*, 81:829–837, 2007.

[16] DOE, 2011 buildings energy data book. U.S. Department of Energy, 2011.

[17] Energy Consumption in the UK (2014). Department of Energy & Climate Change, London SW1A 2AW. Webpage: http://www.gov.uk/decc, 2014.

[18] P.J. Boait, D. Dixon, D. Fan, A. Stafford. Production efficiency of hot water for domestic use. *Energy and Buildings*, 54, 2012.

[19] C.M. Leidl, W.D. Lubitz. Comparing domestic water heating technologies. *Technology in Society*, 31, 2009.

[20] A. Cooperman, J. Dieckmann, J. Brodrick. Drain Water Heat Recovery. *ASHRAE Journal 2011*, 2011.

[21] C. Zaloum, M. Lafrance, J. Gusdorf. Drain water heat recovery characterization and modeling, Final draft. Sustainable Building and Communities, Natural resurces, Canada, 2007.

[22] A. McNabola, K. Shields. Efficient drain water heat recovery in horizontal domestic shower drains. *Energy and Buildings*, 59, 2013.

[23] L.T. Wong, K.W. Mui, Y. Guan. Shower water heat recovery in high-rise residential buildings of Hong Kong. *Applied Energy*, 87, 2010.

[24] X. Liu, L. Ni, S.K Lau, H. Li. Performance analysis of a multi-functional Heat pump system in heating mode. *Applied Thermal Engineering*, 51, 2013.

[25] W. Chen, S. Liang, Y. Gou, K. Cheng. Investigation on the thermal performance and optimization of a heat pump water heater assisted by shower waste water. *Energy and Buildings*, 64, 2013.

[26] J. Wallin, J. Claesson. Investigating the efficiency of a vertical inline drain water heat recovery heat exchanger in a system boosted with a heat pump. *Energy and Buildings*, 80, 2014.

[27] L. Ni, S.K. Lau, H. Li, T. Zhang, J.S. Stansbury, J. Shi, J. Neal. Feasibility study of a localized residential grey water energy-recovery system. *Applied Thermal Engeneering*, 39, 2012.

[28] D.G. Prabhanjan, G.S.V. Raghavan, T.J. Rennie. Comparison of the heat transfer rates between a straight tube heat exchanger and helically coiled heat exchanger. *Int. Comm. Heat Mass Transfer*, 29:185–191, 2002.

[29] W.R. Dean. Note on the motion of fluid in a curved pipe. *Philosophical Magazine*, 4:208–223, 1927.

[30] W.R. Dean. The stream-line motion of fluid in a curved pipe. *Philosophical Magazine*, 5:673–695, 1928.

[31] H. Ito. Friction factors for turbulent flow in curved pipes. *Trans. Amer. Soc. Mech. Eng. J.*, 81:123–132, 1959.

[32] R. Seban, E.F. McLaughlin. Heat transfer in tube coils with laminar and turbulent flow. *Int. J. Heat Mass Transfer*, 6:387–395, 1963.

[33] G.F. Rogers, Y.R. Mayhew. Heat transfer and pressure loss in helically coiled tubes with turbulent flow. *Int. J. Heat Mass Transfer*, 7:1207–1216, 1964.

[34] E.F. Schmidt. Wärmeübergang und Druckverlust in Rohrschlangen. *Chem. Ing. Tech.*, 39:781–789, 1967.

[35] V. Gnielinski. Heat transfer and pressure drop in helically coiled tubes. In *Proceeding 8th Int. Heat Transfer Conference*, 6:2847–2854, 1986.

[36] A.N. Dravid, K.A. Smith, E.W. Merrill, P.L.T. Brian. Effect of secondary fluid motion on laminar flow heat transfer in helically coiled tubes. *AIChE J.*, 17:1114–1122, 1971.

[37] M.E. Ali. Experimental investigation of natural convection from vertical coiled tubes. *Int. J. Heat Mass Transfer*, 37:665–671, 1994.

[38] M.E. Ali. Free convection heat transfer from the outer surface of vertically oriented helical coils in glycerol-water solution. *Heat and Mass Transfer*, 40:615–620, 2004.

[39] R.C. Xin, M.A. Ebadian. Natural convection heat transfer from helicoidal pipes. *Journal of Thermophysics and Heat Transfer*, 10:297–302, 1996.

[40] R.C. Xin, M.A. Ebadian. The effects of prandtl numbers on local and average convective heat transfer characteristics in helical pipes. *Journal of Heat Transfer*, 119:467–473, 1997.

[41] D.G. Prabhanjan, T.J. Rennie, G.S.V. Raghavan. Natural convection heat transfer from helical coil tubes. *International Journal Therm. Sci.*, 43:615–620, 2004.

[42] J. Fernández-Seara, C. Piñeiro-Pontevedra, J.A. Dopazo. On the performance of a vertical helical coil heat exchanger. Numerical model and experimental validation. *Applied Thermal Engineering*, 62:680–689, 2014.

[43] R.G. Jahn. Physics of electric propulsion, New York: McGraw Hill (1968).

[44] R.J. Cassady, R. Frisbee, J. Gilland, M. Houts, M. LaPinte, C. Maresse-Reading, S. Oleson, J. Polk, D. Russell, A. Sengupta. Recent advances in nuclear powered electric propulsion for space exploration. *Energy Conversion & Management*, 49:412–435, 2008.

[45] T.O. Dobbins. Thermodynamics of rocket propulsion and theoretical evaluation of some prototype propellant combinations. Wright Air Development Center, TR-59-757, 1959.

[46] R. Frisbee, H. Robert. Advanced space propulsion for the 21st Century. *Journal of Propulsion and Power*, 19:1129–1154, 2003.

[47] ESA 12th edition of the European Space Technology Master Plan, 2015. European Space Agency, 2015.

[48] NASA Technology roadmaps, TA 2: In-space propulsion technologies, 2015. National Aeronautics and Space Administration (NASA), 2015.

[49] M. Muszynski, P. Alliot. The in-space propulsion (ISP-1) project. In *Proceedings of the 61st International Aeronautical Congress*, 2010.

[50] P. Caisso, A. Souchier, C. Rothmund, P. Alliot, C. Bonhomme, W. Zinner, R. Parsley, T. Neill, S. Forde, R. Starke, W. Wang, M. Takahashi, M. Atsumi, D. Valentian. A liquid propulsion panorama. *Acta Astronautica*, 65:1723-–1737, 2009.

[51] C.H. DeLee, P. Barfknecht, S. Breon, R. Boyle, M. DiPirro, J. Francis, J. Huynh, X. Li, J. McGuire, S. Mustafi, J. Tuttle, D. Wegel. Techniques for on-orbit cryogenic serving. *Cryogenics*, 64:289–294, 2014.

[52] J.R. Schuster, J.P. Wachter, A.G. Powers. COLD-SAT, an orbital cryogenic hydrogen technology experiment. *40th Congress of the International Astronautical Federation*, 1989.

[53] E. Kramer. Cryogenic on-orbit liquid depot-storage, acquisition and transfer (COLD-SAT) experiment conceptual design and feasibility study. NASA Technical paper 3523, 1998.

[54] J. Krige, A. Russo. A history of the European Space Agency 1958 – 1987, Volume II. European Space Agency, 2000.

[55] P. Alliot, P. James, C. Fiorentino, J. Follet, D. Valentian, J.M. Conrardy, D. Vuillamy, H. Goislot, P. Garceau, R. Bec. Progress of the VINCI engine system engineering. In *45nd AIAA/ASME/SAE/ASEE Joint Propulsion Conference & Exhibit*, 2009.

[56] V.P. Dawson, M.D. Bowles. Taming liquid hydrogen: the Centaur upper stage rocket 1958 - 2002, the NASA history series. National Aeronautics and Space Administration (NASA), NASA SP-2004-4230.

[57] D. Cecere, E. Giacomazzi, A. Ingenito. A review on hydrogen industrial aerospace applications. *International Journal of Hydrogen Energy*, 39:10731–10747, 2014.

[58] J. Leiner, J. Riccius, O. Haidn, D. Vuillamy. Heat accumulators for cryogenic in-space propulsion. In *Proceedings of the 4th European Conference For Aerospace Sciences (EUCASS)*, 2011.

[59] D. Valentian, J.M. Conrardy, D. Vuillamy, H. Goislot, P. Garceau, R. Bec. Low cost cryogenic propulsion module with fuel cell power supply. In *42nd AIAA/ASME/SAE/ASEE Joint Propulsion Conference & Exhibit*, 2006.

[60] SNECMA. Cryotechnic propulsion medule. European Patent EP 1241341B1, May 31, 2006.

[61] R. Sioshansi, P. Denholm. The value of concentrating solar power and thermal energy storage. Technical Report NREL/TP-6A2-45833 National Renewable Energy Laboratory, Colorado, USA, 2010, www.nrel.gov.

[62] H.L. Zhang, J. Baeyens, J. Degrève, G. Cacères. Concentrated solar power plants: review and design methodology. *Renewable and Sustainable Energy Reviews*, 22:466–481, 2013.

[63] OECD/IEA. Technology roadmap, concentrating solar power, 2010.

[64] J. Ortega, J. Burgaleta, F. Tellez. Central receiver system solar power plant using molten salt as heat transfer fluid. *Journal of Solar Energy Engineering*, 130:1–6, 2008.

[65] S. Relloso, J. Lata. Molten salt thermal storage: a proven solution to increase plant dispatchability. Experience in Gemasolar Tower plant. In *Proceeding of SolarPaces Congress*, 2011.

[66] J. Schulte-Fischedick, R. Tamme, U. Herrmann. CFD analysis of the cool down behaviour of molten salt thermal storage systems. In *Proceeding of Energy Sustainability*, 2008.

[67] I. Rodríguez, C.D. Pérez-Segarra, O. Lehmkuhl, A. Oliva. Modular object-oriented methodology for the resolution of molten salt storage tanks for CSP plants. *Applied Energy*, 109:402–414, 2013.

[68] Modular domestic refrigeration systems with high energy efficiency (KERS). Research Project, ref IPT-020000-2010-30; INNPACTO (Spanish Government). Company: Fagor Electrodomésticos, 2010-2013.

[69] Retrofitting Solutions and Services for the enhancement of Energy Efficiency in Public Edification (RESSEEPE). Research Project, ref. FPT- EeB.NMP.2013-3, E01199. 2013-2015.

[70] Heat and Mass Transfer Technological Center. Technical University of Catalonia. http://www.cttc.upc.edu.

[71] A. Ivancic. Simulación numérica de la convección natural y forzada en recintos cilíndricos. Aplicación a la acumulación de calor y frío. PhD thesis, Universitat Politècnica de Catalunya, 1998.

[72] I. Rodríguez. Unsteady laminar convection in cylindrical domains: numerical studies and application to solar water storage tanks. PhD thesis, Universitat Politècnica de Catalunya, 2006.

[73] M. Costa. Desenvolupament de criteris numèrics per a la resolució de la transferencia de calor en medis amb conducció, convecció i canvi de fase sólid-líquid. PhD thesis, Universitat Politècnica de Catalunya, 1993.

[74] B. Vidal. Modelización del cambio de fase sólido líquido. Aplicación a sistemas de acumulación de energia térmica. PhD thesis, Universitat Politècnica de Catalunya, 2007.

[75] P.A. Galione. Numerical simulations of thermal storage systems. Emphasis on latent energy storage using phase change materials (PCM). PhD thesis, Universitat Politècnica de Catalunya, 2014.

[76] S. Morales. Numerical simulation of the thermal and fluid dynamics behaviour of liquid-vapour two-Phase flow in evaporators and condensers. PhD thesis, Universitat Politècnica de Catalunya, 2009.

[77] N. Ablanque. Numerical simulation and experimental validation of vapor compression refrigerating systems. Special emphasis on natural refrigerants PhD thesis, Universitat Politècnica de Catalunya, 2010.

[78] R. Damle, O. Lehmkuhl, G. Colomer, I. Rodríguez. Energy simulation of buildings with a modular object-oriented tool. In *Proceedings of the ISES World Conference*, 2011.

References

Chapter 2

Drain Water Heat Recovery Storage-type Unit for Residential Housing

Abstract.

The drain water heat recovery (DWHR) system is an interesting household technology to reduce energy costs and environmental impact. The objective of the utilization of these devices is the recovery of the waste heat from domestic warm drain water, and transferring it to cold water entering the house. A drain water heat recovery unit has been built in this work. The authors are using both numerical and experimental tools to design and study the performance of this device, focusing on the analysis of a specific drain water heat recovery storage-type based on a cylindrical tank with an internal coiled pipe. The numerical simulation has been performed using an in-house platform, where the different elements of the DWHR storage are linked to solve the system. On the other hand, an experimental infrastructure has been developed to analyse of the system, which has been instrumented to provide detailed information of its heat recovery and storage capacities and temperature map. Different internal flow rates and operational temperatures have been studied. From the results obtained it can be said that the device shows interesting heat recovery and storage capacities, while the numerical platform shows promising comparison results against the experiments.

2.1 Introduction

Developing efficient and inexpensive energy recovery devices is as important as developing new energy sources. Heat is necessary for many building applications and, therefore, must be generated, stored and used efficiently to take advantage both economically and environmentally. The drain water heat recovery (DWHR) is designed to recover the residual energy from the hot or warm drain water, and this recover energy is used to preheat the incoming cold water. This interesting technology is an efficient and low-cost way of recovering thermal energy for its reutilization in typical building processes, as space heating and sanitary hot water generation. The residential sector accounts for 26% of the total energy consumption in the USA. Of this, 37% is electricity for lighting, cooling, and appliances. The remaining energy used is attributed to heating: 45% for space heating and 24% for water heating [1]. Therefore, residential water heating accounts for 4% of the total national energy demand. In other countries like the UK, the residential sector representing a 29% of total energy consumption in the country. Of this, 65% for space heating and 16% for water heating [2]. Thus, the energy used for heating water represents a significant part of the total energy which is consumed in a typical household. There are many works, e.g. Boait et al. [3] and Leidl et al. [4], where different technologies are analysed in order to save energy used to heat domestic water, including solar water heating (SWH), gas boilers, heat pumps, immersion heaters and drain water heat recovery.

There are different types of DWHR systems. Authors like Cooperman et al. [5] classified them into two types: on-demand and storage. For the on-demand type, the warm drain water flows down in the inner pipe while simultaneously the incoming cold water flows up in the external coiled tube. This type of DWHR is referred to as a gravity film heat exchanger, see Fig. 2.1 (a). In the storage type described by Cooperman, the warm drain water flows through the heat exchanger heating the clean water into the tank for future use. Fig. 2.1 (b) shows the storage type used in the current work, this configuration is inverted with respect to the configuration described above, the warm drain water is into the tank and the clean water flows through the heat exchanger.

In the literature there are some studies on the DWHR systems, most of them of the falling film heat exchanger, also known as a vertical inline drain water heat recovery heat exchanger. Zaloum et al. [6] demonstrated that the use of vertical exchanger is justified when the movement of the two media is simultaneous. They conducted their experiments on eight different film exchangers to determine the effect of flow rate, temperature and configuration in heat recovery performance. In the different film exchangers, the maximum heat recovered is reached at the lowest flow rates (using the same flow rates for the two media), while the other parameters showed no significant effect on the heat recovery efficiency. McNabola et al. [7] and Wong et al. [8] analysed the efficiency of using the DWHR in a horizontal position. Both

authors used a simple single-pass counter-flow heat exchanger installed horizontally beneath the shower drain.

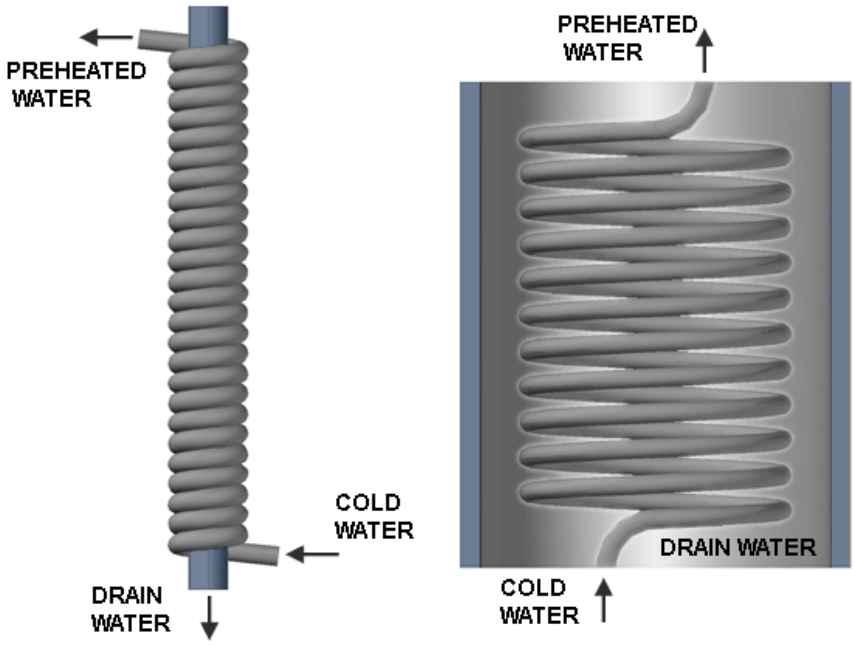

Figure 2.1: (a) On-demand DWHR; (b) storage DWHR.

In works [9, 10] the DWHR are implemented in heat pump systems, and specific numerical models have been developed to their analysis. Wallin et al. [11] experimentally studied the performance of this type of device in a heat pump system. In their work, the exchanger had the capacity to recover more than 25% of the energy available in the drain water for the investigated flow rates (as an evaporator to recover waste heat from shower water).

Ni et al. [12] analysed the potential saving of incorporating a DWHR in heat pump system to reclaim heat from residential wasterwater for space heating, space cooling and domestic water heating. A numerical model was developed for the comparison of annual energy consumption and drinking water savings between the water energy-recovery system and the conventional building energy system. In that study, the drain water heat recovery has a similar configuration to the current work.

Heat exchangers with coiled pipe are used in many applications such as the nuclear industry, refrigeration, food industry, etc. This is because the coiled pipe has higher heat transfer coefficients in comparison with a straight tube [13], while it also allows a more compact structure. The modification of the flow in the coiled pipe is due to the centrifugal forces, where the curvature of the tube produces a secondary flow field with a circulatory movement (Dean [14, 15]).

There is a considerable amount of work focused on the internal heat transfer in coiled pipe. Works carried out since the end of the decade of the 50s have generated interesting correlations based on experimental data. Some examples can be found in Ito [16], Seban et al. [17], Rogers et al. [18], Schmidt [19] and Gnielinski [20]. The generated correlations have been widely used for the internal heat transfer in coiled pipe. Numerical investigation were performed to understand the heat transfer in laminar flow in coiled pipes by Dravid et al. [21].

However, little is known about the external heat transfer in coiled pipe. Ali conducted experimental studies for coiled pipes immersed in water [22] and glycerol-water [23]. From his studies, Ali developed a correlation to evaluate the outside heat transfer. Xin and Ebadian [24] conducted experimental investigations of the outside heat transfer for natural convection from coiled pipes in air. Subsequently, they investigated the effect of the Prandtl number and geometrical parameters on the outside heat transfer from the coiled pipes immersed in air, water and ethylene-glycol [25].

A similar configuration to the studied in this chapter, but used in another type of applications, can be seen in the works by Prabhanjan et al. [26] and Fernández-Seara et al. [27]. They worked with coiled pipes immersed in water and the fluid inside the coiled pipe was water. In addition, these authors combine experimental and numerical studies. Prabhanjan et al. developed a model to predict the outlet temperature of a fluid flowing through a helically coiled heat exchanger. Fernández-Seara et al. developed a numerical model in order to predict the heat transfer process and pressure drop in a helically coiled heat exchanger. Both works described above the temperature of the fluid within the tank is maintained constant.

In this chapter, the transient evolution of the DWHR storage system is studied in order to determine its performance. For this reason in this research, the authors are developing both numerical and experimental tools to design and study the performance of this kind of systems.The numerical simulation has been performed using the in-house multi-level platform that links two codes to solve the system (in-tank + in-tube). On the other hand, an experimental infrastructure has been developed for the analysis of the system, which has been instrumented to provide detailed information of heat recovery from the waste water, heat storage capacity and temperature map. Both numerical and experimental results presented in this chapter show the potential of the proposed methodology as a very useful tool to obtain the per-

formance of drain water heat recovery device through the parametrization of the geometric variables and operating conditions when designing a DWHR storage device. The principal contribution of the current work is that, the temperature of the fluid within the tank in which the coiled pipes are immersed, is not maintained constant, and calculated in full 3D and transient detail. The drain water used in the DWHR storage device arises from domestic washing operations (especially washing machines, but also other sources, such as baths, showers, hand basins and kitchen sinks), but specifically exclude foul or black water sources.

2.2 Numerical Model

In this work the proposed numerical resolution is based on solving at different scales (Lopez et al. [28]) using the in-house NEST thermal systems simulation platform (Damle et al. [29]), which allows the linking between the three different elements (fluid inside tank, tube and in-tube fluid), constituting the DWHR storage system under study. Each of these elements can be solved independently and using different levels of modelling (from global to fully three-dimensional models), while at the same time they are linked to each other through their boundary conditions. An in-house CFD&HT (Computational Fluid Dynamics & Heat Transfer) software, called TermoFluids (Lehmkuhl et al. [30]), is used for solving the fluid movement inside the tank (section 2.2.1), while the in-tube flow is solved considering a single-phase fully-implicit one-dimensional model (section 2.2.2), where the governing equations (momentum, continuity, and energy) are discretised along the whole coil domain (Morales-Ruiz et al. [31]).

All elements of the system are solved subjected to boundary conditions that come from neighbouring elements. In each time step iteration the resolution is carried out in two steps. The first one consists of solving the in-tube flow together with the solid part of the tube. The boundary condition for each control volume is the heat flux calculated in the previous iteration from the fluid inside the tank. From this process a new temperature map for the tube is obtained. The second step consists on solving the fluid inside the tank using the CFD model with the tube temperature map obtained in the previous step. In these simulations, the global resolution algorithm used for the resolution of the whole system of elements (comprising for the fluid inside tank, tube and in-tube fluid) is a Gauss-Seidel method passing through all elements and updating the values. This algorithm has some particularities to facilitate the coupling between the different parts of the system with different schemes (implicit and explicit), and also the coupling of different time steps. A specific effort has been devoted to assure good coupling of heat transfer between in-tank and in-tube fluids (Torras et al. [32]).

2.2.1 Numerical Simulation of In-Tank Free Convection

TermoFluids software uses efficient algorithms, which compute in parallel adapting the solving strategy to the hardware architecture (communication, memory distribution,...) [30]. The Navier-Stokes equations (2.1)-(2.3) are applied to the control volumes of the domain and converted into algebraic ones using three-dimensional unstructured collocated meshes, symmetry-preserving formulation.

$$\mathbf{M}\mathbf{u} = 0 \tag{2.1}$$

$$\Omega\rho(T)\frac{\partial \mathbf{u}}{\partial t} + \mathbf{C}(\rho(T)\mathbf{u})\mathbf{u} + \mathbf{D}(v(T)\mathbf{u}) + \Omega\mathbf{G}p + f = 0 \tag{2.2}$$

$$\Omega\rho(T)c_p(T)\frac{\partial \mathbf{T}}{\partial t} + \mathbf{C}(c_p(T)\rho(T)\mathbf{u})\mathbf{T} + \mathbf{D}\left(\lambda(T)\mathbf{T}\right) = 0 \tag{2.3}$$

where $\mathbf{u} \in \mathrm{R}^{3\mathrm{N}}$, $p \in \mathrm{R}^{\mathrm{N}}$ and $\mathbf{T} \in \mathrm{R}^{\mathrm{N}}$ are the velocity vector, pressure and temperature, respectively, v is the kinematic viscosity, λ is the conductivity, ρ is the density, and c_p is the specific heat. f is the body force $f = \rho(T)\vec{\mathbf{g}}$. Convective and diffusive operators in the momentum equation for the velocity field are given by $\mathbf{C}(\mathbf{u})=(\mathbf{u}\cdot\nabla) \in \mathrm{R}^{3\mathrm{Nx}3\mathrm{N}}$, and $\mathbf{D} = \nabla^2 \in \mathrm{R}^{3\mathrm{Nx}3\mathrm{N}}$, respectively. Gradient and divergence operators are given by $\mathbf{G}=\nabla \in \mathrm{R}^{3\mathrm{Nx}\mathrm{N}}$ and $\mathbf{M}=\nabla \in \mathrm{R}^{\mathrm{Nx}3\mathrm{N}}$, respectively. $\Omega \in \mathrm{R}^{\mathrm{N}}$ is a matrix with the volumes of the cells. For the temporal discretisation of the momentum equation, a fully explicit second-order scheme on a fractional-step method has been used, while for the pressure-gradient term an explicit first-order scheme has been employed [33]. The governing equations are discretised on a collocated unstructured grid arrangement by means of second-order conservative schemes [34]. Such discretisation preserves the symmetry properties of the continuous differential operators, e.g., the conservation properties are held if the convective term is discretised by a skew-symmetric operator, and the diffusive term is approximated by a symmetric, positive-definite coefficient matrix.

LES modelling has been adopted in this simulation to handle turbulence, in order to reduce computational resources compared to Direct Numerical Simulation (DNS) approach, and allowing an unsteady computation unlike RANS (Reynolds Averaged Navier Stokes) by space filtering. In this simulation, a VMS (Variational Multiscale) model has been selected on the basis of previous work carried out by Torras et al. [32]. The VMS model was originally formulated for the Smagorinsky model by Hughes [35] in the Fourier space, and is a promising approach. In VMS three classes of scales are considered: large, small and unresolved scales. The first two classes are solved with LES-WALE (Large Eddy Simulation Wall-Adapting Local Eddy-viscosity), whereas the unresolved scales are modelled.

2.2.2 Numerical Simulation of In-Tube Single-Phase Flow

The numerical simulation model of the thermal and fluid dynamic behaviour of single-phase flow inside ducts is obtained from the integration of the fluid conservation equations (momentum, continuity and energy) in a one-dimensional way along the tube domain over a finite control volume as shown in Fig. 2.2 (a). Considering that the transient term is evaluated using the first-order approximation ($\partial\phi/\partial t \approx (\phi - \phi^0)/\Delta t$) and that the control volume values are obtained from an arithmetic mean between the inlet w and outlet e faces ($\bar{\phi} \approx (\phi_e - \phi_w)/2$), the semi-discretised governing equations show the following form:

$$\frac{\partial \bar{m}}{\partial t} + \dot{m}_e - \dot{m}_w = 0 \tag{2.4}$$

$$\frac{\partial(\bar{m}\bar{v})}{\partial t} + \dot{m}_e v_e - \dot{m}_w v_w = (p_w - p_e)S - \bar{\tau}\pi D \Delta z p - mgsin\theta \tag{2.5}$$

$$\frac{\partial \bar{m}(\bar{h} + \bar{e}_c + \bar{e}_p)}{\partial t} + \dot{m}_e(\bar{h} + \bar{e}_c + \bar{e}_p)_e - \dot{m}_w(\bar{h} + \bar{e}_c + \bar{e}_p)_w = \dot{Q}_{wall} + V\frac{\partial p}{\partial t} \tag{2.6}$$

This formulation requires the use of empirical correlations to evaluate two specific parameters: the shear stress (usually calculated from a friction factor, $\bar{\tau} = (f/4)(\dot{m}^2/2\rho S^2)$), and the convective heat transfer coefficient used to evaluate the heat transferred between the tube and the fluid ($\dot{Q}_{wall} = \alpha\pi D\Delta z(T_{wall,P} - \bar{T})$).

The flow is evaluated on the basis of a step-by-step numerical implicit scheme. The resulting governing equations are rearranged and solved. Thus, from the duct flow inlet conditions, namely, pressure, enthalpy and mass flow, each control volume outlet state is calculated sequentially. At each control volume the shear stress and the convective heat transfer coefficient are evaluated by means of appropriate empirical correlations. The tube wall temperature map acts as the boundary condition for the whole internal flow at each iteration. More details of the model are found in Morales-Ruiz et al. [31].

The energy balance over the solid part of the tube is also considered. The tube is discretised in a two dimensional way (Fig. 2.2 (b)) and is evaluated with implicit scheme. The resolution procedure is carried out with a line-by-line method, which combines direct method Tridiagonal matrix algorithm (TDMA) and Gauss-Seidel iteration method. The energy equation applied at each solid control volume is expressed as follows:

$$\rho c_p \frac{\partial T_p}{\partial t} S \Delta z_p = \dot{Q}_w + \dot{Q}_e + \dot{Q}_n + \dot{Q}_s \tag{2.7}$$

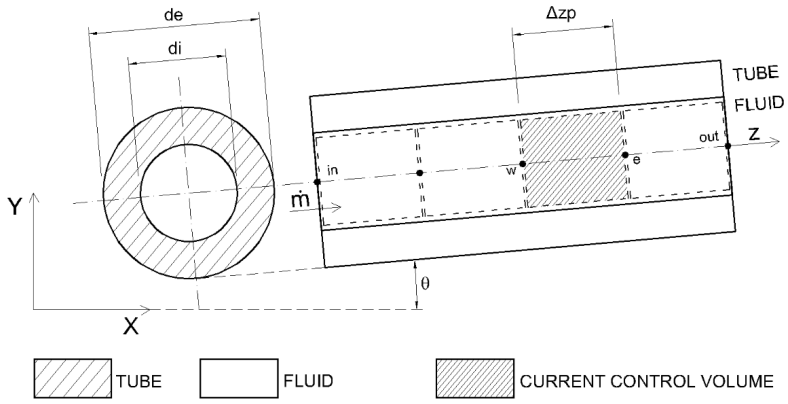

(a)

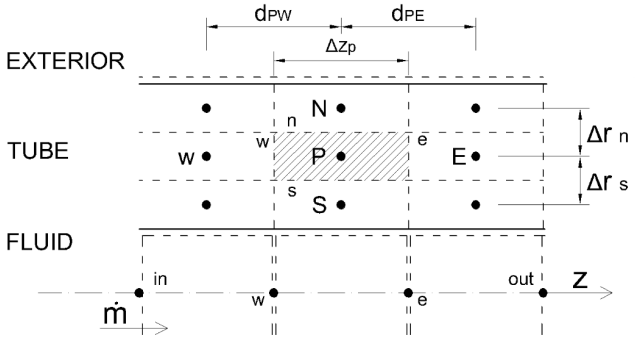

(b)

Figure 2.2: (a) Fluid flow discretisation; (b) tube discretisation.

where $\dot{Q}_s$, $\dot{Q}_n$, $\dot{Q}_e$ and $\dot{Q}_w$ are evaluated from the Fourier law (equation 2.8) for internal nodes.

$$\dot{Q}_i \approx \lambda_i(\frac{T_j - T_P}{d_{Pj}})S_i \tag{2.8}$$

where i = e, w, n, s and j = E, W, N, S and S_i represents the heat flux cross sectional area.

For the boundary nodes, the balance also takes into account the heat exchanged with the internal or external fluids.

Characteristics of Helical Coil in the DWHR storage system

Fig. 2.3 gives the schematic diagram of a helical coil. The pipe has inner and outer diameters equal to d_i and d_e, respectively. The coil has a diameter D_c (measured between the projected centres of the pipes), while the distance between two adjacent turns, called pitch, is p.

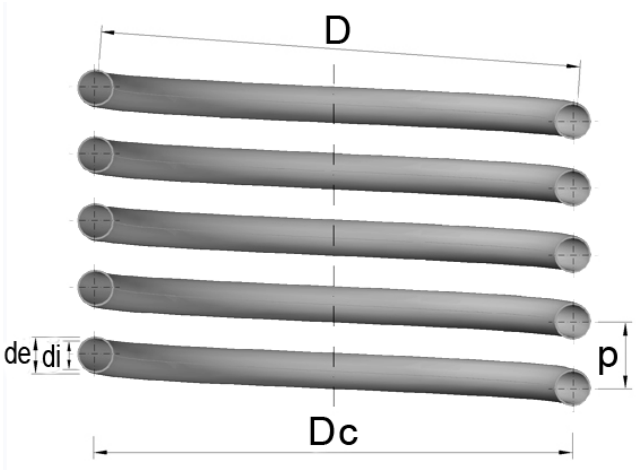

Figure 2.3: Geometry of a helical coil.

Gnielinski [20] defines the diameter of curvature of the coil as D, which is obtained from equation (2.9). Remarkable differences between D and D_c result only for strongly curved tubes and large pitches. For most practical cases, the difference is negligible as p is small compared to D_c. For this reason, many authors do not

distinguish between D and D_c.

$$D = D_c \left(1 + \left(\frac{p}{\pi D_c}\right)^2\right) \tag{2.9}$$

In this work, D is the diameter of curvature used. The relative curvature of the coil is defined as (d_i/D).

Similar to Reynolds number for flow in pipes, Dean number is frequently used to characterise the flow in a helical pipe. The Dean number, De is defined as,

$$De = Re\sqrt{\frac{d_i}{D}} \tag{2.10}$$

The critical Reynolds number for the transition from laminar to turbulent flow in helical coils is a function of the coil parameters. The critical Reynolds number may be determined using the correlation by Schmidt [19].

$$Re_{cri} = 2300\left[1 + 8.6\left(\frac{d_i}{D}\right)^{0.45}\right] \tag{2.11}$$

In this work, the inner convection heat transfer coefficient of the water flowing into the coil is determined from the correlation proposed by Gnielinski [20] (equations (2.12)-(2.14) for the different flow regimes).

Laminar flow regime:

$$Nu = \left(3.65 + 0.08\left\{1 + 0.8\left(\frac{d_i}{D}\right)^{0.9}\right\} Re^m Pr^{\frac{1}{3}}\right)\left(\frac{Pr}{Pr_w}\right)^{0.14} \tag{2.12}$$

$$m = 0.5 + 0.2903\left(\frac{d_i}{D}\right)^{0.194} \tag{2.13}$$

Turbulent flow regime:

$$Nu = \frac{\left(\frac{f}{8}RePr\right)}{1 + 12.7\sqrt{\frac{f}{8}}\left(Pr^{2/3} - 1\right)}\left(\frac{Pr}{Pr_w}\right)^{0.14} \tag{2.14}$$

The factor $(Pr/Pr_w)^{0.14}$ was introduced by Gnielinski into the Schmidt equations [19] to take into account the temperature dependence of the physical properties.

For the transition region $\mathrm{Re}_{cri} < \mathrm{Re} < 22000$, Gnielinski proposes calculated from a linear interpolation of the Nusselt number at Re_{cri} from equation (2.12) and at Re = 22000 from equation (2.14).

The friction factor f in the coiled pipe of circular cross-section is calculated by equations (2.15)- (2.16) (Gnielinski [36]):

Laminar flow regime:

$$f = \frac{64}{Re}\left(1 + 0.33\left(log_{10}De\right)^4\right)k \tag{2.15}$$

Transition and turbulent flow regimes:

$$f = \left(\frac{0.3164}{Re^{0.25}} + 0.03\left(\frac{d_i}{D}\right)^{1/2}\right)k \tag{2.16}$$

Woschni [37] in his experiments observed a decrease of the friction factors with increasing difference between the wall temperature and the mean temperature of the fluid. For this reason a correction factor (k) is introduced using the dynamic viscosity (μ).

$$k = \left(\frac{\mu_w}{\mu}\right)^{0.27} \tag{2.17}$$

2.3 Experimental Setup

An experimental unit has been built to study drain water heat recovery storage systems. The unit provides reliable measurements of their thermal-hydraulic performance. Furthermore, the experiments were carried out to produce the required data for the boundary conditions definition and results validation of the numerical simulations. The experimental unit is thus designed to supply hot and cold water to a DWHR storage device (test section), and to study its performance accumulating and delivering energy.

Besides the DWHR storage device, the experimental unit is made up of two water tanks, two thermal baths, a water pump, a flow meter, a differential pressure sensor, several temperature sensors, valves and pipes. A schematic diagram of the experiment unit is shown in Fig. 2.4.

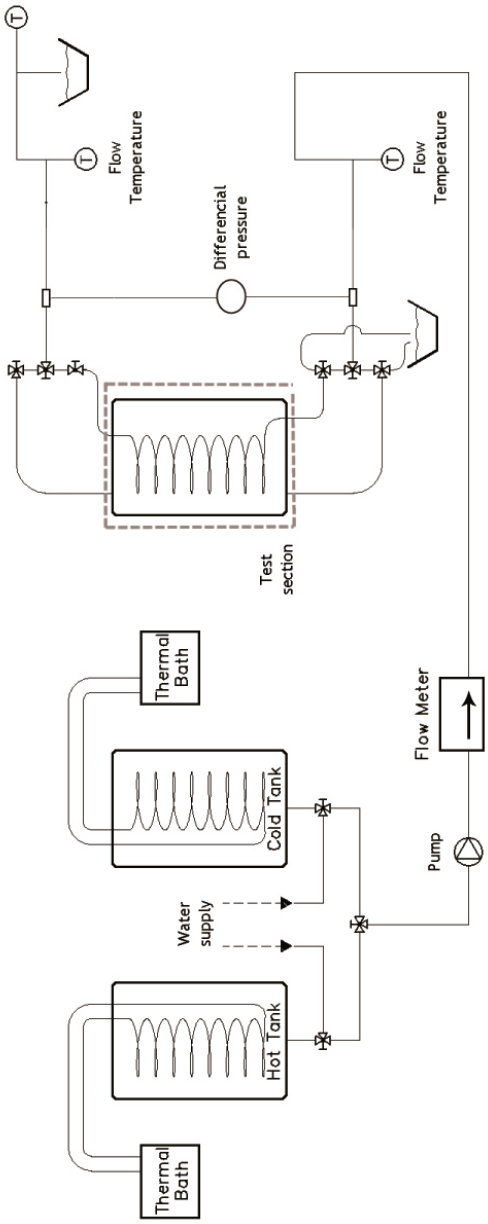

Figure 2.4: Schematic representation of the experimental unit.

The water tanks are used to pump hot or cold water into the test section. Each water tank temperature is controlled by a thermal bath by means of a coiled pipe. These tanks are linked to the test section through valves and pipes, as shown in Figs. 2.4 and 2.5.

Figure 2.5: Detailed view of the experimental unit.

The water mass flow rate is measured by a Coriolis mass flow meter with an accuracy of ± 0.041 % of the actual flow rate within the operating range. The in-tube water inlet and outlet temperatures are measured with K-type thermocouples with an accuracy of ± 0.3 °C. The water pressure drop is obtained from a differential pressure transducer with an accuracy of ± 0.04 % F.S.

The Agilent 34970A data acquisition and control module was used coupled with a LabView data logging and control software application.

The experiments were performed in a climatic chamber in order to control the environmental conditions: the temperature of the chamber was kept constant during the experiments. In addition, all the elements of the experimental facility such as tanks and pipes have been fully insulated to reduce heat losses. A commercial insulation has been used (25 mm insulation thickness) for this purpose.

2.3.1 Test Section

The test section is a drain water heat recovery storage device that consists of a tank with a coiled pipe inside it. The tank is filled with hot water used to store heat while the coiled pipe is used to absorb this energy by means of cold water flowing through it. Fig. 2.6 shows the instrumented test section, the thermocouples position and its placement in the experimental unit.

The tested tank is cylindrical, the height and the diameter are 350 mm and 250 mm, respectively, and its storage capacity is 15.72 l. It is made of stainless steel and covered with an insulation layer. Eleven calibrated K-type thermocouples with an

accuracy of ± 0.3 °C are placed inside the accumulator in order to measure the water temperature at different radii and heights. The coiled pipe is made of cooper with a defined external and internal diameter of 15.87 mm and 14.27 mm, respectively. The tube pitch is 25.44 mm. Three calibrated K-type thermocouples (accuracy of ± 0.3 °C) are located at the beginning, middle and end of the pipe surface. The inlet tube to the test section is 1.1 m length with an internal diameter of 14.27 mm and a thickness of 1.6 mm. The length of the outlet tube of the test section is 900 mm with the same internal diameter and wall thickness to the inlet tube. These tubes are covered with a commercial insulation layer (20 mm insulation thickness).

2.3.2 Experimental Procedure

During the operation time of this DWHR storage device three steps take place: the accumulator fluid charge, energy storage and the heat extraction process. In the charging process the tank is filled with hot water coming from hot water tank. When the tank is full of water, the storage process begins and it finishes when the extraction (discharging) process starts. Finally, the stored energy is extracted in the discharging process by cold water pumped through the accumulator coiled pipe. At this point, all the operational steps are completed.

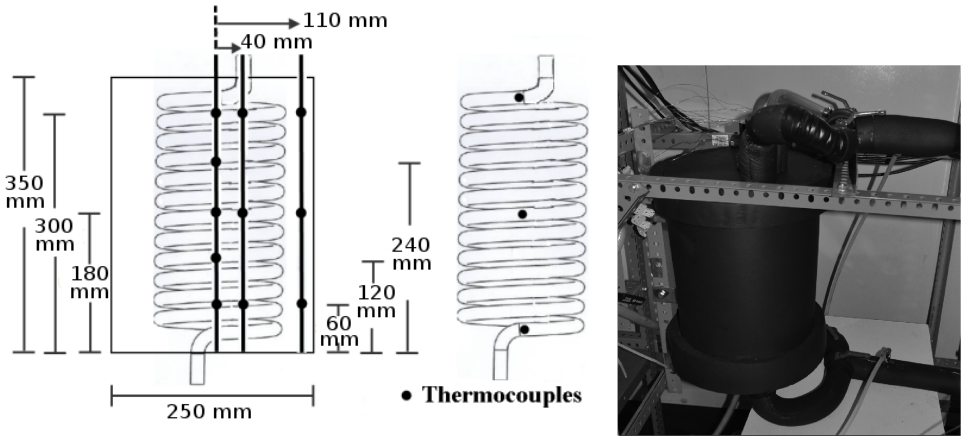

Figure 2.6: (a) Test section, thermocouples located inside the accumulator at different radii and heights; (b) instrumented and mounted in the experimental unit.

An uncertainty analysis has been applied to evaluate the errors influence of the different variables measured on the experimental results, which is based on a propagation error methodology proposed in the technical literature [38, 39]. The maximum uncertainty estimated for the heat transfer rate is around $\pm$11.98 %, while $\pm$7.88 % was obtained as a maximum uncertainty for the energy recovered during the thermal extraction process.

2.4 Results

The performance of a DWHR storage device is characterized by different parameters such as the storage capacity, the heat transfer rates during charging and discharging and the storage efficiency.

The authors consider that for both the experimental and numerical tests carried out, the heat extraction and the storage processes are the most relevant steps to be analysed. The charging process is less critical for the design of this type of DWHR (it mainly depends on the filling water amount and temperature).

The non-dimensional temperature shown in the results is calculated as $T^* = (T - T_{min})/(T_{max} - T_{min})$, where T_{min} is the minimum temperature of the water flow through the coiled pipe, T_{max} the initial maximum temperature of the water inside the accumulator in every test condition of the DWHR.

2.4.1 Test Conditions

The experiments and the numerical simulations for the discharging process are conducted for three different flow rates through the coil and for two different values of initial water temperature at the in-tank (60 °C and 34 °C) defined as high (HT) and intermediate (MT) temperatures, respectively. The in-tube cold water is about 15 °C. Parameters tested in this study are shown in Table 2.1. The inlet and the outlet tubes has been taking into account in the simulations.

And additional experimental test have been carried out to study the heat loss to the environment during the storage period of the DWHR storage device. In this test, the initial water temperature at the in-tank was the high temperature (HT).

2.4.2 Mesh refinement studies and Boundary Conditions used in the numerical simulations

The DWHR storage device analysed numerically consists of a tank full of high-temperature water and a coiled pipe through which low-temperature water circulates absorbing the energy of the water contained in the tank. The device dimensions have been defined previously in the section 2.3.1.

Test	Flow rate [l/min]	$Tini_{in-tank}{}^*$	$Tini_{in-tube}{}^*$	$V_{in-tank}$ [l]	$V_{extractionProcess}$ [l]
1	3	1.0 (MT)	0.0	15.72	20
2	6				
3	9				
4	3	1.0 (HT)			
5	6				
6	9				

Table 2.1: Test conditions.

In order to evaluate the adequacy of the spatial discretisation, computations have been performed on different meshes. Extensive mesh refinement tests have been conducted. A fine near wall mesh is necessary to correctly solve the boundary layer and the physical phenomena associated with the coiled pipe wall. Thus, a prism layer is appropriate in this area due to the low non-orthogonal corrections required by this type of elements.

Three different unstructured meshes are generated attaining the aforementioned criteria to carry out extensive mesh refinement studies. The finest and the coarsest meshes have about 2.0 and 0.68 million elements, respectively. All the meshes guarantee sufficient CVs within the boundary layers, an a priori estimate of the boundary layer has shown that for the studied mean Prandtl number, the thermal boundary layer is thinner than the viscous one as $\delta_t \sim H/Ra^{0.25}$ and $\delta_v \sim Pr^{0.25}\delta_t$ [40]. Details of the tested meshes are shown in Fig. 2.7.

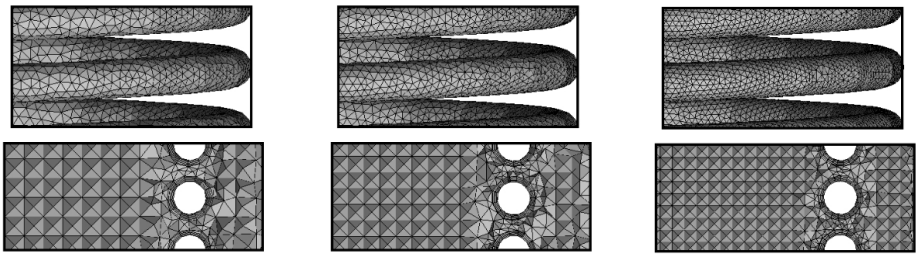

Figure 2.7: Comparison of the unstructured meshes used for the fluid inside the tank: (left) mesh I; (centre) mesh II; (right) mesh III.

A thorough comparison of the main parameters of the DWHR storage has been

carried out using Test 1. Comparisons have shown good agreement for meshes II and III resulting in, for example, relative differences of as low as 1.2% and 2.2% for the outlet temperature of the in-tube water at the final instant and the energy recovered for the DWHR storage device, respectively. Considering these two meshes, the results are in fairly good agreement with the experiment, even though mesh II (this mesh has about 1.0 million elements (Fig. 2.8)) is twice as coarse as mesh III. Mesh II has been selected in this work, because the computational time factor was reduced twice and within acceptable results.

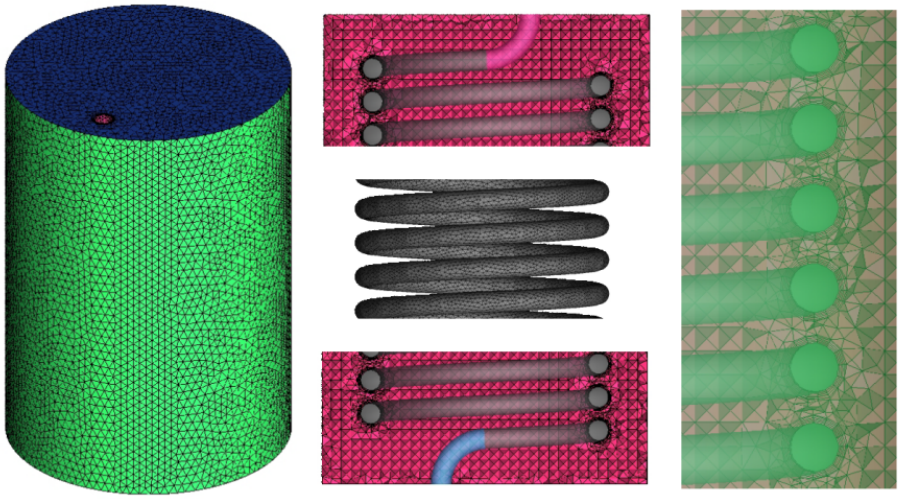

Figure 2.8: Views of the unstructured mesh used for the fluid inside the tank.

The coiled pipe is discretised with a Cartesian grid of 268 x 4 control volumes and the internal fluid flowing through it has 268 control volumes.

The boundary conditions for the fluid inside the tank have been considered with and without heat losses at the tops and sides of the tank during the extraction process. These conditions have been compared using the Test 1 and 4 (with the longest time tests). The results with and without considering the heat losses are highly similar, this is because the heat loss during the extraction process tests are less than 0.1% of the total energy contained in the tank. For this reason, the boundary conditions for the fluid inside the tank are considered adiabatic. And the boundary condition for the fluid flow inside the pipe are: temperature inlet (T_{in}), mass flow inlet ($\dot{m}_{in}$), and pressure inlet (P_{in}), values obtained from the experiments.

2.4.3 Extraction Process results

For the heat extraction process, both the storage temperature and the water flow rate inside the coiled pipe were studied experimentally and numerically as having a large effect on the extraction energy rate. For each initial temperature (HT and MT), the water flow rate in the coil were 3, 6 and 9 l/min.

A comparison between the numerical and experimental results has been carried out for the different flow rates and temperatures considered. Fig. 2.9 shows the evolution of the outlet non-dimensional temperature of the in-tube water for the different tests. In general, good agreement can be appreciated between experimental data and numerical results. The numerical results follow the transient evolution of the temperature correctly, although with small differences between them. The results for the final instant show that all the compared test remain within an relative error below 2.5% (err = 100abs((T$_{outletExp}$-T$_{outletNum}$)/T$_{outletExp}$)[%]). The peak observed in the different tests is due to the water which is initially contained within the coiled pipe and is hotter than the water entering it. These results revealed that the rise in the temperature of the fluid was significantly affected by the flow rate reduction. This effect is caused because the heat transfer rate rises by a smaller proportion than the flow rate.

Experimental and numerical results of the in-tank water non-dimensional temperature along the height of the tank for the all tests are shown in Fig. 2.10. It can be observed that the water temperature at the final instant is decreasing with more intensity in the bottom part of the tank, because the inlet of the cold water in-tube is located in that area of the tank. The numerical results followed a trend similar to the experimental data for the different flow rates. Furthermore, it can be seen the influence of the flow rates on the temperature distribution. Fig. 2.10 also shows that in the lower part of the tank the measured values are modelled quite accurately. However, the measured values in the upper sensor (h= 300 mm) show distinctly higher deviations between experiment and simulation. The authors believe it is due to the fact that the upper part of the tank is a very sensitive zone, because this sensor is located at the end of the coil. This causes large temperature changes in small elevation, as shown in Fig. 2.10 (a) for the test with intermediate temperature. But it also leaves open the possibility of weaknesses of the numerical models and insufficient mesh refinement in the external boundaries (top, bottom, and lateral surface) and in the core of the tank for the test with high temperature. In addition, the authors are aware of the necessity to add extra sensors in this region (upper part) for the experiment.

Another interesting variable to show in the extraction process is the percentage of energy recovered for the DWHR storage device for the different flow rates and temperatures considered (Fig. 2.11). The heat transfer rate was calculated based on the mass flow rate, $\dot{m}$, the specific heat of the in-tube fluid, c_p, and the difference in inlet and outlet temperatures ($T_{out} - T_{in}$).

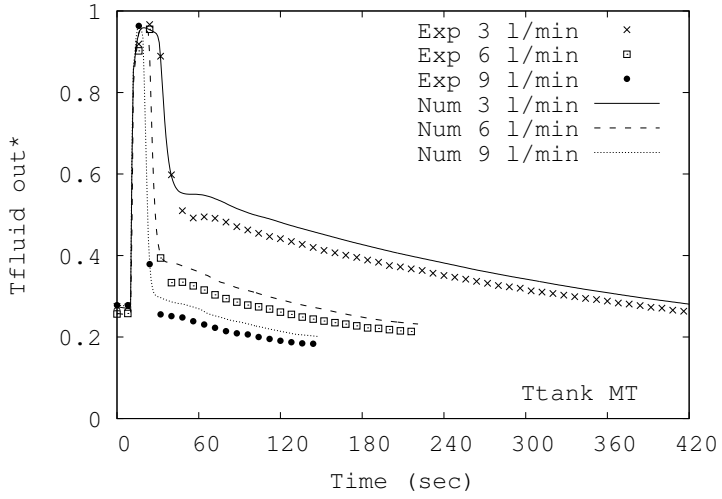

(a)

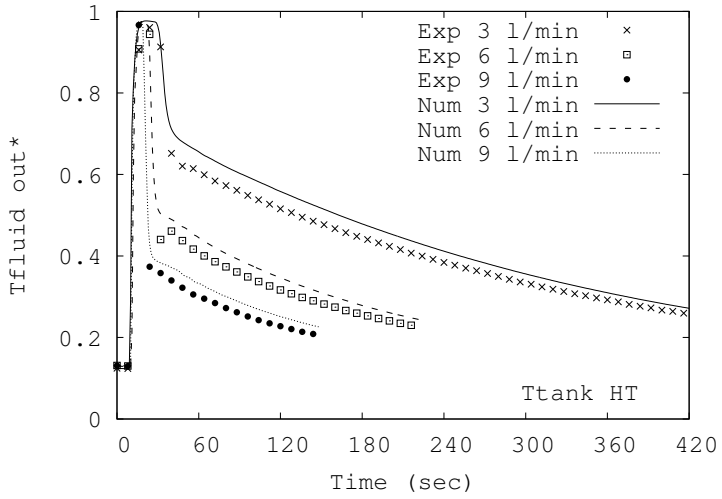

(b)

Figure 2.9: Extraction process: comparison between the numerical simulation and the experiments of the outlet non-dimensional temperature of the in-tube water for different flow rates for in-tank water with: (a) intermediate temperature; (b) high temperature.

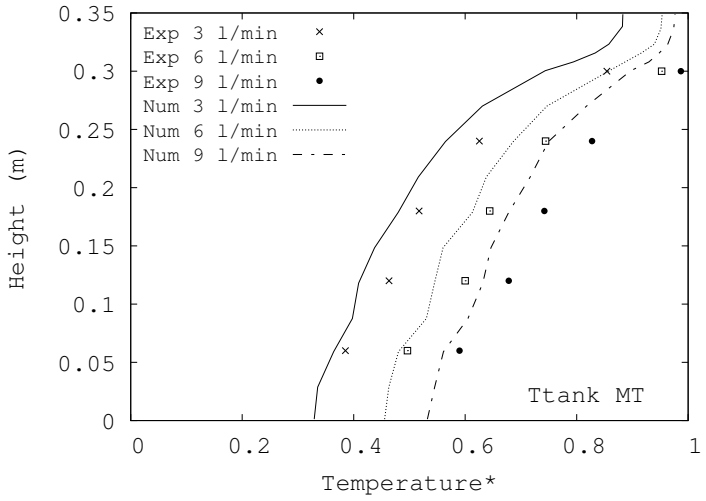

(a)

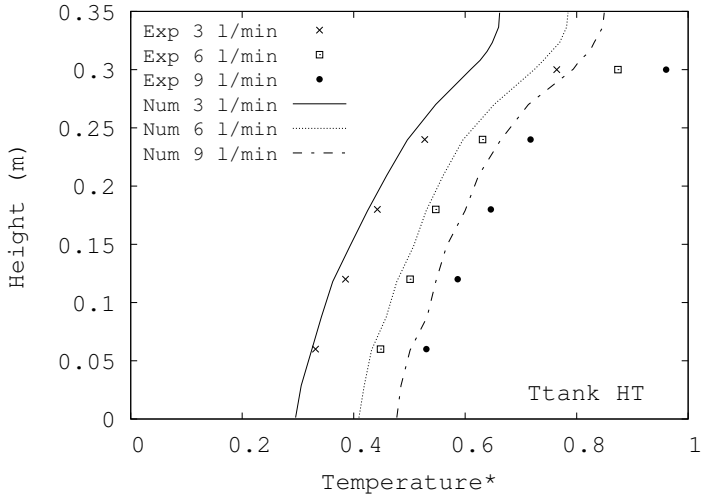

(b)

Figure 2.10: Extraction process: comparison between the numerical simulation and the experiments of the non-dimensional temperature of the in-tank water at the final instant: (a) tests with intermediate temperature; (b) tests with high temperature.

The total energy delivered by the in-tank water is the integration of the heat transfer rate during the test. The total energy recovered or delivered is made dimensionless by dividing by the total energy contained in the in-tank water at the initial time test with respect to the minimum inlet temperature of the in-tube water. It is shown that the in-tube flow rate is the dominating parameter.

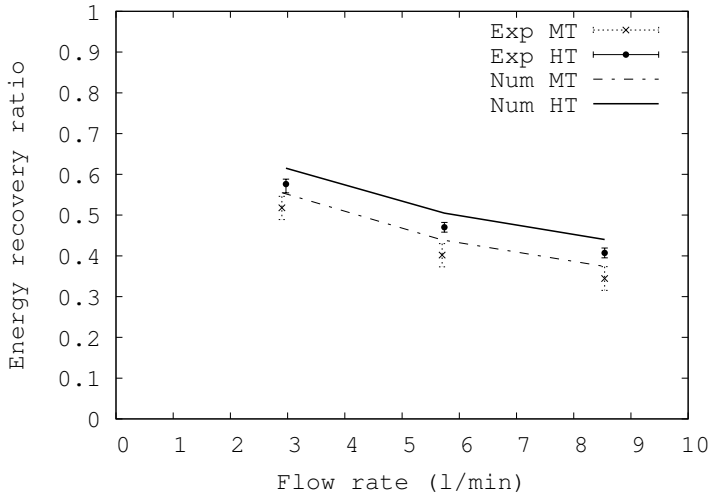

Figure 2.11: Extraction process: comparison between the numerical simulation and the experiments of the energy recovery ratio for different flow rates.

Detailed comparisons between the experimental and numerical results for Test 1 (MT, 3 l/min) are shown below. Figs. 2.12 (a), 2.12 (b) and 2.13 (a) show the evolution of the non-dimensional temperature over time at different locations inside the accumulator in the DWHR storage device. The greater effect of the height on the temperature can be clearly seen, while smaller effect was determined in the radial direction. A reasonable agreement can be appreciated between experiment and numerical simulation. However, discrepancies have been found in the temperature of the in-tank water located at a height of 300 mm. As explained above, the authors believe this may be due to the position of the coil that produces a very sensitive zone, possible weaknesses of the numerical models and insufficient mesh refinement. Two extra sensors have been added numerically at heights of 305 and 310 mm to appreciate the transient behaviour of the DWHR storage in this zone.

The non-dimensional temperature of the in-tube water along the time at different

positions are shown in Fig. 2.13 (b). Fig. 2.13 (b) shows that the rise of temperature is reduced over time due to the cooling process in the in-tank water. Furthermore, Fig. 2.13 (b) shows a good agreement between the numerical simulations and experiments. The numerical simulations performed seem to reasonably predict the transient behaviour of the in-tube water.

Fig. 2.14 (a) shows the profile along the time of the heat transfer rate from the in-tank water to the in-tube water. As would be expected, the profile of the heat transfer rate has the same behaviour as the outlet temperature of the in-tube water. The evolution over time of the total energy delivery ratio by the DWHR storage device as shown in Fig. 2.14 (b).

For the case studied, the numerical results and measured results show a high degree of correspondence. Good agreement was also attained for the heat transfer rate and the total energy delivery ratio. However, small discrepancies were identified in the non-dimensional temperature over time at height 300 mm inside the accumulator. Regarding the in-tube water, the numerical results show an acceptable agreement with the experimental data in the DWHR storage during the extraction process.

The numerical model provides additional and more detailed information of the heat extraction process at any time of the natural movement of the water and the temperature distribution inside the DWHR storage. Figs. 2.15 and 2.16 show the 3D streamline and the transient evolution of the non-dimensional temperature of the water in the tank, respectively, for Test 1. The cooled tank water near the coiled pipe wall travels down and moves through the tubes forming streams which advance towards the bottom of the tank. These streams of cooled water interact continuously with the water in the core. When the streams in the bottom arrive to the centre and to the lateral wall of the tank, upward streams are formed as shown in Fig. 2.15, and in greater detail at 60 seconds in Fig. 2.16. As the interaction between the cooled water on the coiled pipe wall and the water in the core continues, the stratification of the fluid temperatures advances from the bottom to the top, see Fig 2.17. Furthermore, it is seen how the in-tank water temperature decreases progressively from bottom to top of the tank getting closer to the in-tube inlet temperature, due to the energy delivery process to the in-tube water.

The average outer Nusselt number ($\overline{Nu_o}$) is defined in this problem as a function of the fluid (in-tank) and the wall (coiled pipe) temperatures. The Nusselt number is numerically calculated in this work and can be defined as:

$$\overline{Nu_o} = \frac{L_{ref}}{\Delta T_{ref} S} \int_S \frac{\partial T}{\partial n} ds \tag{2.18}$$

where, ΔT_{ref} =($T_{in-tank,t=0}$ - $T_{in-tube,inlet}$), L_{ref} is the characteristic length, and S is the outer surface of coiled pipe. For this work the coil height is taken as characteristic length.

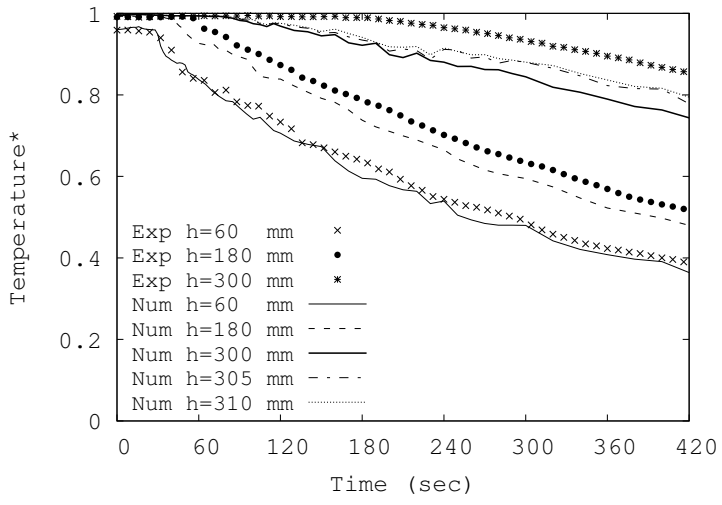

(a)

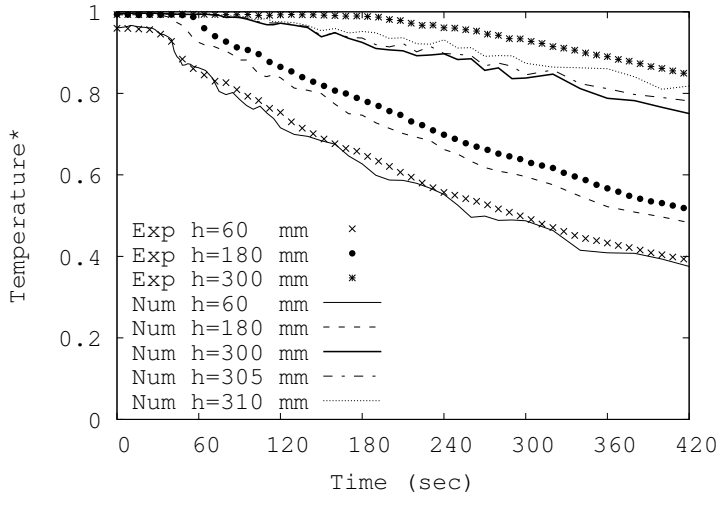

(b)

Figure 2.12: Test 1: Transient evolution of non-dimensional temperature of the in-tank water at different positions: (a) r= 0; (b) r= 40 mm.

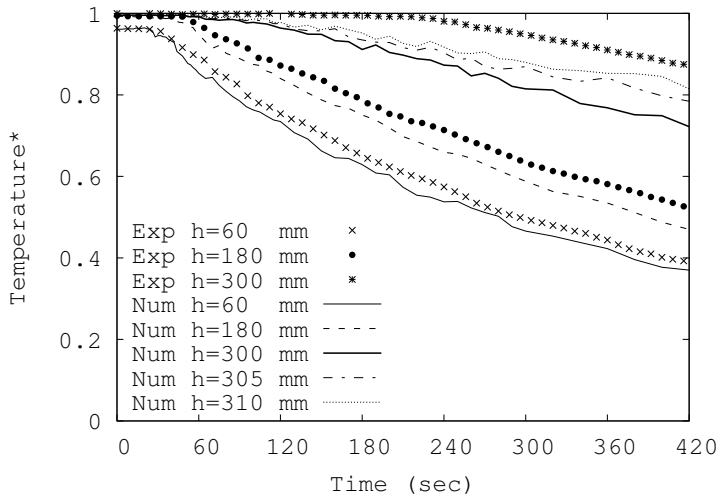

(a)

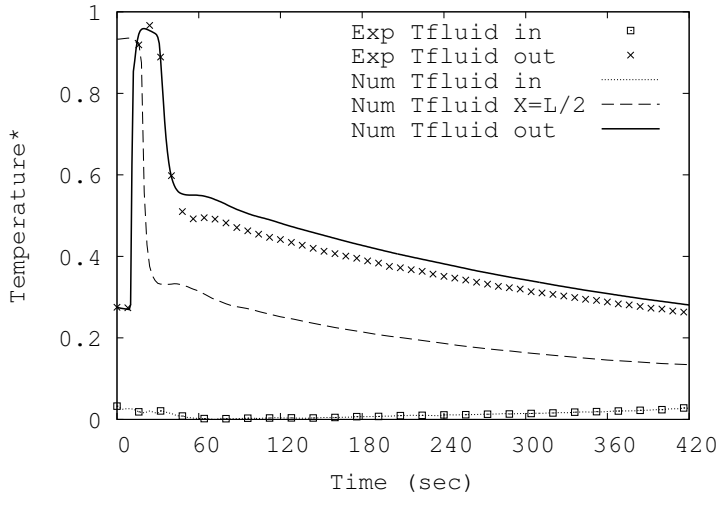

(b)

Figure 2.13: Test 1: Transient evolution of non-dimensional temperature of: (a) the in-tank water at r= 110 mm; b) the in-tube water at different positions.

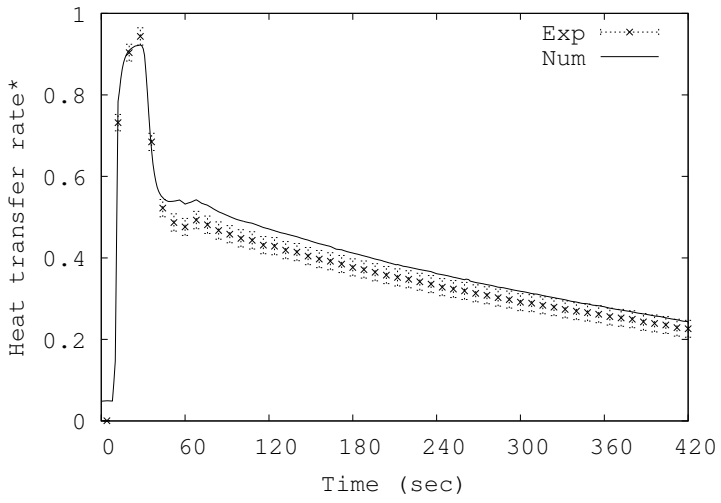

(a)

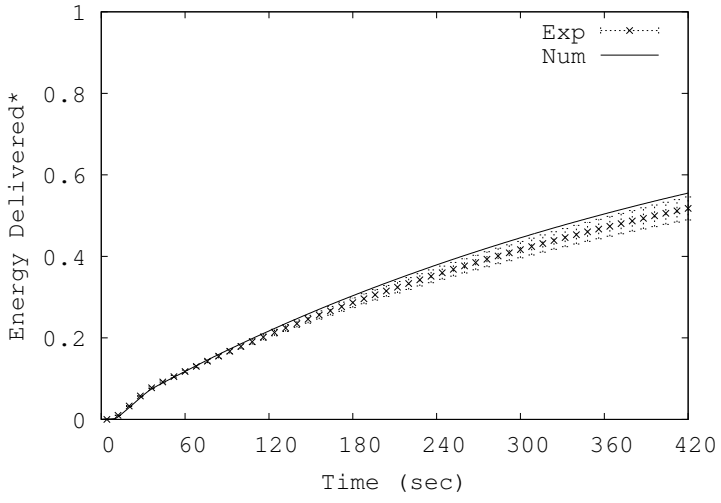

(b)

Figure 2.14: Test 1: Transient evolution of: (a) non-dimensional heat transfer rate; (b) the energy delivery ratio of the device.

(a) 30 s. (b) 60 s. (c) 120 s.

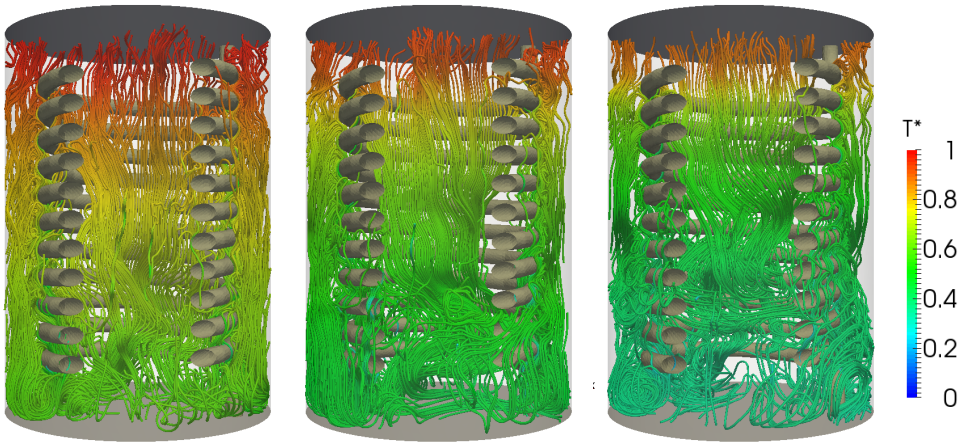

(d) 180 s. (e) 300 s. (f) 420 s.

Figure 2.15: Test 1: in-tank water 3D streamline for different instants of time (s).

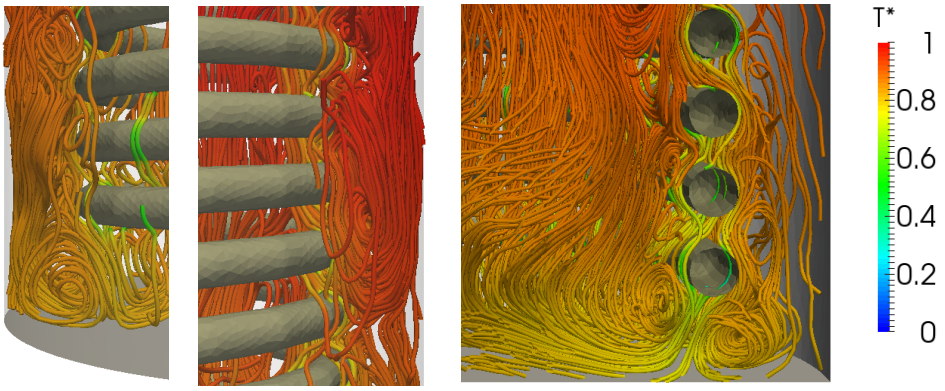

Figure 2.16: Test 1: in-tank water 3D streamline detail at 60 seconds.

Fig. 2.18 shows the evolution of the average outer Nusselt number for intermediate temperature (MT)and flow rates of 3 l/min (a) and 9 l/min (b). The Nusselt number behaviour is described by means of a curve divided into two zones. Zones 1 corresponds to the initial evolution of the Nusselt number, increasing until it reaches a maximum value. At first, there is a strong increase in the temperature difference between the wall and the in-tank water promoted by the inlet in-tube water. While in zone 2, the Nusselt number decreases at a constant rate with time as the difference between the in-tank water and the wall temperature decreases. It is also observed that the Nusselt number increases with the flow rate.

2.4.4 Storage Process results

For storage process a test of heat loss to the environment of the DWHR storage device has been carried out experimentally, considering an initial non-dimensional temperature of 1.0 (HT) for the water inside the tank. The test was performed in a climatic chamber, where its non-dimensional temperature was kept constant during the experimental test at 0.11. The duration of the heat loss test was 60 hours.

In Fig. 2.19 the vertical non-dimensional temperature measurements of the in-tank water are plotted over the duration of the test. These results show that the bottom of the storage dropped in temperature little more than the other temperature sensors located directly above. An exponential decay of the water temperature inside the tank during the test period was observed. It was also noted that there were no significant temperature gradients in the radial direction. Additionally, the

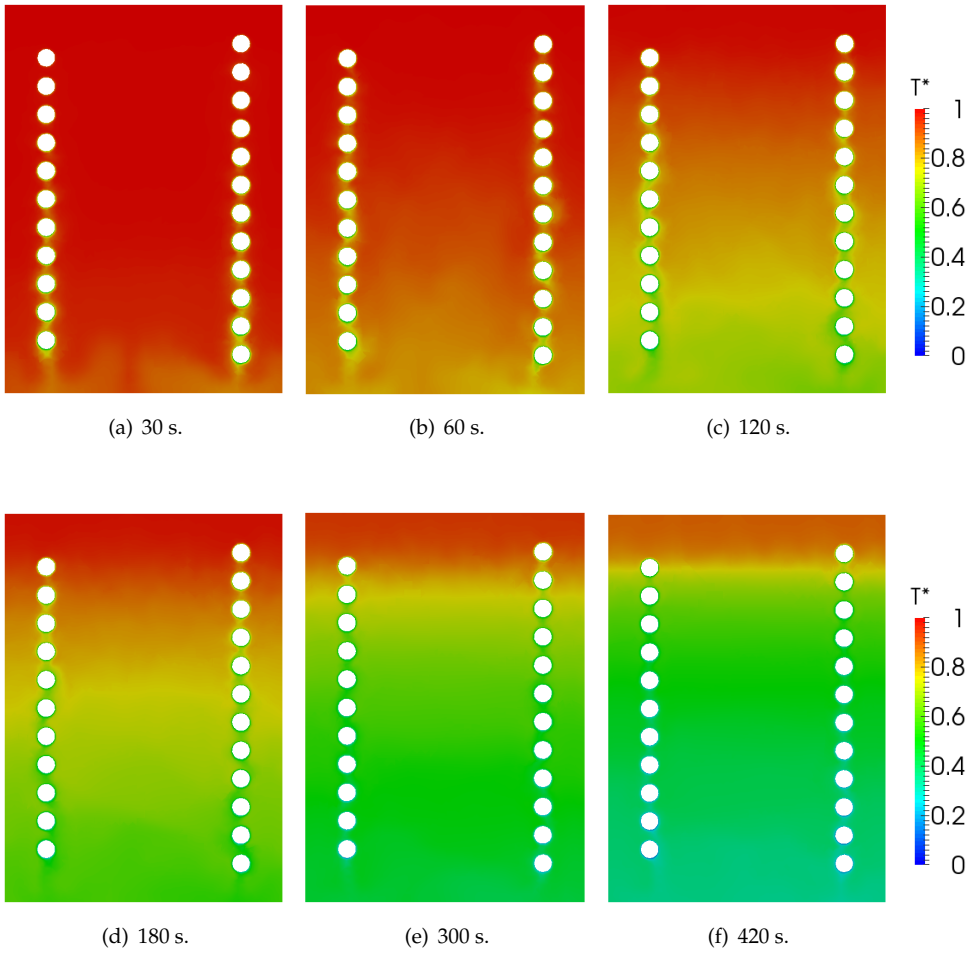

(a) 30 s. (b) 60 s. (c) 120 s.

(d) 180 s. (e) 300 s. (f) 420 s.

Figure 2.17: Test 1: in-tank water non-dimensional temperature for different instants of time (s).

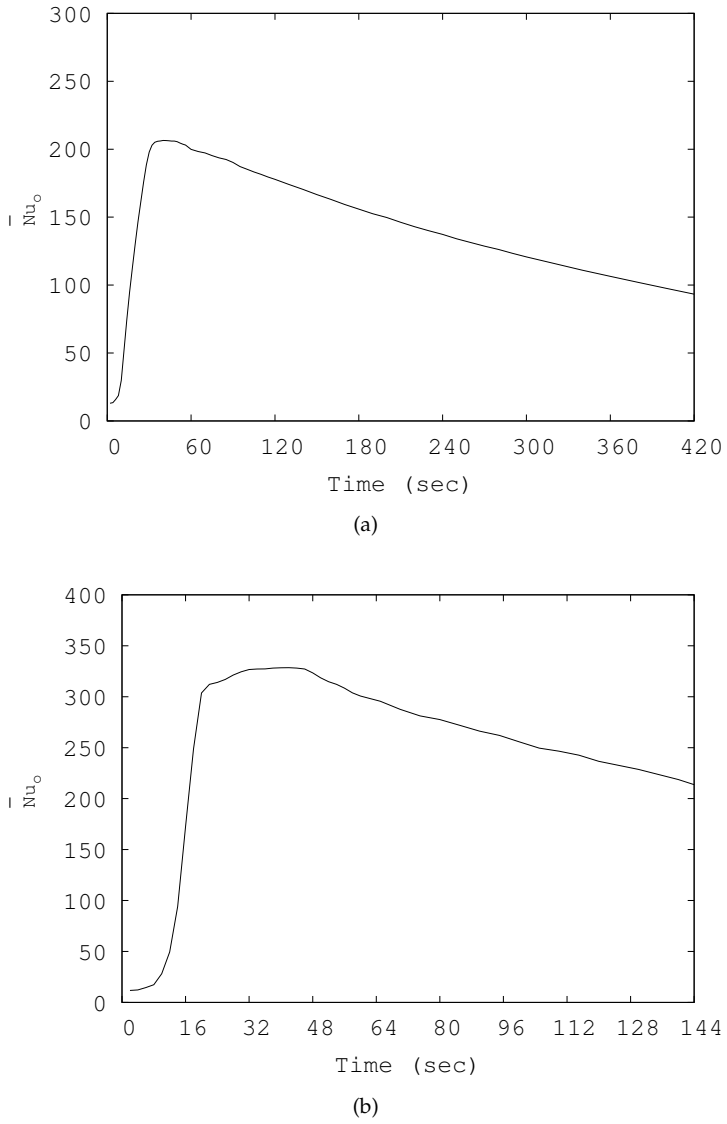

Figure 2.18: Evolution of the overall outer Nusselt number for intermediate temperature (MT) and flow rates: (a) 3 l/min and (b) 9 l/min.

available energy in the DWHR storage device with time has been obtained from the experimental data Fig. 2.20. This available energy is calculated with respect to the initial instant and for use in the extraction process with cold water. The DWHR storage device has been insulated with a 25 mm closed cell elastomeric insulation layer (λ=0.04 W/m.K). A 50% reduction in stored energy is observed at 24 h, which reveals its limitations for long-term storage applicability.

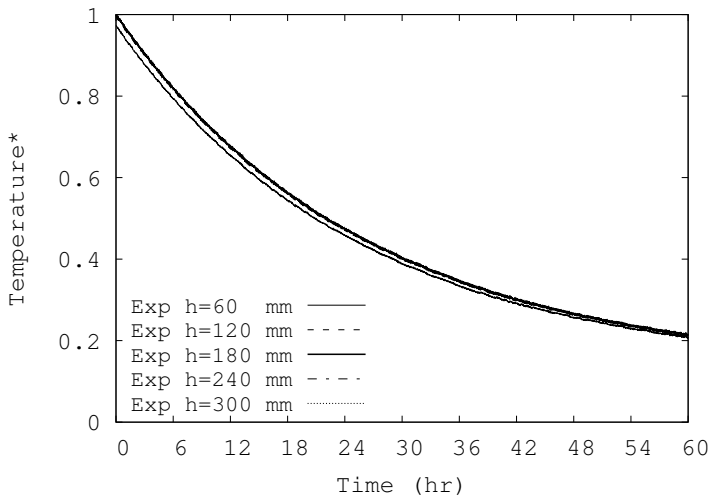

Figure 2.19: Storage process: evolution of non-dimensional temperature of the in-tank water at different positions in r=0.

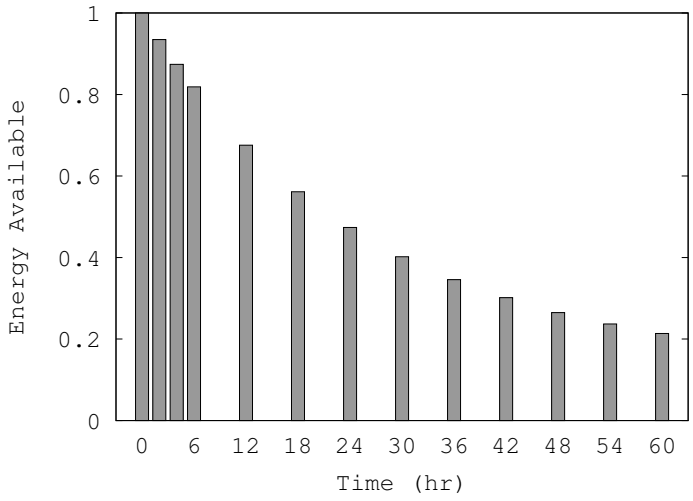

Figure 2.20: Storage process: available energy in the DWHR storage device with time.

2.5 Concluding Remarks

A specific drain water heat recovery storage-type based on a cylindrical tank with an internal coiled pipe has been built. In this work both numerical and experimental tools have been used to design and study the performance of this device.

An experimental unit has been constructed. The unit provides reliable measurements of the temperatures at different locations (in-tank and in-tube) and the flow rate, to study the storage capacity and the delivering energy process of the DWHR storage device. The experiments have generated the required data for the boundary conditions definition and results for validation of the numerical simulations.

A numerical simulation platform has been adapted for the prediction of the DWHR storage system. This platform will be applicable to future versions of DWHR storage (geometric configuration and operational condition). The numerical simulation provides additional and more detailed information of the DWHR storage, such as the natural movement of the in-tank water.

Extraction process tests were conducted to determine the effect of flow rate and temperature in the heat recovery performance of the DWHR storage device. For the DWHR storage built in this work, the maximum heat recovered is reached at the lowest flow rates (3 l/min) for the two different in-tank temperatures. The DWHR stor-

age had the capacity to recover from 60% - 34% of the energy available in the drain water for the investigated flow rates. It has been concluded that the in-tube mass flow rate has noticeable impact (18% difference between the smallest and largest values) on the energy recovered from the DWHR storage at both high and intermediate temperatures. In addition, the greater effect of the height on the temperature can be clearly seen, while a smaller effect was determined in the radial direction.

In these tests a comparison between the numerical and experimental results has been carried out. Different results of the DWHR storage device are shown, such as the evolution of the non-dimensional temperature over time of the water in-tank and in-tube and the energy recovery ratio, where the numerical results were shown a trend similar to the experimental data for the different tests. The evolution of non-dimensional temperature at the outlet of the in-tube water and for the in-tank water in the lower part of the tank (h $<$ 300 mm) are modelled quite accurately. The numerical results follow the transient evolution of the temperature correctly. However, the measured values in the upper sensor (h= 300 mm) shows distinctly higher deviations between experiment and simulation. The authors leave open the possibility of weaknesses of the numerical models and insufficient mesh refinement in the external boundaries and in the core of the tank. But in general, the numerical results show a good agreement with the experimental data of the presented experiments. The numerical simulations performed seem to predict reasonably the transient behaviour of the DWHR storage device.

A heat losses test was conducted on the insulated DWHR storage device to determine the heat loss characteristics. There were no significant temperature gradients in the radial direction. A 50% reduction in stored energy is observed at 24 h, which reveals its limitations for long-term storage applicability.

The drain water heat recovery is one efficient and low-cost technology to reduce energy costs and environmental impact. The objective of these devices is the recovery of the waste heat from domestic warm drain water and transferring it to cold water entering the house. From the results, it can be concluded that the objective has been reached with the proposed design.

Acknowledgments

This work has been financially supported by the Ministerio de Economía y Competitividad, Secretaría de Estado de Investigación, Desarrollo e Innovación, Spain (CEN-20091005), by the project “SEILA” New technologies for an efficient, ecologic and intelligent washing system for textiles of the future (Ref. C07973).

References

[1] DOE, 2011 buildings energy data book. U.S. Department of Energy, 2011.

[2] Energy Consumption in the UK (2014). Department of Energy & Climate Change, London SW1A 2AW. Webpage: http://www.gov.uk/decc, 2014.

[3] P.J. Boait, D. Dixon, D. Fan, A. Stafford. Production efficiency of hot water for domestic use. *Energy and Buildings*, 54, 2012.

[4] C.M. Leidl, W.D. Lubitz. Comparing domestic water heating technologies. *Technology in Society*, 31, 2009.

[5] A. Cooperman, J. Dieckmann, J. Brodrick. Drain Water Heat Recovery. *ASHRAE Journal 2011*, 2011.

[6] C. Zaloum, M. Lafrance, J. Gusdorf. Drain water heat recovery characterization and modeling, Final draft. Sustainable Building and Communities, Natural resurces, Canada, 2007.

[7] A. McNabola, K. Shields. Efficient drain water heat recovery in horizontal domestic shower drains. *Energy and Buildings*, 59, 2013.

[8] L.T. Wong, K.W. Mui, Y. Guan. Shower water heat recovery in high-rise residential buildings of Hong Kong. *Applied Energy*, 87, 2010.

[9] X. Liu, L. Ni, S.K Lau, H. Li. Performance analysis of a multi-functional Heat pump system in heating mode. *Applied Thermal Engineering*, 51, 2013.

[10] W. Chen, S. Liang, Y. Gou, K. Cheng. Investigation on the thermal performance and optimization of a heat pump water heater assisted by shower waste water. *Energy and Buildings*, 64, 2013.

[11] J. Wallin, J. Claesson. Investigating the efficiency of a vertical inline drain water heat recovery heat exchanger in a system boosted with a heat pump. *Energy and Buildings*, 80, 2014.

[12] L. Ni, S.K. Lau, H. Li, T. Zhang, J.S. Stansbury, J. Shi, J. Neal. Feasibility study of a localized residential grey water energy-recovery system. *Applied Thermal Engeneering*, 39, 2012.

[13] D.G. Prabhanjan, G.S.V. Raghavan, T.J. Rennie. Comparison of the heat transfer rates between a straight tube heat exchanger and helically coiled heat exchanger. *Int. Comm. Heat Mass Transfer*, 29:185–191, 2002.

[14] W.R. Dean. Note on the motion of fluid in a curved pipe. *Philosophical Magazine*, 4:208–223, 1927.

[15] W.R. Dean. The stream-line motion of fluid in a curved pipe. *Philosophical Magazine*, 5:673–695, 1928.

[16] H. Ito. Friction factors for turbulent flow in curved pipes. *Trans. Amer. Soc. Mech. Eng. J.*, 81:123–132, 1959.

[17] R. Seban, E.F. McLaughlin. Heat transfer in tube coils with laminar and turbulent flow. *Int. J. Heat Mass Transfer*, 6:387–395, 1963.

[18] G.F. Rogers, Y.R. Mayhew. Heat transfer and pressure loss in helically coiled tubes with turbulent flow. *Int. J. Heat Mass Transfer*, 7:1207–1216, 1964.

[19] E.F. Schmidt. Wärmeübergang und Druckverlust in Rohrschlangen. *Chem. Ing. Tech.*, 39:781–789, 1967.

[20] V. Gnielinski. Heat transfer and pressure drop in helically coiled tubes. In *Proceeding 8th Int. Heat Transfer Conference*, 6:2847–2854, 1986.

[21] A.N. Dravid, K.A. Smith, E.W. Merrill, P.L.T. Brian. Effect of secondary fluid motion on laminar flow heat transfer in helically coiled tubes. *AIChE J.*, 17:1114–1122, 1971.

[22] M.E. Ali. Experimental investigation of natural convection from vertical coiled tubes. *Int. J. Heat Mass Transfer*, 37:665–671, 1994.

[23] M.E. Ali. Free convection heat transfer from the outer surface of vertically oriented helical coils in glycerol-water solution. *Heat and Mass Transfer*, 40:615–620, 2004.

[24] R.C. Xin, M.A. Ebadian. Natural convection heat transfer from helicoidal pipes. *Journal of Thermophysics and Heat Transfer*, 10:297–302, 1996.

[25] R.C. Xin, M.A. Ebadian. The effects of prandtl numbers on local and average convective heat transfer characteristics in helical pipes. *Journal of Heat Transfer*, 119:467–473, 1997.

[26] D.G. Prabhanjan, T.J. Rennie, G.S.V. Raghavan. Natural convection heat transfer from helical coil tubes. *International Journal Therm. Sci.*, 43:615–620, 2004.

[27] J. Fernández-Seara, C. Piñeiro-Pontevedra, J.A. Dopazo. On the performance of a vertical helical coil heat exchanger. Numerical model and experimental validation. *Applied Thermal Engineering*, 62:680–689, 2014.

[28] J. Lopez, O. Lehmkuhl, R. Damle and J. Rigola. A parallel and object-oriented general purpose code for simulation of multiphysics and multiscale systems. In *Proceedings of the 24th International Conference on Parallel Computational Fluid Dynamics*, 2012.

[29] R. Damle, O. Lehmkuhl, G. Colomer, I. Rodríguez. Energy simulation of buildings with a modular object-oriented tool. In *Proceedings of the ISES World Conference*, 2011.

[30] O. Lehmkuhl, C.D. Pérez-Segarra, R. Borrell, M. Soria, A. Oliva. TERMOFLUIDS: A new Parallel unstructured CFD code for the simulation of turbulent industrial problems on low cost PC Cluster. In *Proceedings of the Parallel CFD 2007 Conference*, 2007.

[31] S. Morales-Ruiz, J. Rigola, C.D Pérez-Segarra and O. García-Valladares. Numerical analysis of two-phase flow in condensers and evaporators with special emphasis on single-phase/two-phase transition zones. *Applied Thermal Engineering*, 29:1032–1042, 2009.

[32] S. Torras, O. Lehmkuhl, J. Rigola and A. Oliva. Numerical simulation of heat storage for domestic applications. In *Proceedings of the 23rd IIR Int. Congress of Refrigeration*, 2011.

[33] F.X. Trias, O. Lehmkuhl. A self-adaptive strategy for the time integration of Navier-Stokes equations. *Numer. Heat Transfer Part B*, 60:116–134, 2011.

[34] R.W.C.P. Verstappen, A.E.P. Veldman. Symmetry-preserving discretization of turbulent flow. *J. Comput. Phys.*, 187:343–368, 2003.

[35] T.J.R. Hughes, L. Mazzei and K.E. Jansen. Large eddy simulation and the variational multiscale method. *Computing and Visualization in Science*, 3:47–59, 2000.

[36] V. Gnielinski. Zur Berechnung des Druckverlustes in Rohrwendeln. *Vt-Verfahrenstechnik*, 17:683–690, 1983.

[37] G. Woschni. Untersuchung des Wärmeübergangs und des Druckverlusts in gekrümmten Rohren. *Dr. -Ing. Diss. Universität Karlsruhe*, F.R.G. 1985.

[38] R.J. Moffat. Describing the uncertainties in experimental results. *Experimental Thermal and Fluids Science*, 1:3–17, 1998.

[39] H.W. Coleman, W.G. Steele. Experimentation and uncertainty analysis for engineers. John Wiley and Sons, Inc. New York, 1998.

[40] D. Kizildag, I. Rodríguez, A. Oliva, O. Lehmkuhl. Limits of the Oberbeck-Boussinesq approximation in a tall differentially heated cavity filled with water. *International Journal of Heat and Mass Transfer*, 68:489–499, 2014.

Chapter 3

Numerical Modelling and Experimental Validation of a Thermal Energy Accumulator for Propulsion Systems Under Cryogenic Conditions

Abstract.

The In-Space Propulsion project (ISP-1) [1] was initiated with the objective of improving the knowledge and the techniques related with cryogenic propulsion which are necessary for future space missions. The ISP-1 project presented various technological difficulties associated to the development of a Low Thrust Cryogenic Propulsion (LTCP) system [1]. One of them is its energy management, e.g. the non-coincidence of the refrigeration needs of the fuel cells with the needs of propellants gasification and tanks pressurisation. For this reason a LTCP system needs a thermal energy storage acting as a heat accumulator, where a cryogenic flow of liquid nitrogen (LN_2) propellant is gasified inside, under a fast transient evaporation process. The heat accumulator is heated by means of a secondary fluid (typically helium or nitrogen) that removes the heat from the fuel cells. The thermal energy stored in the accumulator is performed by means of a Phase Change Material (PCM). In this work, a numerical model of the thermal and fluid-dynamic behaviour of the two-phase flow inside ducts working under cryogenic conditions, coupled with the analysis of the thermal accumulator (with or without PCM) is proposed [2]. The numerical analysis is based on: i) a one-dimensional and transient resolution of the governing equations (conservation of mass, momentum and energy) for the fluid flow of propellant; ii) a multi-dimensional and transient resolution of the governing equations in the region occupied by the PCM, incorporating a model for the turbulence to solve the convection phenomena involved; iii) the solid elements are modelled considering a multidimensional and transient treatment of the thermal conduction equation. The numerical results are experimentally validated by means of a series of experimental tests [3].

The heat accumulator used in this work for validation of the models was develop by Leiner et al. [4]. The comparative analysis shows a good agreement between both numerical results and experimental data. The experimental validation under different working conditions of the cryogenic flow and/or the PCM material, shows the possibilities of this model for design optimization purposes.

3.1 Introduction

Since the beginning of the space travel, rockets propelled by chemical propulsion systems are the most widely used technology in spacecraft propulsion to overcome Earth's gravity. These technologies are capable of producing the magnitude of thrust necessary. In these systems the energy to generate the thrust is obtained by chemical reactions by forcing a gas from the rear of the vehicle at very high speed through a supersonic de Laval nozzle. However, once in orbit, this propulsion system has a significant limitation, due to its relatively low specific impulse (I_{SP}) if they are compared with other emerging technologies such as electric propulsion [5, 6]. The chemical propulsion has a fixed amount of energy per unit mass, which limits the achievable exhaust velocity or specific impulse. However, because the rate at which the energy can be supplied by the propellant is independent of their mass, it implies that a very high powers and thrust levels can be achieved [7].

The spacecraft usually have a second propulsion system with a higher I_{SP} and thus being able to travel in space. This system is called in-space propulsion, and it is the technology capable of generating the thrust necessary for a spacecraft to travel through space. Actually, the main objective of this technology is to allow the propulsion of the spacecraft to move from one orbit to another or make minor corrections. The requirements for in-space propulsion vary widely according to their intended application [8–10].

The In Space Propulsion-1 (ISP-1) project [1] was initiated with the objective of improving the knowledge and the techniques which are necessary for future space missions that are related with cryogenic propulsion. The ISP-1 project does not focus on the early launch phase, but on the technologies involved in the subsequent phases of a space mission, once the spacecraft has already been placed in orbit. The idea of using cryogenic propulsion is because toxic propellants with poor propulsion performance are frequently used. The cryogenic propulsion, on the other hand, produces non–toxic/harmless exhaust gases and the specific impulses are much higher. Cryogenic liquids are liquefied gases that are kept in their liquid state at very low temperatures. These liquids are extremely cold and have boiling points less than -150°C . All cryogenic liquids are gases at normal temperatures and pressures. The cryogenic liquids most used are: liquid hydrogen (LH_2), liquid oxygen (LO_X), liquid nitrogen (LN_2), liquid methane (LCH_4), among others. Nowadays, cryogenic propulsion based on LO_X propellant is a mature field and a core technology [11]. In-space cryogenic fluid management has been of interest to NASA since the 1960s for scavenging cryogenic propellants [12]. LO_X/LH_2 also powered the upper stages of the Saturn V and Saturn IB rockets, as well as the Centaur upper stage, the United States' first LO_X/LH_2 rocket (1962). Plans for integrated cryogenic propellant flight demonstrations have been carried out since the end of the decade of the 1980s, such as COLD-SAT [13]. The COLD-SAT studies was conducted in the early 1990s [13]

and summarized by NASA in 1998 [14]. The COLD-SAT was intended to provide sufficient data on the storage and handling of cryogens (specifically liquid hydrogen) in the low gravity environment of space to enable future space systems to be confidently and efficiently designed. For its part, ESA worked on the first Ariane launcher as early as 1974, using a cryogenic technology of combining liquid oxygen and liquid hydrogen. The Ariane rocket family has evolved over the years to meet the demands of the market. For over 30 years, Ariane rockets have been the mainstay of European space launch capabilities. The reliability and versatility of Ariane rockets has allowed them to become one of the worlds premier commercial satellite launchers. The HM7B is a European cryogenic upper stage rocket engine used in Ariane rocket family. The development of HM7 engine begun in 1973 on a base of HM4 rocket engine [15]. It was designed to power a third stage of newly constructed Ariane 1, the first launch system for ESA. The HM7 will be replaced by Vinci as an upper-stage engine for Ariane 5 [16]. Vinci is currently under development. The Soviet Union did not even test a (LH_2) upper stage until the mid-1980s [17]. The Russians are now designing their Angara rocket family with liquid-hydrogen upper stages [18].

The basic system studied in the ISP-1 is the low thrust cryogenic space propulsion (LTCP) system (see Fig. 3.1), that is mainly composed of hydrogen and oxygen propellant tanks, propellant pumps, a fuel cell, heat accumulators, a main combustion chamber, attitude control thrusters and, a fuel cell cooling circuit. One of the components, the heat accumulator, stores the thermal energy from the fuel cell that provides electrical energy to the whole system. This thermal energy is employed for the pressurization of the propellant tanks and gasification of the propellant to the combustion chamber. Two different types of heat accumulators are present in the LTCP system: the High Temperature Accumulator (HTA) and the Low Temperature Accumulator (LTA). The HTA provides the thermal energy for the self-pressurisation of the hydrogen tank and the LTA provides thermal energy for the self-pressurisation of the oxygen tank [4]. The fuel cells have an operating optimum temperature at about +80°C.

The base idea of this kind of in-space propulsion system is the Low Cost Cryogenic Propulsion (LCCP) concept [19], which was previously patented by Société Nationale d'Études et de construction de moteurs d'Aviation (SNECMA) [20]. The aim of saving energy by heat accumulators starts from the fact that on the one hand, a cooling of the fuel cells is necessary, which provide electrical energy for the spacecraft, and therefore also some sort of cooling device is needed. On the other hand, thermal energy is necessary during the engine operation, especially at the starting of the engines, in order to: i) pressurise the tanks themselves by the help of vaporization of their corresponding propellant and; ii) a better combustion in the combustion chamber. However, the refrigeration needs of the fuel cell are not coincident in gen-

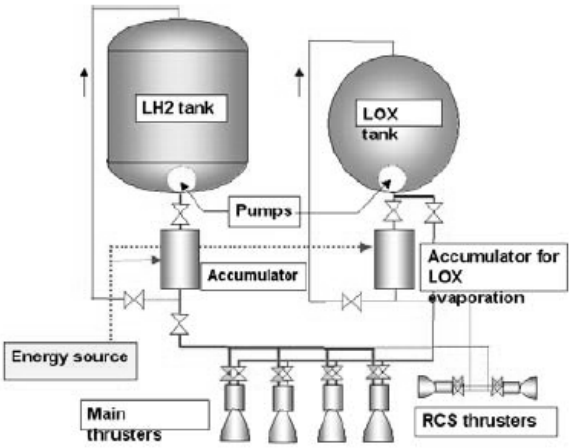

Figure 3.1: Schematic of a low thrust cryogenic stager (figure extracted from [1]).

eral with the needs of propellant gasification. For this reason, energy storage is of special interest.

This study is focused on the Low Temperature Accumulator based on water as PCM [1, 19]. The water was tried as the optimum working fluid, due to its high phase change heat, and the range of the temperatures of the LTA: from -200 °C approximately, that is the temperature of the LN_2 evaporation, up to +80 °C, the working temperature of the fuel cell. The design of the experimental test device of the LTA was oriented to the validation of the model. It consists on a cylindrical container with a tube located inside it in the center. The container filled partially with the PCM.

Four different experimental test types [3] were designed in order to reproduce all the possible working conditions in the LTA accumulator, see Fig. 3.2. All the combinations of melting/solidification at the water-ice PCM, together evaporation/single flow for the LN_2/N_2 stream have been reproduced in the experimental test device. Depending on the case, these operations involves accumulation and disaccumulation of the thermal energy in the in-tank fluid (water) in a fast transient process.

In this work, a numerical model of the thermal and fluid-dynamic for the whole LTA accumulator. It consists in the modelling of the two-phase flow inside ducts working under cryogenic conditions (propellant flow), coupled with the analysis of the tank partially filled with PCM. The numerical analysis is based on: i) a one-dimensional and transient resolution of the governing equations (conservation of

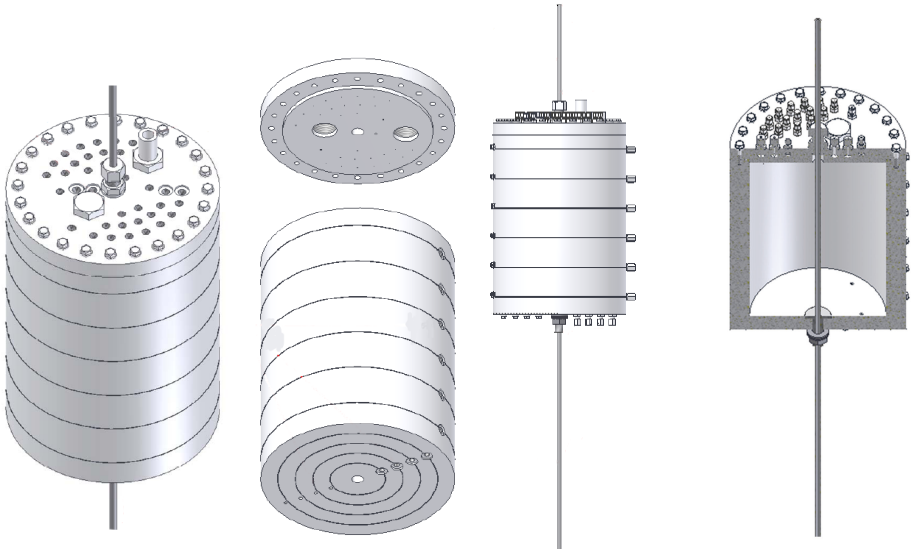

Figure 3.2: Schematic views of the experimental setup of the LTA at DLR (figures extracted from [3, 4]).

mass, momentum and energy) for the fluid flow of propellant; ii) a multi-dimensional and transient resolution of the conservative governing equations in the region occupied by the PCM, incorporating a model for the turbulence to solve the convection phenomena involved; iii) the solid elements are modelled considering a multidimensional and transient treatment of the thermal conduction equation. Finally, an overall energy balance for the gas (air) contained into the tank, is performed in order to calculate its medium temperature.

The numerical results are experimentally validated against the experimental tests. The comparative analysis shows the good agreement between both numerical results and experimental data. The agreement under different working conditions of the cryogenic flow and/or the PCM material, shows the possibilities of the models proposed for design optimization purposes.

3.2 Mathematical Model & Numerical Implementation

The thermal energy storage tank considered is formed by different elements: The two fluids (water and air) inside tank, the tube and the in-tube fluid (nitrogen), which interact with each other through their boundary conditions. The model developed is based in the coupling of three models/subroutines: i) single flow/two phase flow 1D inside the tubes; ii) heat conduction in solid parts; and iii) modelling of the PCM together with turbulent convection outside tube. An additional overall energy balance is performed in order to calculate the temperature of the air ullage inside the tank. A brief mathematical description is presented in the following subsections.

3.2.1 Numerical simulation of the fluid inside the tube

The two-fluid model is inter-penetrating, capable of defining the behaviour of the velocity, the pressure, the temperature and the distribution of each one of the phases, gas and liquid, separately [21].

The assumed hypotheses in the two-fluid model are: one-dimensional flow, constant cross section and, negligible axial heat conduction in fluid. The governing equations for the two-phase fluid flow are:

Conservation of mass:

$$\frac{\partial}{\partial t}\left[\rho_l \varepsilon_l\right] + \frac{\partial}{\partial z}\left[\rho_l \varepsilon_l v_l\right] = -\Gamma_g \tag{3.1}$$

$$\frac{\partial}{\partial t}\left[\rho_g \varepsilon_g\right] + \frac{\partial}{\partial z}\left[\rho_g \varepsilon_g v_g\right] = \Gamma_g \tag{3.2}$$

Conservation of momentum:

$$\frac{\partial}{\partial t}\left[\rho_l \varepsilon_l v_l\right] + \frac{\partial}{\partial z}\left[\rho_l \varepsilon_l {v_l}^2\right] = -\varepsilon_l \frac{\partial p}{\partial z} - g\rho_l \varepsilon_l sin\theta - \frac{P_{w,l}\tau_{w,l}}{s} + \frac{P_i \tau_{i,l}}{s} - \Gamma_g \bar{v}_{il} \quad (3.3)$$

$$\frac{\partial}{\partial t}\left[\rho_g \varepsilon_g v_g\right] + \frac{\partial}{\partial z}\left[\rho_g \varepsilon_g {v_g}^2\right] = -\varepsilon_g \frac{\partial p}{\partial z} - g\rho_g \varepsilon_g sin\theta - \frac{P_{w,g}\tau_{w,g}}{s} + \frac{P_i \tau_{i,g}}{s} + \Gamma_g \bar{v}_{ig} \quad (3.4)$$

Conservation of energy:

$$\frac{\partial}{\partial t}\left[\rho_l \varepsilon_l h_l\right] + \frac{\partial}{\partial z}\left[\rho_l \varepsilon_l h_l v_l\right] = \frac{\dot{q}_{il} P_{il}}{s} - \frac{\dot{q}_{w,l} P_{w,l}}{s} - \Gamma_l h_{il} + \varepsilon_l \frac{\partial p}{\partial t} \quad (3.5)$$

$$\frac{\partial}{\partial t}\left[\rho_g \varepsilon_g h_g\right] + \frac{\partial}{\partial z}\left[\rho_g \varepsilon_g h_g v_g\right] = \frac{\dot{q}_{ig} P_{ig}}{s} - \frac{\dot{q}_{w,g} P_{w,g}}{s} + \Gamma_g h_{ig} + \varepsilon_g \frac{\partial p}{\partial t} \quad (3.6)$$

Where the heat transfer exchanged at the interface and the heat transferred from the wall to the liquid and gas phase has been evaluated by means of empirical expressions [22, 23]. The discretization of the governing equations has been developed by means of finite volume techniques. The two-phase flow phenomena of propellant inside the primary tube (evaporation phenomena) are simulated considering the two-fluid model and are solved by means of semi-implicit pressure based method (SIMPLE), which shows a good stability in the calculation [24]. More details about the formulation and the definition of the regime used for the simulation of the in-tube fluid can be found in reference [25].

3.2.2 Numerical simulation of fluid inside the tank

The phase change phenomenon of the PCM is simulated by means of the numerical resolution of the Navier-Stokes together with energy equations using a multidimensional model (2D or 3D). Some of the most relevant simplifying assumptions that are made are [26]:

- Incompressible fluid.
- Boussinesq approximation (density is considered constant, except in the volumetric forces term).
- Constant thermo-physical properties.

Based on the above mentioned hypotheses and adopting the enthalpy-porosity model to account for the phase change phenomenon [27, 28], the mass, momentum and energy conservation equations can be written in the following form:

Conservation of mass:

$$\nabla \cdot \vec{u} = 0 \tag{3.7}$$

Conservation of momentum:

$$\frac{\partial(\rho\vec{u})}{\partial t} + (\vec{u} \cdot \nabla)\vec{u} = -\nabla p_d + \mu\nabla^2\vec{u} - \rho\epsilon g\beta(T - T_0)\hat{j} - S\vec{u} \tag{3.8}$$

Conservation of energy:

$$\frac{\partial(\rho h)}{\partial t} + \nabla \cdot (\rho\vec{u}C_{pl}T) = \nabla \cdot (\lambda\nabla T) \tag{3.9}$$

where $\vec{u}$ is the seepage velocity (or Darcy velocity), which is defined as the average fluid velocity over a representative volume that may contain both liquid and solid phases [29]. The enthalpy h includes both sensible and latent components. The source term $-S\vec{u}$ is introduced into the momentum equation to account for the presence of solid in the control volumes. Its value depends on the porosity ϵ (or liquid fraction). To solve these equations, it is necessary to define a relation between enthalpy and temperature of the PCM. In this work, the change of phase is considered at a fixed temperature. On the other hand, a fixed grid is used for the numerical resolution in the entire domain (including liquid, solid and interface), where the liquid fraction determines the state of the substance in each control volume. Liquid fraction with values between 0 and 1 indicates the presence of both phases in the same mesh node. These nodes are called "interface" nodes [26].

3.2.3 Numerical simulation of the solid tube

For the solid parts, the heat conduction equation (3.10) is considered:

$$\rho C_p \frac{\partial T}{\partial t} = \nabla.(\lambda\nabla T) \tag{3.10}$$

The wall tube temperature distribution is obtained after solving the discretized energy equation, where the heat flux due to conduction between tube and PCM, and the heat convection between tube and fluid flow have been considered as boundary conditions. The tube is discretized in a two dimensional way and is evaluated with an implicit scheme. The resolution procedure is carried out with a line-by-line method [30], which combines the direct method Tridiagonal matrix algorithm (TDMA) and the Gauss-Seidel iterative method.

3.2.4 Numerical simulation of the gas contained

Additionally, the gas ullage (air), e.g. the region between the PCM top surface and the top wall of the container should also be considered in the global methodology, as it affects to the heat losses. Similar to the other objects, the gas ullage is linked through its boundary conditions with the PCM surface and the tank walls. In this work, this element is used as a generator of dynamic boundary conditions.

$$\frac{\partial(\rho C_p T)}{\partial t} = \dot{Q}_{tube} + \dot{Q}_{pcm} + \dot{Q}_{top} + \dot{Q}_{lateral} \tag{3.11}$$

where $\dot{Q}_{tube}$, $\dot{Q}_{pcm}$, $\dot{Q}_{top}$ and $\dot{Q}_{lateral}$ take into account the heat exchanged with the tube, internal (PCM) and external fluids (ambient). The heat transfer exchanged at the interface and the heat transferred between the gas and the PCM inside the tank, the gas with the tube and with the tank walls are evaluated by means of empirical expressions [31].

3.2.5 Coupled resolution

As commented, the numerical algorithm takes into account, in a coupled manner, the resolution of the different elements of the system: i) the two-phase fluid flow of propellant inside the primary tubes (evaporation phenomena); ii) the phase change of the PCM (solid-liquid) in the tank; iii) the heat conduction through the solid elements (the tubes), see Fig. 3.3 (a); and iv) the heat transfer in the gas contained.

In each time step iteration the resolution is carried out in three steps.

- The first one consists of solving the in-tube flow together with the solid part of the tube. The boundary condition for each control volume is the heat flux calculated in the previous iteration from the PCM and the gas inside the tank. From this process a new temperature map for the tube is obtained.

- The second step consist on calculating the gas temperature by means an overall energy balance in the gas ullage, with the tube temperature map and the heat flux with the PCM calculated obtained in the previous step.

- The third step consist on solving the PCM inside the tank using the CFD model, with the tube and the gas temperature map obtained in the previous step.

This implementation has been performed within the NEST platform [32], which allows linking between different elements of the thermal system. Each of these elements can be solved independently and by using different levels of modelling (from

global to fully three-dimensional models). On the other hand, the CFD&HT (Computational Fluid Dynamics & Heat Transfer) calculations in the PCM have been performed using a parallel, non-structured and an in-house CFD&HT software, called TermoFluids [33].

In these simulations, the algorithm used for the resolution of the system of equations (comprising the fluids inside tank, the tube and the in-tube fluid) is a Gauss-Seidel type algorithm adapted to facilitate the coupling between the different parts of the system.

The boundary condition at the interface is the last temperature profile sent by the external wall tube during the internal fluid loop, and it is updated with the new temperature profile sent by the external wall tube once the time scales have the same order of magnitude. The subroutine of calculation of the fluid inside the tank sends to the tube domain the heat flux between these two domains (fluid inside the tank and the tube) and it is used as boundary condition at the interface for the tube.

The Fig. 3.3(b) shows the exchange of information of the different subroutines/ models. By one hand, the tube subroutine gives temperature and, on the other hand, the multidimensional (3D or 2D) subroutine gives heat flow. In the parallel computing calculation, particularities were used attempting to save computational costs on unnecessary communications between domains and to help the convergence of the in-tube fluid, the fluid inside the tank domain is forced to work within an internal loop in order to accumulate heat until the sum of fluid time steps is of the order of one in-tube fluid coherent time scale.

The meshes used for the fluid inside the tank are coincident with the mesh used in the tube. In order to facilitate the exchange of information. On the other hand, in order to achieve a compromise between accuracy in the results and a reasonable CPU time calculation, depending on the case a 2D or 3D multidimensional resolution has been chosen for the PCM inside the tank. The different cases are explained in the next section.

In order to evaluate the adequacy of the spatial discretisation, computations have been performed on different meshes for the different test cases. A mesh refinement tests have been conducted. Refinement of the mesh near the wall tube is necessary to correctly solve the boundary layer and the physical phenomena associated with the tube wall. Three meshes are used with each case, see Table 3.1 for details. The meshes for the fluid inside the tank are generated attaining the aforementioned criteria to carry out mesh refinement studies. The tube is discretized with a 2D Cartesian grid, and the in-tube fluid with a 1D mesh (see Fig. 3.4).

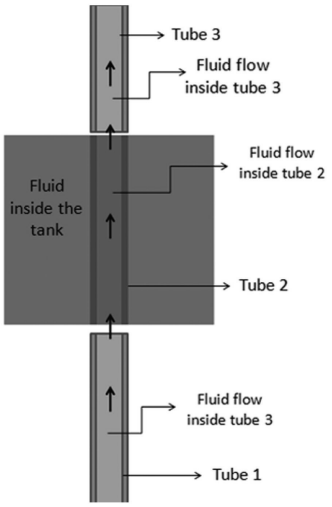

(a)

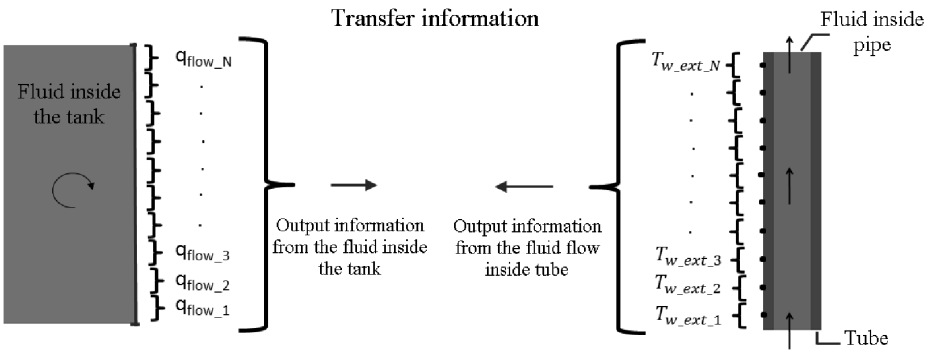

(b)

Figure 3.3: (a) Low temperature accumulator; (b) data exchange between PCM (water and/or ice) and the wall tube.

Mesh	Fluid inside the tank		Tube	In-tube fluid
	Type	NCV	Nx x Ny	Nx
I	3D structured	136800	78 x 4	78
II		228000	133 x 7	133
III		409500	163 x 7	163
IV	2D Axial - symmetric	1600	40 x 4	40
V		3600	60 x 7	60
VI		6400	80 x 9	80

Table 3.1: Mesh parameters. NCV the total number of control volumes in the domain inside the tank.

In summary, Meshes II and V have been selected for the 3D and 2D simulations, respectively. Because the computational time factors were reduced twice respect the finest meshes and within acceptable results. Details of the tested 3D mesh II is shown in Fig. 3.5.

For the temporal discretization of the momentum equation, on the one hand, in the multidimensional (3D or 2D) subroutine, a two-step linear explicit scheme on a fractional-step method has been used, while for the pressure-gradient term an explicit first-order scheme has been employed [34]. This methodology has been previously used with accurate results for solving the flow over bluff-bodies with massive separation (see for instance [35] and [36]), but also for the turbulent natural convection in enclosures [37]. On the other hand, different temporal discretization are used for the fluid inside the tube with each case. The time step has been selected according to the fluid needs.

3.3 Experimental validation

Four experiments have been used for the validation of the models proposed. Different combinations of single-phase/two-phase (evaporation) flow of the fluid (LN_2/ N_2) inside the tube together with different combinations of single-phase (liquid water) / two-phase (water-ice, in process of freezing or melting) of the fluid inside the tank have been tested by DLR [3], see Table 3.2. The LTA (see Fig. 3.6) consists on a cylindrical container of PTFE that was filled partially with the PCM, the 80% of the total volume approximately (indicated as fluid 1, which is water, the fluid 2 is air). The vertical tube is made of stainless steel and it is located inside of the container in the centre. There is a part of the tube located upstream and another part located downstream. The nitrogen flow is injected from the bottom of the tube under different conditions. The (LN_2) was selected as the test fluid for the safety considerations.

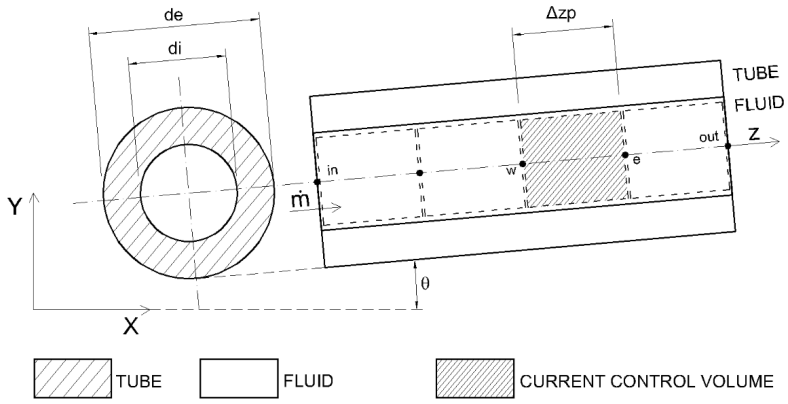

(a)

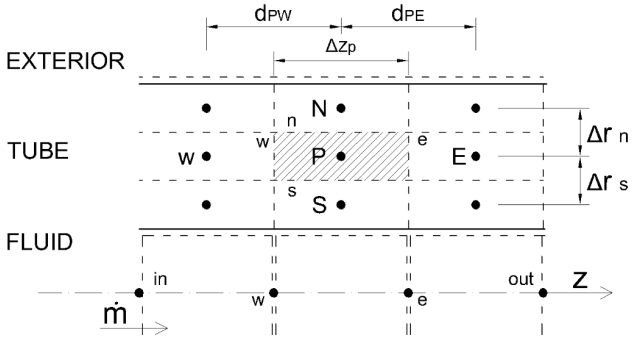

(b)

Figure 3.4: (a) Fluid flow discretization; (b) tube discretization.

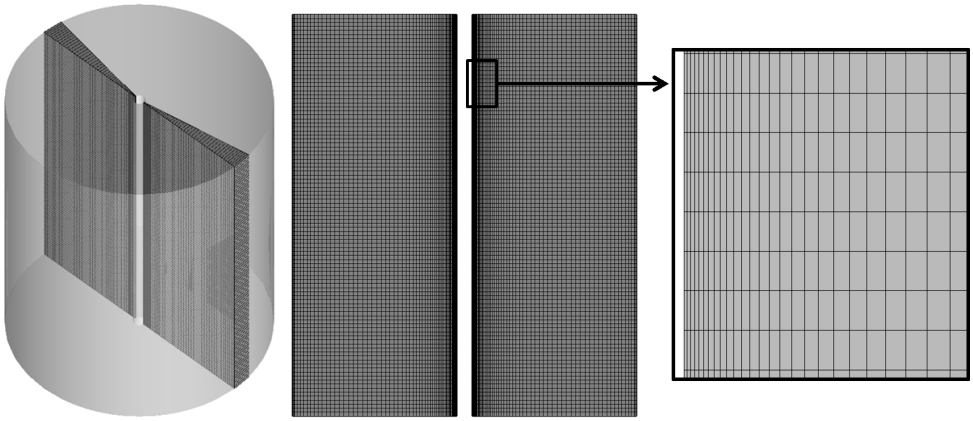

Figure 3.5: Views of the 3D mesh II.

Case	Fluid inside tube	Fluid in the tank
A	Single flow, gas	Single flow, liquid
B	Single flow, gas	Two-phase flow, melting
C and D	Two-phase flow, liquid evaporation	Two-phase flow, freezing

Table 3.2: Short description of each case used for validation.

The LTA has 260 mm of internal length (L) with an internal diameter (2*r0) of 178 mm and a wall thickness of 10 mm. The inlet tube has around 550 mm length with an internal diameter of 5 mm and a thickness of 1.5 mm. The length of the outlet tube has around 200 mm with the same internal diameter and wall thickness to the inlet tube.

In order to reproduce realistic conditions, it has been estimated the exterior heat transfer coefficient between the inlet and outlet tubes and the external environment, by means of empirical correlations of natural convection of cylinders in vertical position. The heat transfer coefficients (U) of the tank have been calculated taking into account experimental measurements and with different values according to the appropriate side of the LTA (top, bottom and lateral).

For all cases, a variable thermophysical properties were considered for the fluid (LN_2/N_2) inside the tube. However, for the fluid (water-ice) inside the tank have been considered constant or variable depending of the case, as can be seen in Table 3.3.

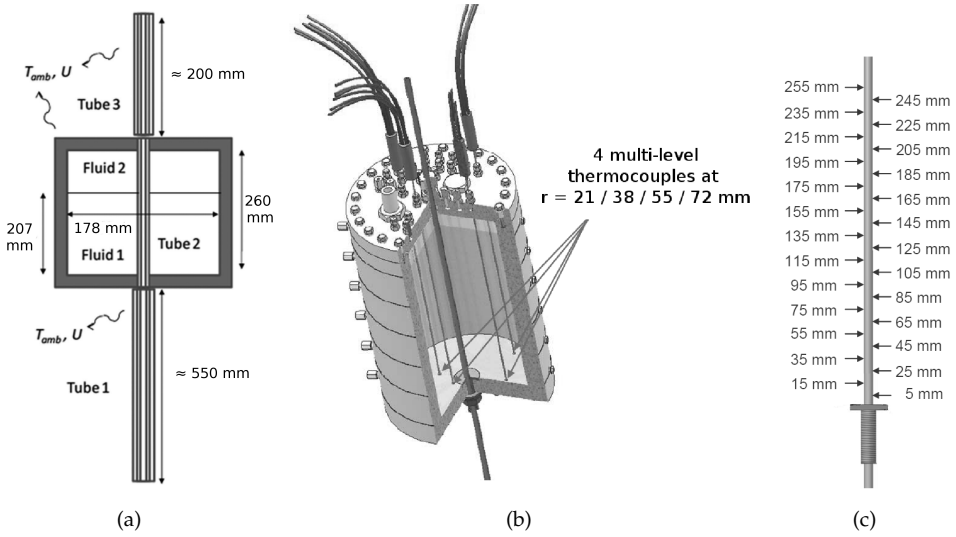

Figure 3.6: (a) Schematic view of the system simulated; (b) thermocouples located inside the accumulator at different radii and height; (c) thermocouples located in the external wall of the tube at different height. (Figures b) and c) extracted from [3, 4].

	Case	A	B	C	D
T_{ow}	$(°C)$	7.74	-2.00	1.12	3.2
$T_{amb(b/s/t)}$	$(°C)$	12.50	-2.19/-2.19/0.35	1.52	1.0
U	(W/m^2K)	5 - 12	2 - 10	2 - 10	2 - 10
$\dot{m}(N_2)$	(g/s)	4.15	7.82	30.0	0.7
$T_{in}(N_2)$	$(°C)$	80.0	80.0	-195.0	-195.0
ρ_{N2}	(kg/m^3)	variable [38]	variable [38]	variable [38]	variable [38]
C_{pN2}	(J/kgK)	variable [38]	variable [38]	variable [38]	variable [38]
λ_{N2}	(W/mK)	variable [38]	variable [38]	variable [38]	variable [38]
ρ_w	(kg/m^3)	variable [38]	997.0	997.0	997.0
μ_w	$(Pa.s)$	variable [38]	0.001	0.001	0.001
β_w	(K^{-1})	variable [38]	variable [38]	$-2.07 \cdot 10^{-4}$	$-2.07 \cdot 10^{-4}$
C_{pw}	(J/kgK)	variable [38]	4184.0	4184.0	4184.0
λ_w	(W/mK)	variable [38]	0.607	0.607	0.607
ρ_{ice}	(kg/m^3)	-	916.0	916.0	916.0
C_{pice}	(J/kgK)	-	1930.0	variable [39]	variable [39]
λ_{ice}	(W/mK)	-	2.22	variable [39]	variable [39]
ρ_{air}	(kg/m^3)	variable [38]	variable [38]	-	-
C_{pair}	(J/kgK)	variable [38]	variable [38]	-	-
λ_{air}	(W/mK)	variable [38]	variable [38]	-	-

Table 3.3: Input conditions of the tests.

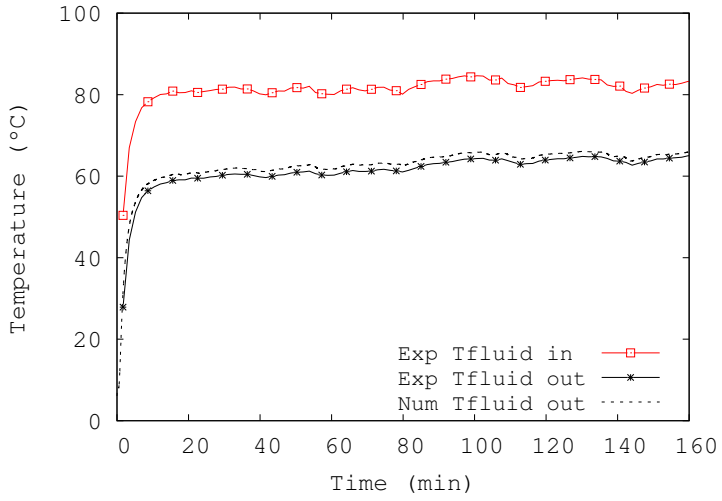

(a)

Figure 3.7: Case A: comparison of the experimental data vs. numerical results of the transient evolution of the nitrogen gas outlet temperature.

3.3.1 Results of case A

The LTA is filled with water that is heated by hot nitrogen gas. In this case a 3D simulation for the water inside the tank has been performed using the mesh II. The heat losses to the environment have been adjusted in the simulation to the experimental values, with an overall heat transfer coefficient of U = 5 - 14 W/m^2K ($U_{top} \approx 5$ W/m^2K, $U_{lateral,air} \approx 8$ W/m^2K, $U_{lateral,pcm} \approx 14$ W/m^2K and $U_{bottom} \approx 10$ W/m^2K). The air chamber temperature has been considered by means of an overall energy balance.

The evolution of the outlet temperature of the in-tube nitrogen gas is shown in Fig. 3.7. In general, a good agreement can be appreciated between experimental data and numerical results. The numerical results follow the transient evolution of the temperature correctly, although with small differences between them. The main reason could be not the consideration of the boundary conditions of the LTA with enough accuracy. The result for the final instant shows that the compared test remain within an relative error below 2.6% (err = 100 abs((T$_{outletExp}$-T$_{outletNum}$)/T$_{outletExp}$)[%]).

The Figs. 3.8 and 3.9 show more details by comparing experimental vs. numerical

of the transient evolution of the temperature over time at different locations inside the water tank. The greater effect of the height on the temperature can be clearly seen, while a smaller effect can be observed in the radial direction. The predicted temperatures inside the water are in a acceptable agreement with the experiment. However, some slight discrepancies can be observed at the end of the simulation, probably also due to inaccuracies in the boundary conditions. The results presented have been improved compared to a previous work [2], due to the improvement in the boundary conditions for the fluid inside the LTA.

Additional and more detailed information is obtained with the multidimensional (3D) numerical results at any time about the temperature distribution and the movement due to the natural convection of the water inside the tank. The Fig. 3.10 shows the transient evolution of the temperature of the water inside the tank. It can be seen how the in-tank water temperature increases progressively from bottom to top of the tank, because the received energy from the in-tube nitrogen gas. Furthermore, there can be also observed how the phenomena of the stratification of the temperatures of the fluid advances from the bottom to the top.

The Fig. 3.11 shows the trajectories of the water in the tank at different instants of time. The water of the tank that is heated near the pipe wall travels up and it moves around the tube forming a stream that advances toward the top of the tank. This stream of heated water interacts continuously with the water in the core. When the stream in the top arrive to the lateral wall of the tank, downward stream is formed as shown in the Fig. 3.11.

3.3.2 Results of case B

In this test, the LTA is filled with water, then it is cooled until the water reaches the solid state (ice). When the experiment is started the water into the tank is heated by hot N_2 gas. The LTA has been simulated with a 3D model in the tank using the mesh II. The numerical heat losses have been adjusted to the experimental data, with an overall heat transfer coefficient of U = 4 - 9 W/m^2K, depending on the side ($U_{top} \approx 4$ W/m^2K, $U_{lateral,air,pcm} \approx 8$ W/m^2K, and $U_{bottom} \approx 9$ W/m^2K). The air chamber has been considered by means of an overall energy balance.

The Fig. 3.12 shows the comparison between the calculated temperatures and the experimental ones, for the outlet temperature of the in-tube nitrogen gas and the wall tube temperature. The numerical results show an acceptable agreement with the experimental data during this test. The Fig. 3.12 (a) shows how the numerical results follow the transient evolution of the outlet temperature of the in-tube nitrogen gas. The Fig. 3.12 (b) also shows that the measured values of the temperature of the wall tube are modelled quite accurately. However, few differences can be found in the temperature of the wall tube in the sensor at height 245 mm, see Fig. 3.12 (b). These

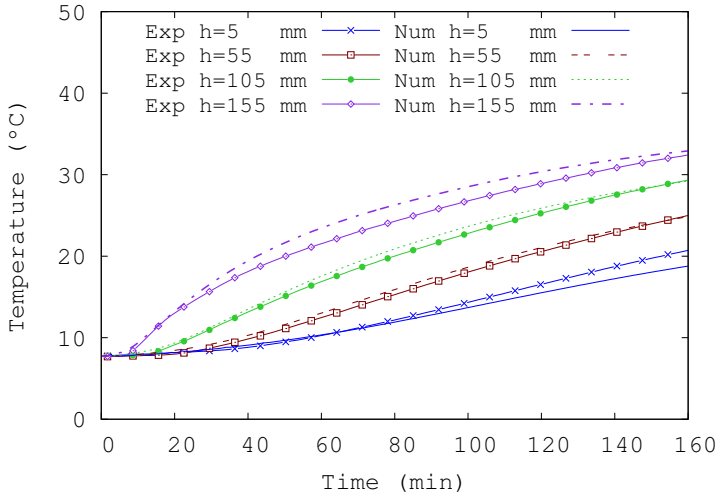

(a)

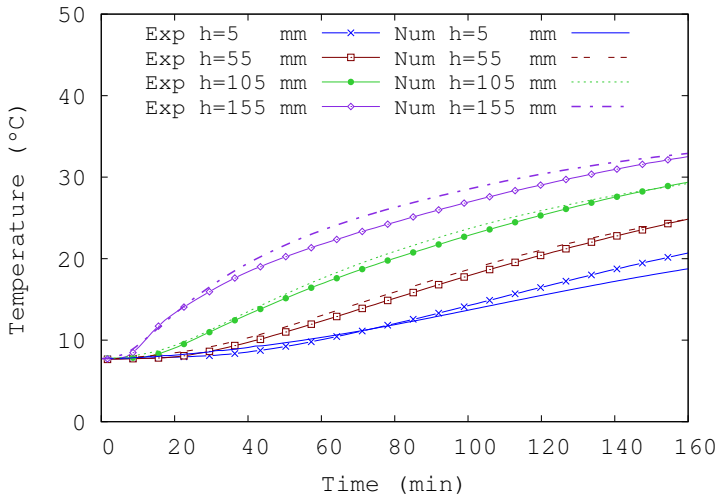

(b)

Figure 3.8: Case A: comparison of the experimental data vs. numerical results of the transient evolution of temperature of the in-tank water at different positions: (a) r= 21 mm; (b) r= 38 mm.

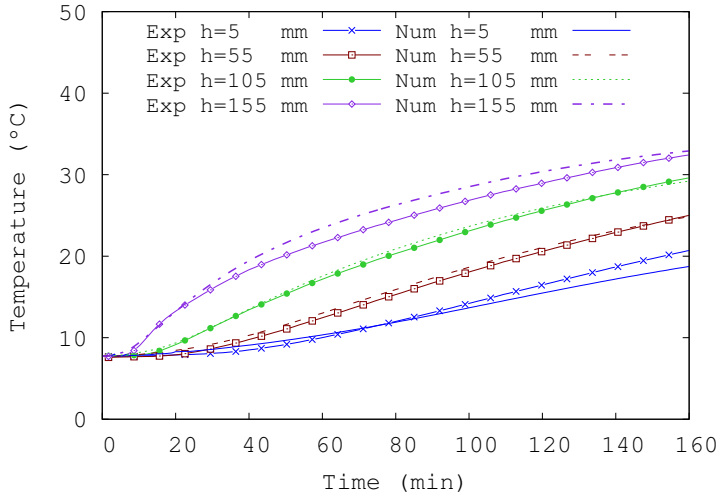

(a)

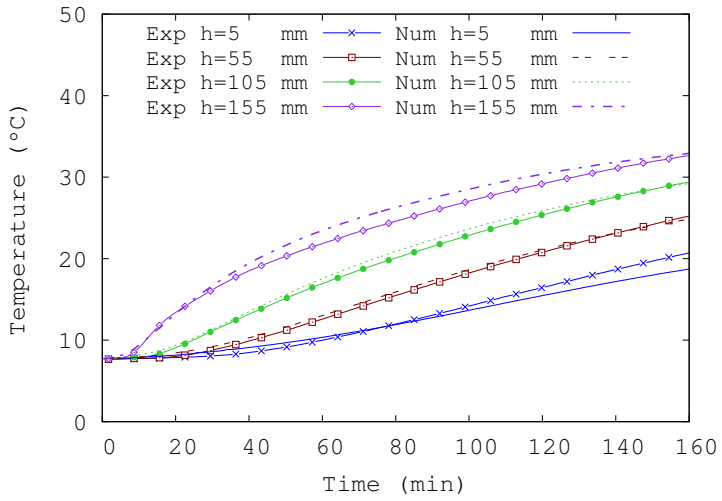

(b)

Figure 3.9: Case A: comparison of the experimental data vs. numerical results of the transient evolution of temperature of the in-tank water at different positions: (a) r= 55 mm; (b) r= 72 mm.

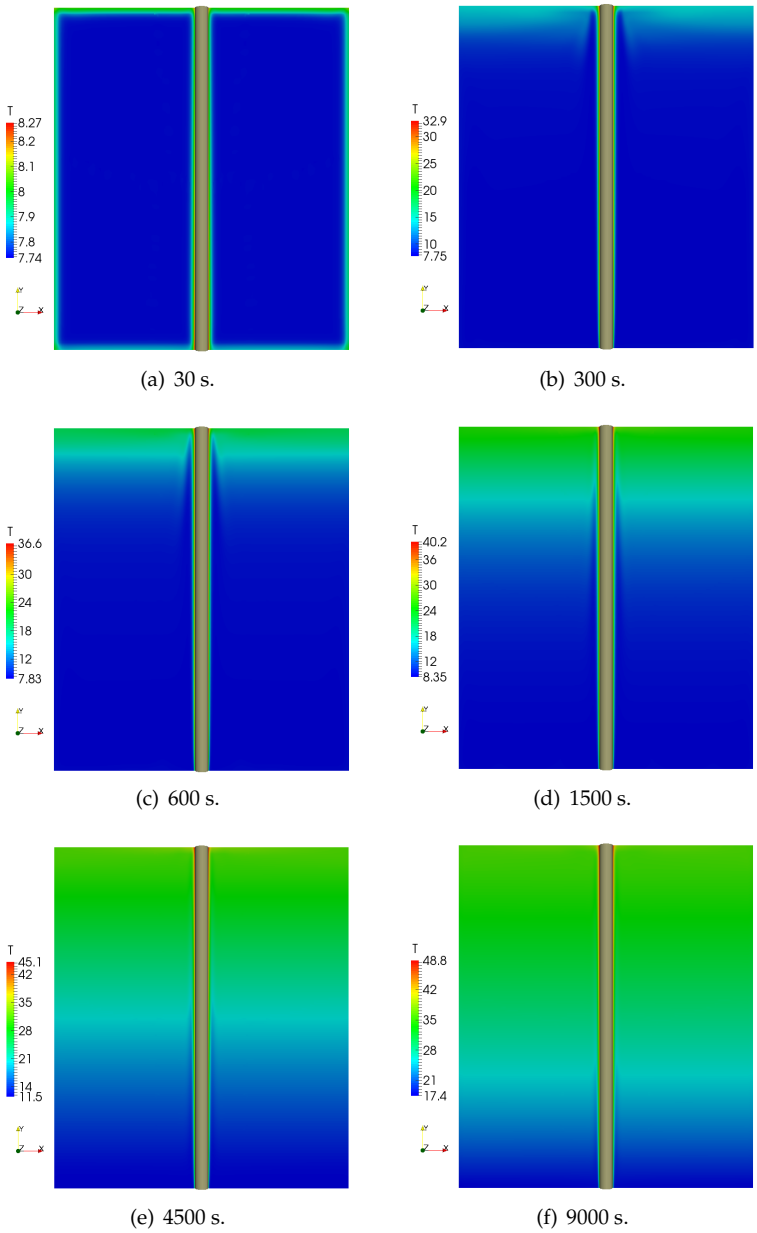

(a) 30 s. (b) 300 s.

(c) 600 s. (d) 1500 s.

(e) 4500 s. (f) 9000 s.

Figure 3.10: Case A: in-tank water temperature for different time instants (s).

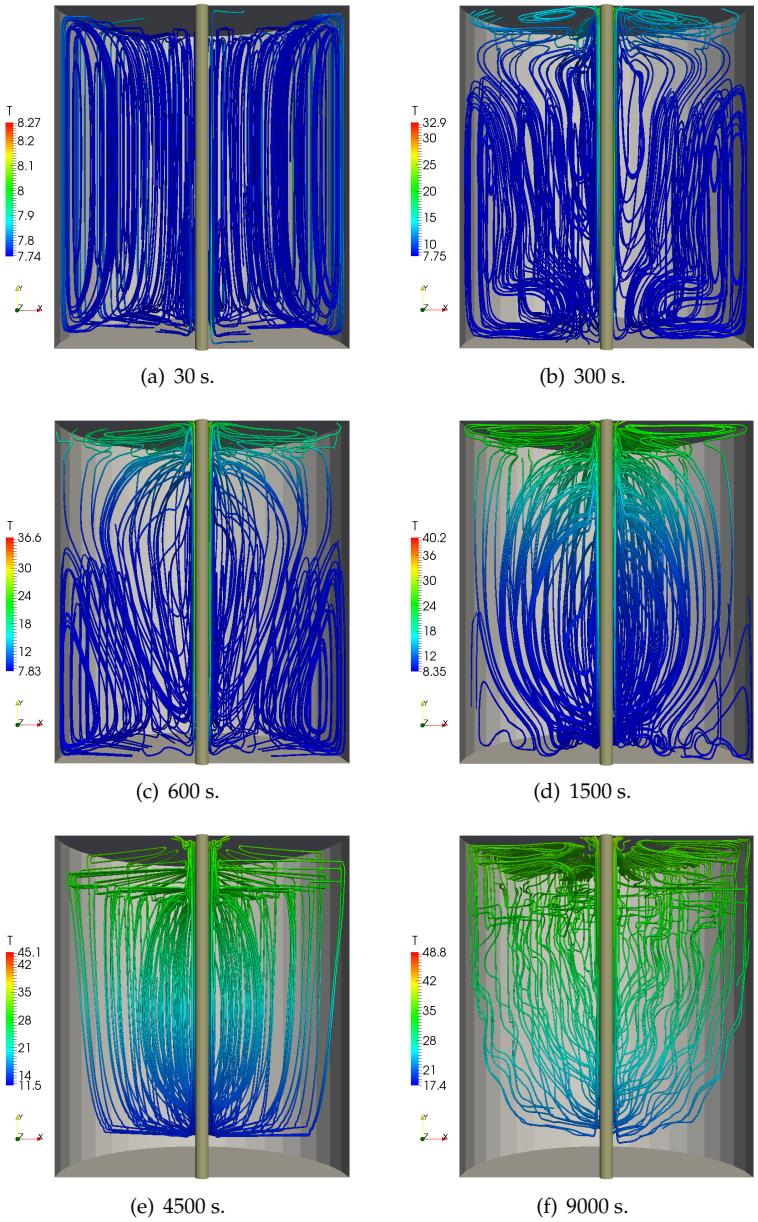

(a) 30 s. (b) 300 s.

(c) 600 s. (d) 1500 s.

(e) 4500 s. (f) 9000 s.

Figure 3.11: Case A: in-tank water trajectories for different time instants (s).

discrepancies are due probably to the use of empirical information [31] in the model for the air gap region.

The Figs. 3.13 and 3.14 show the transient evolution of the temperature vs. time at different locations inside the water tank. In this figure, the big influence of the height on the temperature can be observed. In this case, the differences on temperature in the radial direction is due to the phase change is occurring, the solid water (ice) is changing to liquid water. The Figs. 3.13 and 3.14 also show, that the numerical results followed a trend similar to the experimental data. In the lower part of the tank the measured values are modelled quite accurately. However, the measured values in the upper sensor (h= 155 mm) show distinctly a higher deviation between experiment and simulation. Also, it can be observed by the end of the simulation that the numerical results have a delay with the experiment data. Different reasons could be causing the differences:

- The ice break-up, caused by the high difference of temperature (around 80 $^{\circ}C$) between the in-tank water (ice) and the in-tube nitrogen gas [40].
- The hypotheses of constant density assumed, while the liquid water presents a variation of the density of around 8% higher respect to density at solid state.
- Other thermophysical properties of water have also been considered as constant (density, thermal conductivity, viscosity, heat capacity).

The Fig. 3.15 show different sections of the 3D temperature field, it can be observed the transient evolution of the temperature of the water inside the tank for different instants of time . It is seen how the ice inside the tank is melting and the temperature of the liquid water increases progressively, due to the received energy from the in-tube nitrogen gas.

The Fig. 3.16 shows the trajectories of the liquid water and the liquid fraction in the tank at different times. Near the pipe wall, the ice is heated and it melts, then the liquid water begins to travel in up direction, and moving around the tube forming a stream that advances toward the top of the tank. The heated water interacts continuously with the solid water in the core, producing the ice melt.

3.3.3 Results of case C

In this case, the LTA is filled with water that is cooled down by LN_2. The heat transfer losses have been adjusted in the simulation to the experimental values by means an overall heat transfer coefficient of U= 2-4 W/m^2K, depending on the side ($U_{top} \approx 4$ W/m^2K, $U_{lateral,pcm} \approx 2.5$ W/m^2K and $U_{bottom} \approx 2$ W/m^2K). In the cylindrical tank, it has not considered the influence of the air chamber. By the one

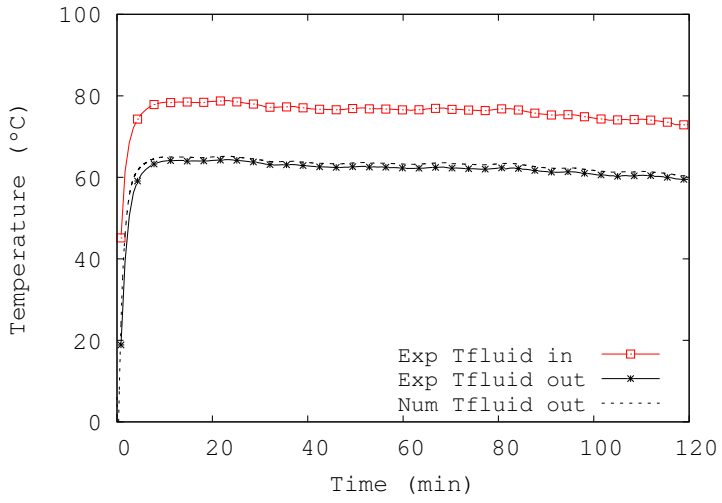

(a)

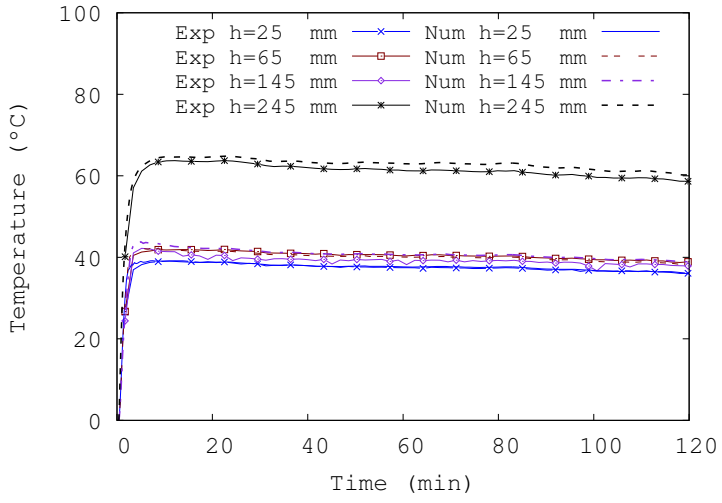

(b)

Figure 3.12: Case B: comparison of the experimental data vs. numerical results of the transient evolution of: (a) the nitrogen gas temperature; (b) tube wall temperature.

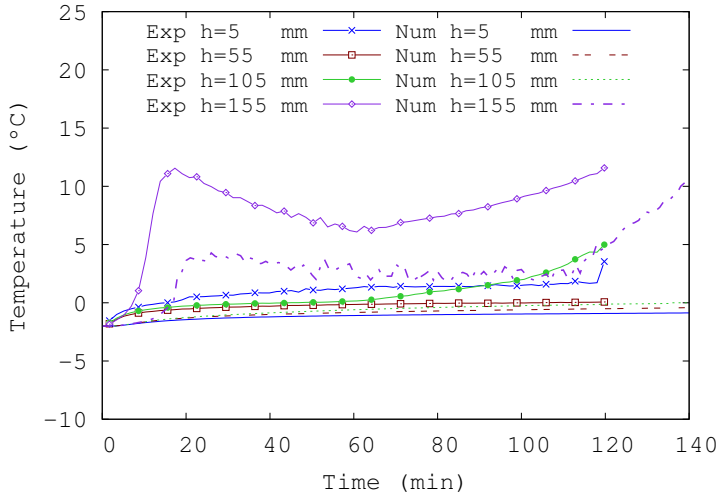

(a)

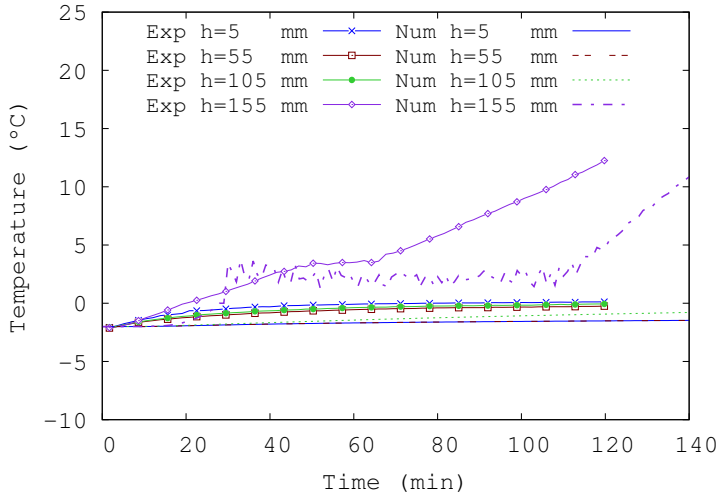

(b)

Figure 3.13: Case B: comparison of the experimental data vs. numerical results of the transient evolution of temperature of the in-tank water at different positions: (a) r= 21 mm; (b) r= 38 mm.

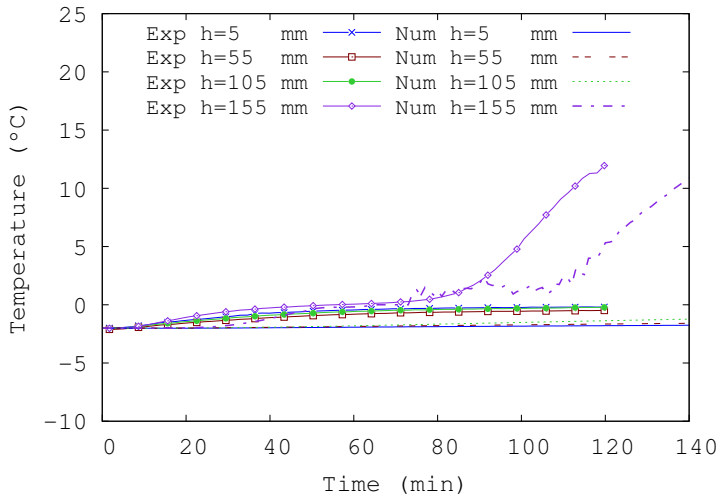

(a)

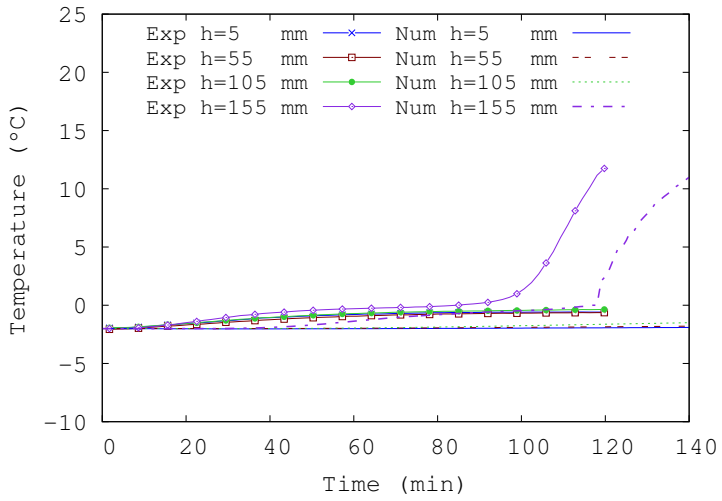

(b)

Figure 3.14: Case B: comparison of the experimental data vs. numerical results of the transient evolution of temperature of the in-tank water at different positions: (a) r= 55 mm; (b) r= 72 mm.

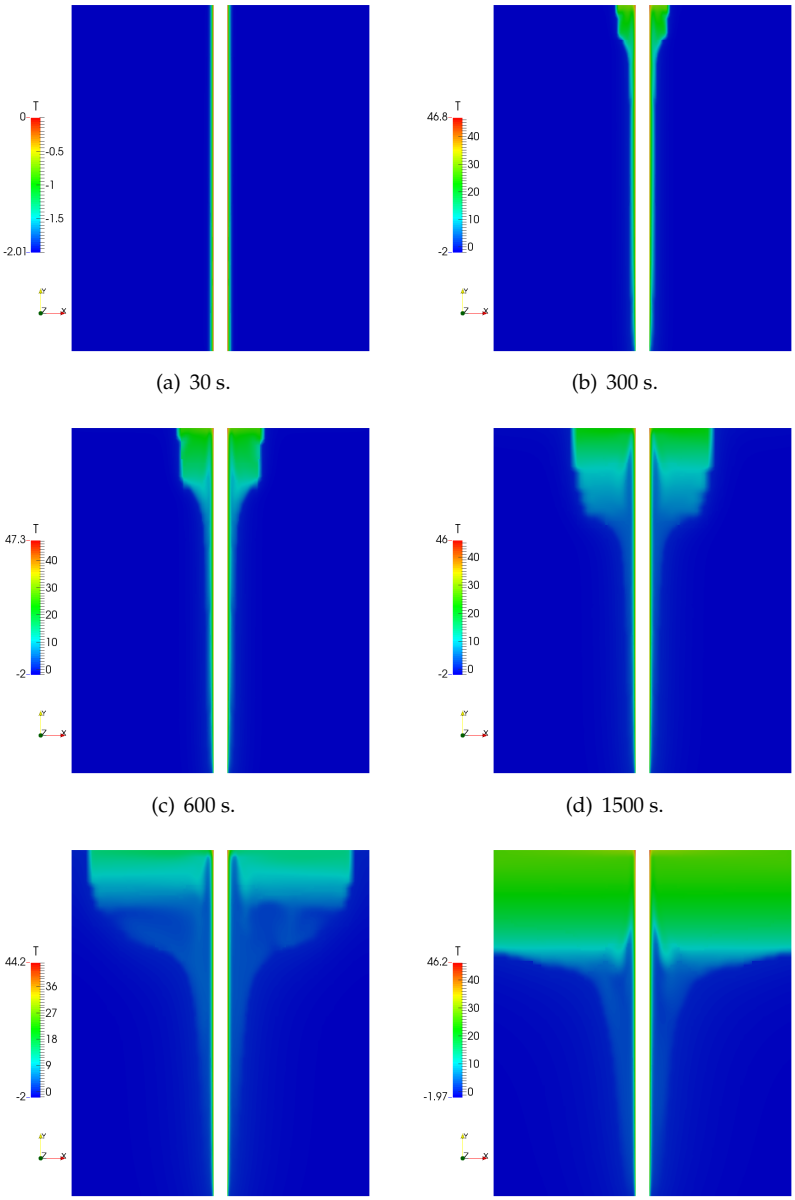

(a) 30 s. (b) 300 s.

(c) 600 s. (d) 1500 s.

(e) 4500 s. (f) 9000 s.

Figure 3.15: Case B: in-tank water temperature for different time instants (s).

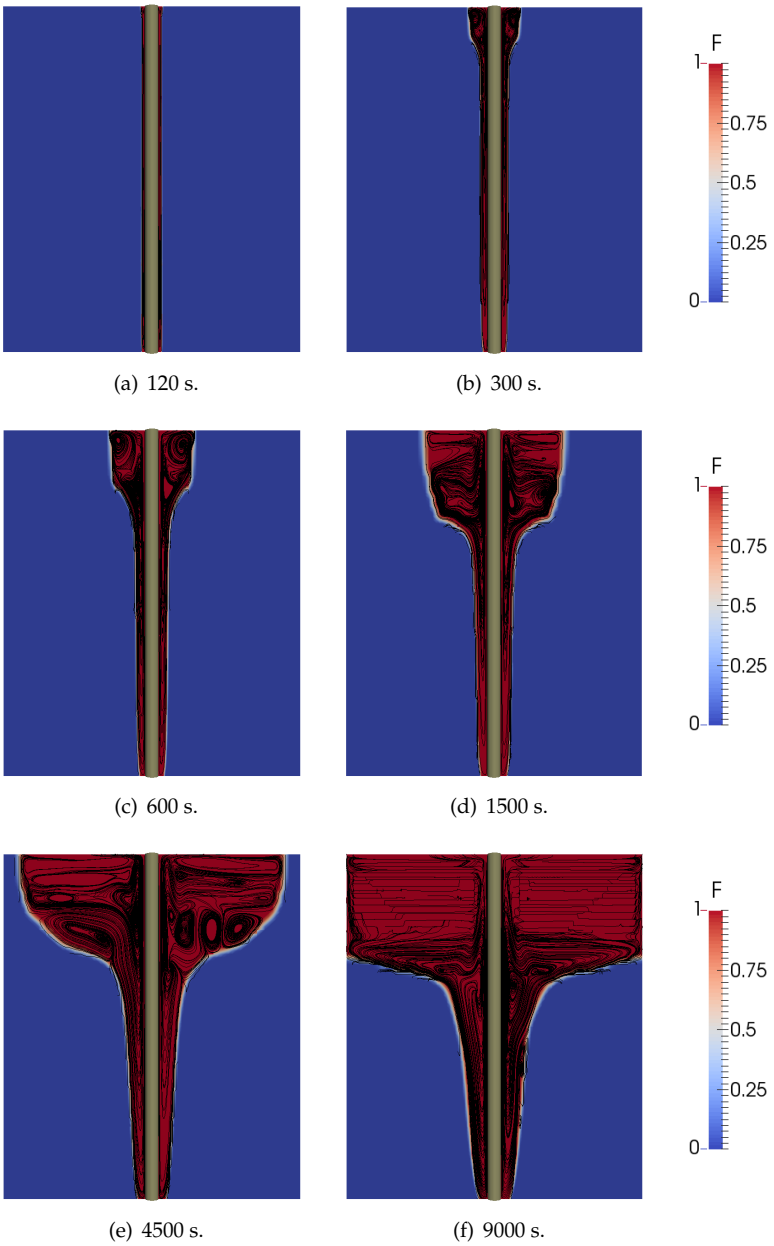

(a) 120 s. (b) 300 s.

(c) 600 s. (d) 1500 s.

(e) 4500 s. (f) 9000 s.

Figure 3.16: Case B: in-tank water trajectories and liquid fraction map for different time instants (s).

hand, for the ice the 2D mesh has been used (mesh V). On the other hand, the mesh for the tube is constant and coincident with the 2D mesh as indicated in section 3.2.5.

The Fig. 3.17 shows the comparison between the calculated outlet temperatures of the N_2 and the experimental ones. A reasonable agreement can be appreciated between experiment and numerical simulation. At the beginning, there are discrepancies between simulation and experiment because the initial sequence of start-up of the experiment that cannot be reproduced accurately: at the beginning of the experiment (first 20 s), all the LN_2 is bypassed from the LTA, then a ball valve is opened during 40 s and after this movement all the LN_2 flow goes through the LTA. In the simulation is supposed the whole mass flow of LN_2 since the beginning. Despite this, the numerical simulations performed seem to reasonably predict the transient behaviour of the in-tube nitrogen flow (liquid and gas). In this case C, special phenomena in the two-phase flow evaporation is detected. In several publications [41–43] it is reported a special type of regime only at high heat transfer ratios. This type of regime is called "quenching" flow. The quenching is encountered when a cold liquid flows on a dry and hot surface and the surface temperature is sufficiently higher than a certain limit. This limit is called rewetting temperature. The Fig. 3.18 shows a comparison on flow patterns between high and low mass flow rate conditions. It shows a fully developed vertical flow pattern typically for a cryogenic liquid, which assumes that the tube is long enough to show the complete flow pattern evolution from beginning to the end [42]. This case is under a high mass flow rate and, two different types of flow pattern can be observed during quenching: inverted annular flow and bubbly flow. At the beginning of this test, when the liquid is injected in the LTA tube, only a stream of gas is in contact with the tube wall (in LTA), as the wall temperature is above the rewetting temperature. The gas heat transfer is not very effective during this type of flow pattern (inverted annular), and the liquid stream cannot get in touch with the tube wall due to its high temperature (evaporation process). The Fig. 3.17 shows the evolution of the outlet temperature of the nitrogen stream. The temperature behaviour is described by zones. The first zone corresponds to the initial evolution of the nitrogen stream reaches a maximum value of temperature when the stream of gas is in contact with the tube wall. In the next zone, as part of the tube wall temperature is getting the rewetting temperature and, a rapid change from the transition flow to the dispersed bubbly flow will occur directly after the quenching front, causing the stream of gas temperature decreases with time. The reason of the transition flow is explained below.

When the wall temperature falls down is the rewetting limit, the liquid comes in contact with the hot surface, wetting again this and therefore, the heat transfer is produced mainly between the liquid and the wall. In this regime the liquid contacts the wall and the heat transfer coefficient is very high. In this work is used a constant rewetting temperature and it has been set at 175 K. The Fig. 3.19 shows the numerical

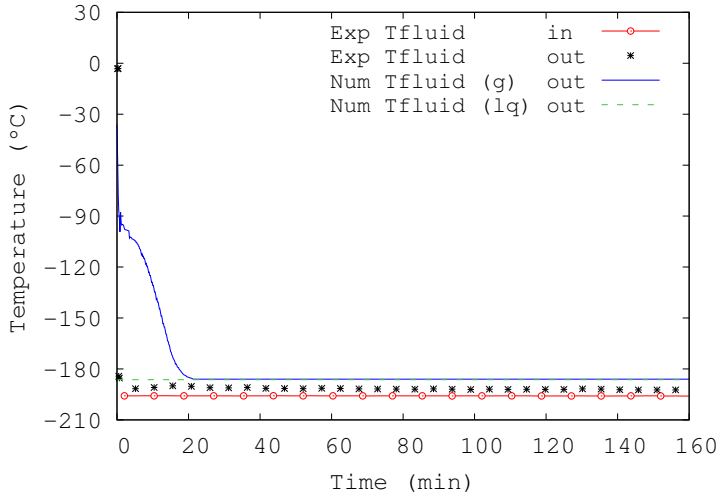

(a)

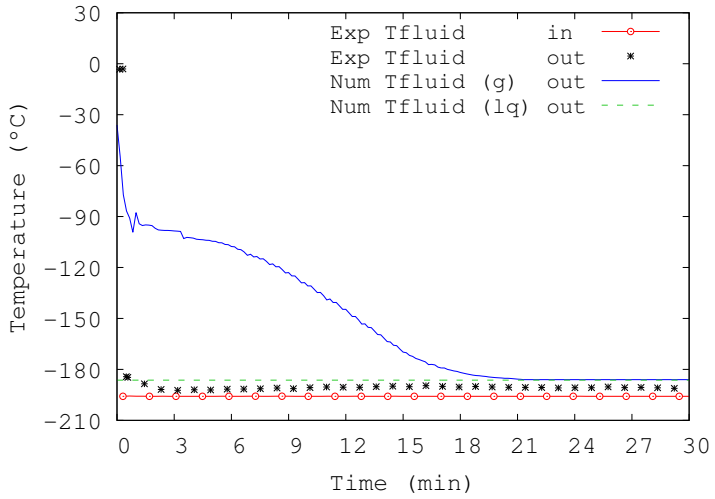

(b)

Figure 3.17: Case C: comparison of the experimental data vs. numerical results of the outlet temperature of the nitrogen stream: (a) during the entire test; (b) during the first thirty minutes of the test.

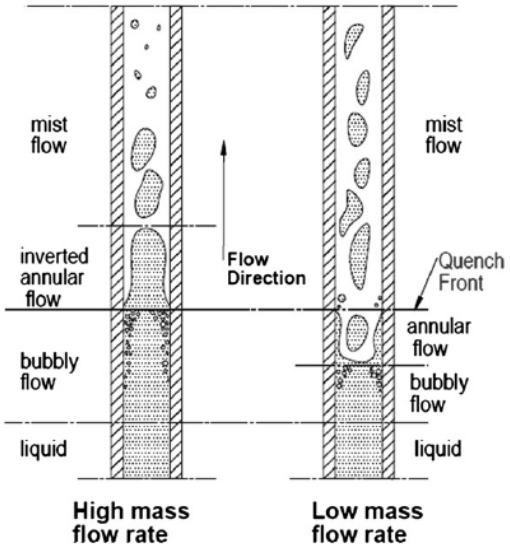

Figure 3.18: Heat transfer regimes and flow patterns during quenching in a vertical pipe. (Figure extracted from [42]).

results of the wall temperature of the tube. It can be observed the temperature jump produced by the sudden change in the heat transfer coefficient, during this period (after the slope change) the flow pattern is bubbly flow. This result agrees reasonably with the experimental data reported by DLR [2, 3].

The Figs. 3.20 and 3.21 show more details by comparing the experimental data vs. numerical results of the transient evolution of the temperature at different locations inside the water tank (ice). The predicted temperatures values inside the water are in an acceptable agreement with the experiment. It can be observed the temperature differences due to the different heights. However, they are more significant the temperature gradients in the radial direction due to the phase change effect (solidification).

3.3.4 Results of case D

In this case, the LTA is filled with water that is cooled down by the LN_2 stream. The heat losses have been adjusted in the simulation to the experimental values with an overall heat transfer coefficient of U= 2-4 W/m^2K, depending on the side ($U_{top} \approx 4$ W/m^2K, $U_{lateral,pcm} \approx 2.5$ W/m^2K and $U_{bottom} \approx 2$ W/m^2K). As in the case C, in the cylindrical tank neither has been considered the air chamber. For this case, also a 2D calculation has been performed for the PCM (water - ice), with the same mesh as case C (mesh V).

The Fig. 3.22 shows the outlet temperature (liquid and gas) and the experimental validation of the tube temperatures. As in the case C, the initial sequence of start-up of the experiment that cannot be reproduced accurately: at the beginning of the experiment (first 50 s), all the LN_2 is bypassed from the LTA, then a ball valve is opened during 100 s and after this movement all the LN_2 flow goes through the LTA. In the simulation is supposed the whole mass flow of LN_2 since the beginning. In this case, there is not temperature jump (as in the case C), this occurs because the flow rate is too low and the flow pattern changes, in this case is a dispersed flow. Again, the model predicts the physics of the situation. This flow pattern was observed in previous works [41–43]. These works described that for low values of mass flow rate the liquid core is irregular, continuously created and disrupted. Consequently, with lower cooling capability, due to most of the liquid cannot touch the tube wall. In Fig. 3.22 a reasonable agreement can be appreciated between experiment and numerical simulation. However, large differences can be found in the temperature of the wall tube in the sensor at height 15 mm.

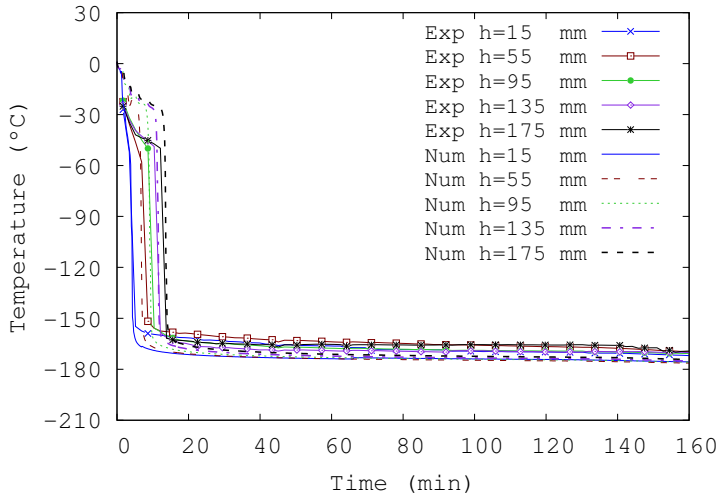

(a)

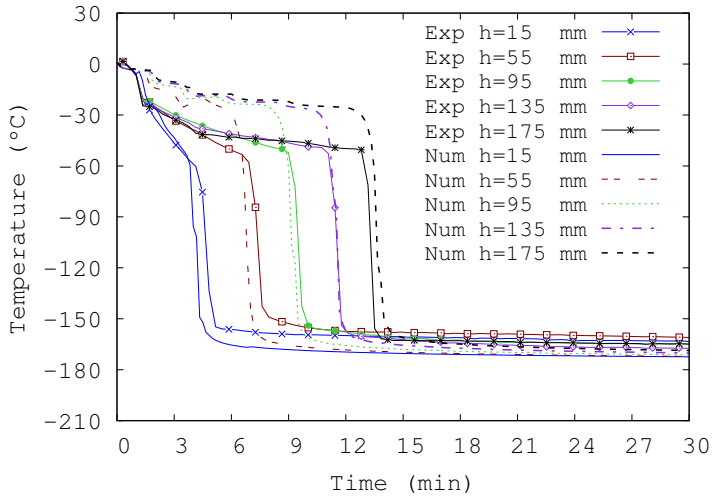

(b)

Figure 3.19: Case C: comparison of the experimental data vs. numerical results of the tube wall temperature: (a) during the entire test; (b) during the first thirty minutes of the test.

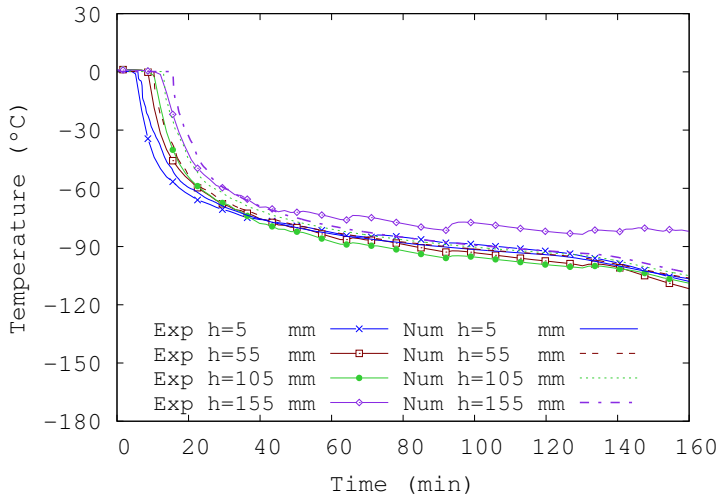

(a)

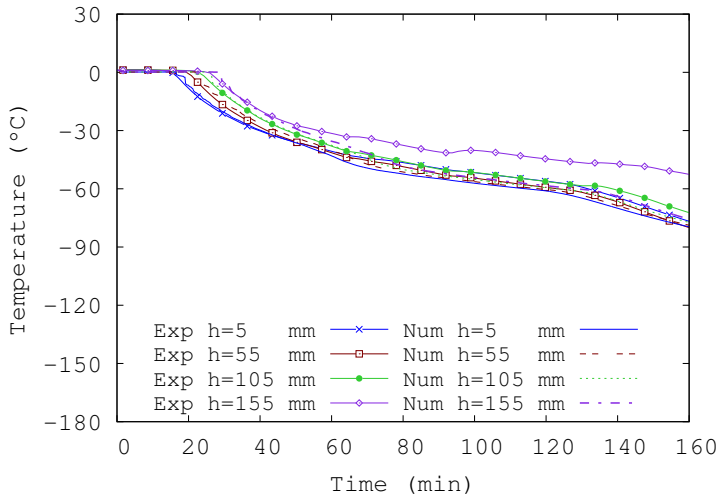

(b)

Figure 3.20: Case C: comparison of the experimental data vs. numerical results of the transient evolution of temperature of the in-tank water at different positions: (a) r= 21 mm; (b) r= 32 mm.

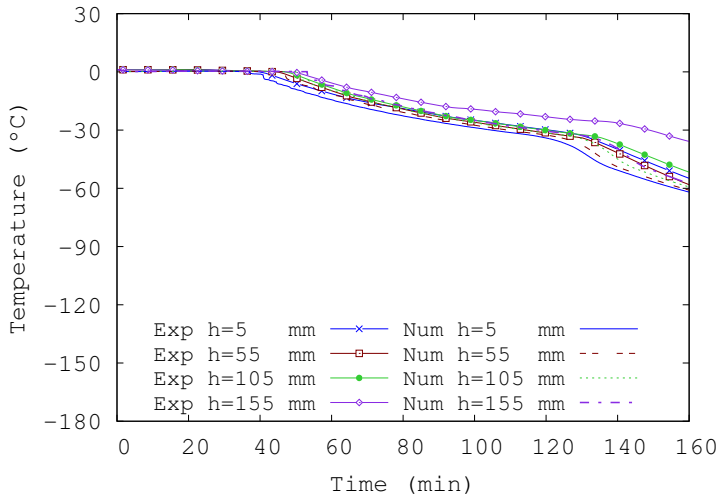

(a)

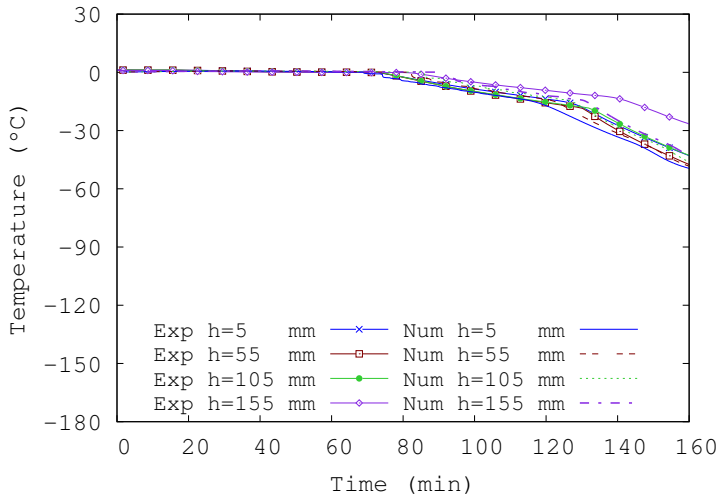

(b)

Figure 3.21: Case C: comparison of the experimental data vs. numerical results of the transient evolution of temperature of the in-tank water at different positions: (a) r= 55 mm; (b) r= 72 mm.

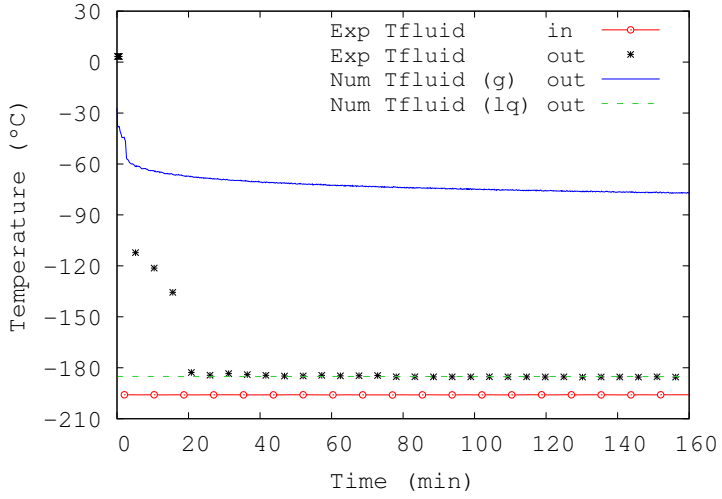

(a)

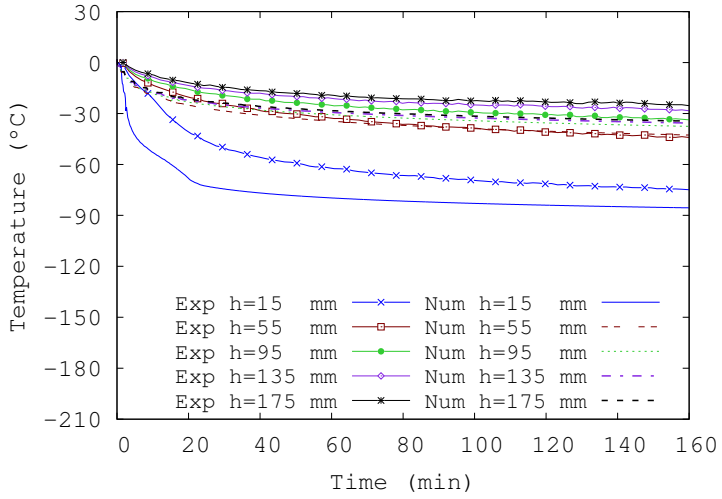

(b)

Figure 3.22: Case D: comparison of the experimental data vs. numerical results of the outlet temperature of: (a) calculated outlet temperature (liquid and gas); (b) tube wall temperature comparison.

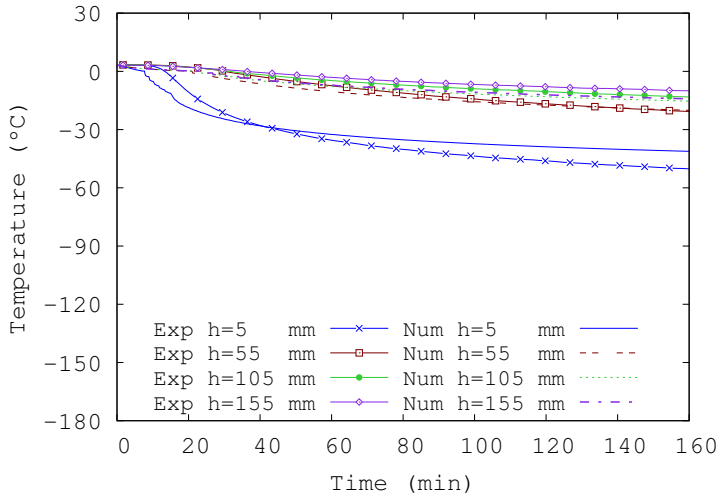

(a)

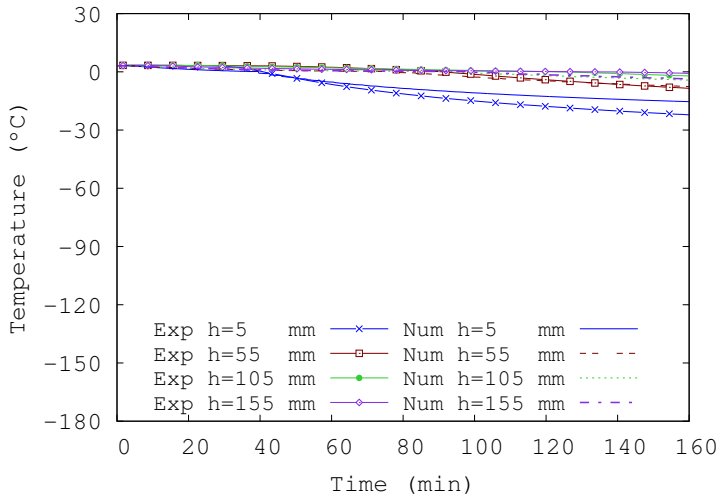

(b)

Figure 3.23: Case D: comparison of the experimental data vs. numerical results of the transient evolution of temperature of the in-tank water at different positions: (a) r= 21 mm; (b) r= 32 mm.

The Fig. 3.23 shows the evolution of the calculated temperatures in the ice. These results are in reasonably agreement with the experiment. As in the case C, it can be observed the temperature differences due to the different heights and the radial direction due to the phase change effect (solidification). In contrast to the case C, in this case, the temperature decreases with time more slower, due to the flow patterns that is present a low mass flow rate, causing lower heat transfer.

3.4 Concluding Remarks

A model for the design and prediction of the thermo-hydraulic behaviour of the LTA prototype of a LTCP system has been developed. This model is composed by three main different subroutines: i) 1D two-fluid model; ii) heat conduction of the solid parts; iii) multidimensional convection with the possibility of using LES models with the ability of introducing PCM material.

Four cases are been used for the validation according to the conditions of the N_2 and the water storage. In the case A (gas flow of N_2, liquid water inside tank) a reasonable agreement is observed between numerical results and experimental data. The few discrepancies observed in the temperatures inside the tank are due to the inaccuracies of the boundary conditions of the LTA.

In the case B (gas flow of N_2, water-ice melting), a reasonable agreement is observed between numerical results and experimental data in the case of N_2 gas outlet temperature. Concerning to the multidimensional simulation of PCM inside the tank, a 3D model with LES modelling has been used. In this case, the assumption of constant physical properties in the water-ice was the cause of discrepancies together with the break up of the ice.

For the case C (vaporization of the LN_2 stream, water-ice freezing), the 1D two-phase flow evaporation subroutine, therefore predicted quite well the heat transfer phenomena at high heat fluxes, the temperature profiles at the tube wall are quite well reproduced. Both for cases C and D (vaporization of the LN_2 stream, water-ice freezing) the outlet temperature calculated of the N_2 stream has a reasonable agreement with the experiment. Regarding the prediction of the temperatures in the ice inside the tank, although the tendencies are quite well predicted.

From the experiments and the numerical simulation have been confirmed that mass flow rate has a significant influence on the flow patterns for cryogenic temperatures.

According to this exhaustive experimental validation, it has been demonstrated the capabilities of the model developed, that is valid for design optimization and prediction purposes of such type of devices.

Nomenclature

c_p	specific heat capacity
d	diameter
g	gravity
H	height
h	enthalpy
$\hat{j}$	unitary vector in the vertical direction
p	pressure
$\dot{q}$	heat flux
r	radial direction, radius
s	surface area
S	momentum source term coefficient introduced by the porosity method
T	temperature
t	time
$u, \vec{u}$	velocity magnitude, vector (PCM)
v	velocity (two-phase flow)
z	axial coordinate

Greek symbols

α	heat transfer coefficient
β	thermal expansion coefficient
ϵ	volume liquid fraction (porosity)
ε	void fraction
θ	angle to gravity
Γ	mass exchange
λ	thermal conductivity
μ	dynamic viscosity
ν	kinematic viscosity
ρ	density
τ	shear stress

Subscripts

air	air
amb	ambient
$bottom$	referred to the bottom side of the tank
Exp	referred to the experiment
g	gas
H_2O	water

$inlet$	inlet
l	liquid
Num	referred to the numerical simulation
$N2$	nitrogen
$lateral$	referred to the lateral side of the tank
$outlet$	outlet
pcm	referred to PCM
qr	related to q and r invariants
top	referred to the top side of the tank
$tube$	referred to the tube
vms	variational multiscale
$wall$	referred to wall

References

[1] M. Muszynski, P. Alliot. The in-space propulsion (ISP-1) project. In *Proceedings of the 61st International Aeronautical Congress*, 2010.

[2] S. Torras, J. Castro, J. Rigola, S. Morales, J. Riccius, J. Leiner. Modelling and experimental validation of the heat accumulator in a low thrust cryogenic propulsion (LTCP) system. In *Proceedings of the 5th European Conference For Aerospace Sciences (EUCASS)*, 2013.

[3] J. Leiner, J. Riccius. Experimental investigation of phase-change behavior in a water-ice heat accumulator setup for cryogenic application. In *Proceedings of the Space Propulsion Conference*, 2012.

[4] J. Leiner, J. Riccius, O. Haidn, D. Vuillamy. Heat accumulators for cryogenic in-space propulsion. In *Proceedings of the 4th European Conference For Aerospace Sciences (EUCASS)*, 2011.

[5] R.G. Jahn. Physics of electric propulsion, New York: McGraw Hill (1968).

[6] R.J. Cassady, R. Frisbee, J. Gilland, M. Houts, M. LaPinte, C. Maresse-Reading, S. Oleson, J. Polk, D. Russell, A. Sengupta. Recent advances in nuclear powered electric propulsion for space exploration. *Energy Conversion & Management*, 49:412–435, 2008.

[7] T.O. Dobbins. Thermodynamics of rocket propulsion and theoretical evaluation of some prototype propellant combinations. Wright Air Development Center, TR-59-757, 1959.

[8] R. Frisbee, H. Robert. Advanced space propulsion for the 21st Century. *Journal of Propulsion and Power*, 19:1129–1154, 2003.

[9] ESA 12th edition of the European Space Technology Master Plan, 2015. European Space Agency, 2015.

[10] NASA Technology roadmaps, TA 2: In-space propulsion technologies, 2015. National Aeronautics and Space Administration (NASA), 2015.

[11] P. Caisso, A. Souchier, C. Rothmund, P. Alliot, C. Bonhomme, W. Zinner, R. Parsley, T. Neill, S. Forde, R. Starke, W. Wang, M. Takahashi, M. Atsumi, D. Valentian. A liquid propulsion panorama. *Acta Astronautica*, 65:1723-–1737, 2009.

[12] C.H. DeLee, P. Barfknecht, S. Breon, R. Boyle, M. DiPirro, J. Francis, J. Huynh, X. Li, J. McGuire, S. Mustafi, J. Tuttle, D. Wegel. Techniques for on-orbit cryogenic serving. *Cryogenics*, 64:289–294, 2014.

[13] J.R. Schuster, J.P. Wachter, A.G. Powers. COLD-SAT, an orbital cryogenic hydrogen technology experiment. *40th Congress of the International Astronautical Federation*, 1989.

[14] E. Kramer. Cryogenic on-orbit liquid depot-storage, acquisition and transfer (COLD-SAT) experiment conceptual design and feasibility study. NASA Technical paper 3523, 1998.

[15] J. Krige, A. Russo. A history of the European Space Agency 1958 – 1987, Volume II. European Space Agency, 2000.

[16] P. Alliot, P. James, C. Fiorentino, J. Follet, D. Valentian, J.M. Conrardy, D. Vuillamy, H. Goislot, P. Garceau, R. Bec. Progress of the VINCI engine system engineering. In *45nd AIAA/ASME/SAE/ASEE Joint Propulsion Conference & Exhibit*, 2009.

[17] V.P. Dawson, M.D. Bowles. Taming liquid hydrogen: the Centaur upper stage rocket 1958 - 2002, the NASA history series. National Aeronautics and Space Administration (NASA), NASA SP-2004-4230.

[18] D. Cecere, E. Giacomazzi, A. Ingenito. A review on hydrogen industrial aerospace applications. *International Journal of Hydrogen Energy*, 39:10731–10747, 2014.

[19] D. Valentian, J.M. Conrardy, D. Vuillamy, H. Goislot, P. Garceau, R. Bec. Low cost cryogenic propulsion module with fuel cell power supply. In *42nd AIAA/ASME/SAE/ASEE Joint Propulsion Conference & Exhibit*, 2006.

[20] SNECMA. Cryotechnic propulsion medule. European Patent EP 1241341B1, May 31, 2006.

[21] M. Ishii, T. Hibiki. Thermo-fluid dynamics of two-phase flows, Springer, 2006.

[22] K. Yuan, Y. Ji, J.N. Chung. Numerical modeling of cryogenic chilldown process in terrestrial gravity and microgravity. *International Journal of Heat and Fluid Flow*, 30:44–53, 2009.

[23] V. Gnielinski. New equations for heat and mass transfer in turbulent pipe and channel flow. *International Chemical Engineering*, 16:359–368, 1976.

[24] S. Morales-Ruiz, J. Rigola, C.D Pérez-Segarra, O. García-Valladares. Numerical analysis of two-phase flow in condensers and evaporators with special emphasis on single-phase/two-phase transition zones. *Applied Thermal Engineering*, 29:1032–1042, 2009.

[25] S. Morales-Ruiz, J. Castro, J. Rigola, C.D Pérez-Segarra, O. Oliva. Numerical resolution of the heat accumulator in a low cost cryogenic propulsion (LCCP) system. In *Proceedings of the 4th European Conference For Aerospace Sciences (EUCASS)*, 2011.

[26] P.A. Galione, O. Lehmkuhl, J. Rigola, A. Oliva. Fixed-grid modeling of solid-liquid phase change in unstructured meshes using explicit time schemes. *Numerical Heat Transfer*, 65:27–52, 2014.

[27] V. Voller, C. Prakash. A fixed grid numerical modelling methodology for convection-diffusion mushy region phase change problems. *Int. J. Heat Mass Transfer*, 30:1709–1719, 1987.

[28] A.D. Brent, V.R. Voller. Enthalpy-porosity technique for modelling convection-diffusion phase change: application to the melting of a pure metall. *Numerical Heat Transfer*, 13, 1988.

[29] D.A. Nield, A. Bejan. Convection in Porous Media, 3rd edition. Springer, 2006.

[30] S.V. Patankar. Numerical Heat Transfer and Fluid Flow, Hemisphere, Washington, DC, 1980.

[31] H.Y. Wong. Handbook of essential formulae and data on heat transfer for engineers, Longmann, London, New York (1977) ISBN: 0-582-46050-6.

[32] R. Damle, O. Lehmkuhl, G. Colomer, I. Rodríguez. Energy simulation of buildings with a modular object-oriented tool. In *Proceedings of the ISES World Conference*, 2011.

[33] O. Lehmkuhl, C.D. Pérez-Segarra, R. Borrell, M. Soria, A. Oliva. TERMOFLUIDS: A new Parallel unstructured CFD code for the simulation of turbulent industrial problems on low cost PC Cluster. In *Proceedings of the Parallel CFD 2007 Conference*, 2007.

[34] F.X. Trias, O. Lehmkuhl. A self-adaptive strategy for the time integration of Navier-Stokes equations. *Numerical Heat Transfer*, 60:116–134, 2011.

[35] I. Rodríguez, R. Borrell, O. Lehmkuhl, C.D. Pérez-Segarra, A. Oliva. Direct numerical simulation of the flow over a sphere at Re = 3700. *Journal of Fluid Mechanics*, 679:263–287, 2011.

[36] I. Rodríguez, O. Lehmkuhl, R. Borrell, C.D. Pérez-Segarra, A. Oliva. Low-frequency variations in the wake of a circular cylinder at Re = 3900. In *Proceedings of the 13th European Turbulence Conference*, 2011.

[37] D. Kizildag, I. Rodríguez, A. Oliva, O. Lehmkuhl. Limits of the Oberbeck-Boussinesq approximation in a tall differentially heated cavity filled with water. *International Journal of Heat and Mass Transfer*, 68:489–499, 2014.

[38] NIST, Thermodynamic properties of refrigerants and refrigerant mixtures database (REFPROP), Version 7.0 (2002).

[39] The Engineering Tool Box - 2015, http://www.engineeringtoolbox.com

[40] J. Riccius, J. Leiner, J. Castro, J. Rigola. Hot run test results of a validation optimized water-ice phase change heat accumulator and comparison to numerical analysis. In *Proceedings of the 5th European Conference For Aerospace Sciences (EUCASS)*, 2013.

[41] M. Kawaji, Y.S. Ng, S. Banerjee, G. Yadigaroglu. Reflooding with steady and oscillatory injection: Part i—flow regimes, void fraction, and heat transfer. *Journal Heat Transfer*, 107:670–679, 1985.

[42] H. Hu, J. Chung, S.H. Amber. An experimental study on flow patterns and heat transfer characteristics during cryogenic chilldown in a vertical pipe. *Cryogenics*, 52, 2012.

[43] G.P. Celata, M. Cumo, M. Gervasi, G. Zummo. Quenching experiments inside 6.0 mm tube at reduced gravity. *International Journal of Heat and Mass Transfer*, 52:2807-2814, 2009.

Chapter 4

Parametric study of two-tank TES systems for CSP plants

Abstract.

The two-tank thermal energy storage (TES) system is the most used technology for storage in concentrating solar power (CSP) plants. This work focuses on a parametric study, which aims to identify the most important parameters on TES system, in order to improve the design and increase the performance of the plant. Three parameters have been considered: meteorological data, insulation thickness of the storage tank, and configuration of the foundation of the storage tank. The effect of each parameter is evaluated using numerical simulations based on a modular object-oriented methodology. The main issues related to the mathematical models and its numerical methodology are also presented in this chapter.

4.1 Introduction

Concentrated solar power (CSP) plants are experiencing considerable growth in recent years. They are based on well-proven technology for providing a considerable part of renewable electricity [1]. CSP uses renewable solar resource to generate electricity while producing very low levels of greenhouse-gas emissions. Thus, it has strong potential to be a key technology for mitigating climate change. There are four main CSP systems that perform the conversion of solar energy into electricity: parabolic troughs, power towers, linear Fresnel reflectors and parabolic dishes (see Fig. 4.1), which can be categorised by the way they focus the solar rays and the technology used to receive the solar energy (see for instance [2, 3]). Although they have different characteristics, the operating principle is the same. Reflector elements concentrate the solar rays into a receiver, where a heat transfer medium is heated, and use to drive a steam turbine.

Thermal energy storage (TES) systems can be considered a key aspect for concentrated solar power plants, as they provide not only dispatchable electricity but also stability to the electricity network in case of high fraction of renewable production or intermittences due to weather conditions. Today, the two-tank system employing molten salt are the most used configuration [4, 5], which make profit of the sensible energy changes of a heat transfer fluid (molten salt) under a temperature difference. The two-tank storage systems are subdivided into direct and indirect systems. In a direct system, the heat transfer fluid also serves as the storage medium, while in an indirect system, a second medium is used for storing the heat [6]. For instance, Gemasolar plant (located in Fuentes de Andalucia, near to Seville, Spain) has a power tower technology [7]. Its storage system is based on two-tank direct system (see Fig. 4.2). As an example of the two-tank indirect system is Andasol I [5] (see Fig. 4.3). This solar thermal power plant is located in Guadix, Granada (Spain), and the solar field is based on parabolic trough technology.

In the two-tank storage systems there are significant design considerations that must be taken into account, namely, avoiding the salt freezing by controlling the heat losses, and storage optimization (aspect ratio, design of the inlet ports, etc.). A profound knowledge of the thermal and fluid-dynamic phenomena present inside storage tanks is required to reduce/control heat losses and design optimization. Efforts made for integrating this technology within demonstration and commercial plants can be found in Refs. [5, 7]. In addition to the accumulative experience acquired in the sector, optimization techniques based on computational fluid dynamic and heat transfer (CDF&HT) are becoming an important tool. One of the few CFD&HT simulations carried out for these tanks was conducted by Schulte-Fischedick et al. [8]. In their work, they coupled a CFD simulation using a RANS model for evaluating the molten salt behaviour with a finite element method for the tank walls. More recently, Rodríguez et al. [9] presented a methodology for studying the molten salt TES

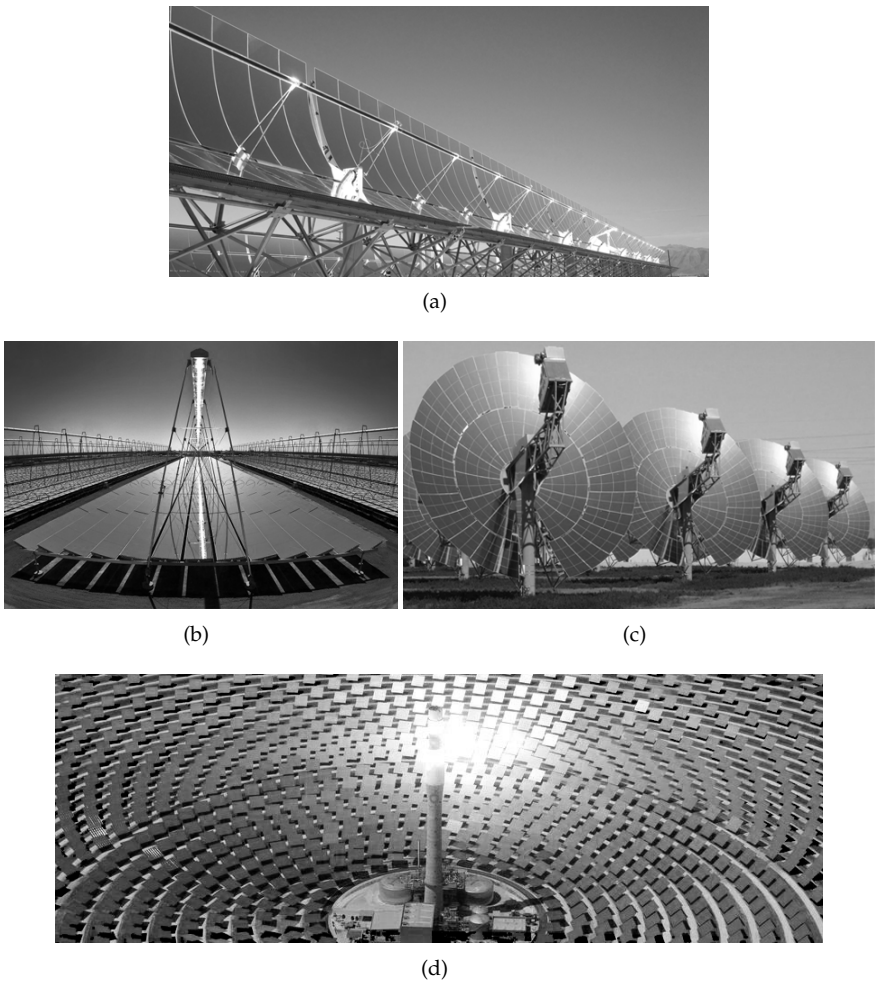

(a)

(b)

(c)

(d)

Figure 4.1: (a) parabolic troughs; (b)linear Fresnel reflectors; (c) parabolic dishes; (d) power tower.

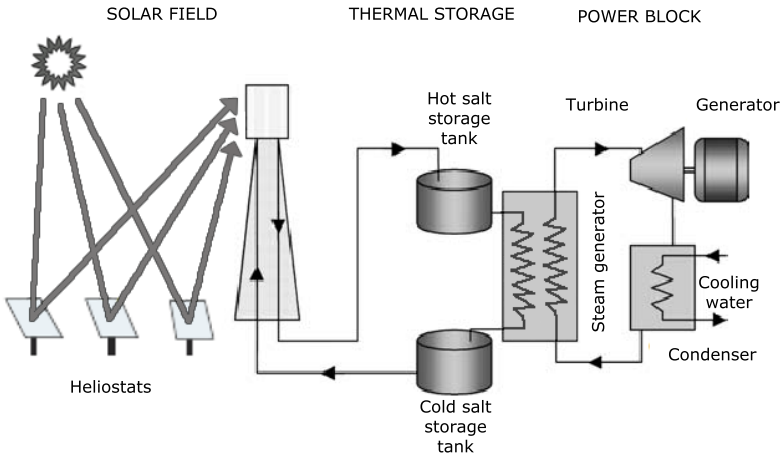

Figure 4.2: Direct storage system.

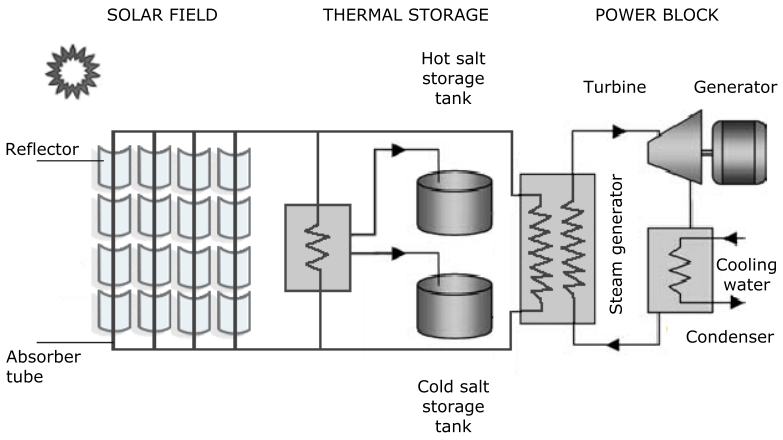

Figure 4.3: Indirect storage system.

by coupling different levels of modelisation in which the molten salt was evaluated using large eddy simulation (LES).

This paper follows the work carried out by Rodríguez et al. [9], but goes further in the concept presented. However, in this study a global model is used to solve the molten salt in order to take into account changes in the level of the fluid in the tank. Using the existing and new models implemented, a parametric study of the storage tank for CSP plants is carried out. From the work by Rodríguez et al. [9] and the current work, an in-house software called STEScode has been developed. The STEScode is based on a modular object-oriented methodology, and allows the detailed thermal and fluid dynamic analysis of sensible TES systems for designing purposes. More information about the STEScode can be found in Appendix A. With the STEScode, the influence of several parameters (geometry, materials, operational conditions and meteorological data) is studied in detail. In the next section, the main aspects of the numerical model are explained. After that, the reference case (section 4.3) and different results are presented (section 4.4).

4.2 Mathematical Model

The two-tank TES is considered to be formed by different elements, e.g. molten salt fluid, tank foundation, tank walls and insulation, etc., which interact each other through their boundary conditions. The modular object-oriented methodology used in this work is the same as the one presented by Rodríguez et al. [9, 10]. This implementation has been carried out within the NEST platform [11], which allows the linking between different elements of the thermal system. The mathematical model considers the transient behaviour of the molten salt fluid, the gas ullage, the tank walls and insulation, different configuration of the foundation, radiation exchange between the salt and the tank walls in the ullage. For a detailed description and derivation of the model, the interested reader is referred to a previously work [9]. A scheme of the energy balance at the different elements of the model and its boundary conditions is given in Fig. 4.4. A brief mathematical description is presented hereafter.

4.2.1 Molten salt global model

The molten salt fluid can be evaluated by means of global balances, together with the other elements through the boundary conditions. The mass and energy balances for the molten salt can be written as,

$$\frac{d}{dt}\int_{V_{ms}} \rho_{ms} dV + \dot{m}_{ms}^{out} - \dot{m}_{ms}^{in} = 0 \tag{4.1}$$

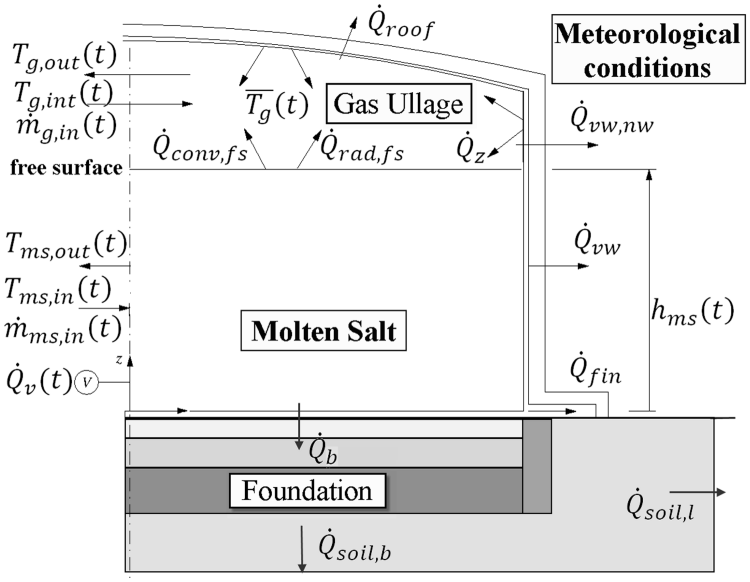

Figure 4.4: Boundary conditions of the different elements of the storage tank.

$$\frac{d}{dt}\int_{V_{ms}} \rho_{ms} u_{ms} dV + (\dot{m}u)_{ms}^{out} - (\dot{m}u)_{ms}^{in} = -\dot{Q}_b - \dot{Q}_{vw} - \dot{Q}_{fs} + \int_{S_{ms}} \vec{v}_{ms} \cdot \vec{f}_{(\vec{n})} dS \quad (4.2)$$

In the energy equation, kinetic variation and viscous dissipation have been considered negligible. The change in internal energy and the heat flux can be interpreted as the sum of all the heat losses through the tank foundation (equation 4.3), the vertical walls (equation 4.4), and through the molten salt free surface (equation 4.5):

$$\dot{Q}_b = \int_{S_b} \alpha_{ms}^{b} (\bar{T}_{ms} - T_t) dS \quad (4.3)$$

$$\dot{Q}_{vw} = \int_{S_{vw}} \alpha_{ms}^{vw} (\bar{T}_{ms} - T_t) dS \quad (4.4)$$

$$\dot{Q}_{fs} = \int_{S_{fs}} \left[\alpha_{ms}^{fs} (\bar{T}_{fs} - \bar{T}_g) + \varepsilon_{ms} \sigma T_{fs}^4 - \varepsilon_{fs} \dot{g}_{fs} \right] dS \quad (4.5)$$

4.2.2 Gas ullage model

The region between the molten salt free surface and the top wall of the container is considered in the global methodology, as it contributes to the heat losses. The balance for the gas contained in this zone is:

$$\frac{d}{dt}\int_{V_g} \rho_g dV + \dot{m}_g^{out} - \dot{m}_g^{in} = 0 \quad (4.6)$$

$$\frac{d}{dt}\int_{V_g} \rho_g u_g dV + (\dot{m}u)_g^{out} - (\dot{m}u)_g^{in} = -\dot{Q}_{roof} - \dot{Q}_{vw,g} - \dot{Q}_{fs} + \int_{S_g} \vec{v}_g \cdot \vec{f}_{(\vec{n})} dS \quad (4.7)$$

Similar to the other objects, the gas ullage is linked through its boundary conditions with the molten salt free-surface and the container walls.

4.2.3 Tank walls and insulation

Any solid wall, including the container and the insulation material, can be evaluated by means of a transient heat balance as,

$$\rho c_p \frac{\partial T}{\partial t} = \nabla \cdot (\lambda \nabla T) \quad (4.8)$$

The above equation is evaluated for each wall layer of the object, and linked with the appropriate boundary conditions. For instance:

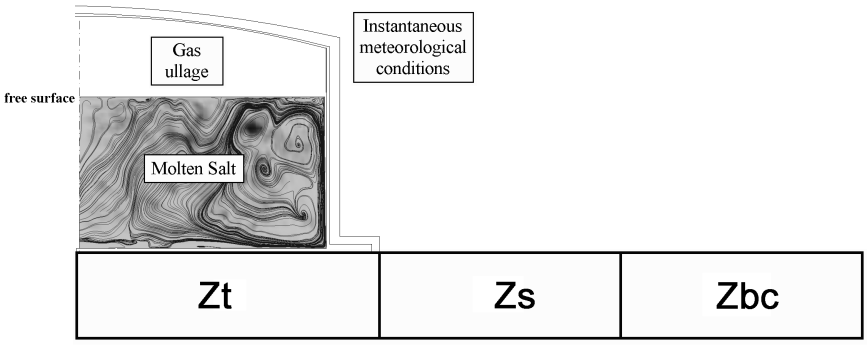

Figure 4.5: Schematic representation of the foundation model.

- With the molten salt object as,

$$\alpha_{ms}^{vw}(T_{ms} - T_t) = -\lambda_t \frac{\partial T_t}{\partial r} \tag{4.9}$$

- With internal interfaces/ walls as,

$$-\lambda_t \frac{\partial T_t}{\partial n} = -\lambda_i \frac{\partial T_i}{\partial n} \tag{4.10}$$

- With external conditions as,

$$-\lambda_i \frac{\partial T_i}{\partial n} = \alpha_{ext}(T_i - T_{ext}) + \varepsilon_i \sigma (T_i^4 - T_{sky}^4) - \dot{q}_s \tag{4.11}$$

4.2.4 Foundation (simplified zonal model)

In [9] an advance multidimensional model was used. However, a much faster (from a computational point of view) model for the foundation has been developed considering three main zones. According to Fig. 4.5, a main zone Zt just below the tank is defined with the different foundations materials. Next to this zone, a second one, called Zs, allows for radial heat transfer losses. Finally, zone Zbc corresponds to the transient evolution of the temperature at the soil, far from the tank, and considering soil characteristics and the specific meteorological conditions.

The foundation of the storage tank (Zt) is composed of different layers; each of one is evaluated as,

$$\rho_i C_{pi} \frac{\partial T_i}{\partial t} = \nabla \cdot (\lambda_i \nabla T_i) - \dot{q}_{v,i} \qquad i = 1, 2, 3, ..., N \tag{4.12}$$

In general $\dot{q}_{v,l} = 0$, except in the layer with passive cooling. The passive cooling is a natural convective air cooling that is installed in the foundation, in order to dissipate heat gain through the transfer of heat from the tank. Depending on the layer, different boundary conditions are set:

- For the surfaces at the top:

  first radial zone, Zt:

  $$-\lambda_i \frac{\partial T_i}{\partial z} = -\lambda_t \frac{\partial T_t}{\partial z} \tag{4.13}$$

  second radial zone, Zs:

  $$-\lambda_j \frac{\partial T_j}{\partial z} = \alpha_{gr}(T_j - T_{ext}) + \dot{q}_{j,lateral} + \varepsilon_j \sigma (T_j^4 - T_{sky}^4) - \dot{q}_s \tag{4.14}$$

  third radial zone, Zbc:

  $$-\lambda_k \frac{\partial T_k}{\partial z} = \alpha_{gr}(T_k - T_{ext}) + \dot{q}_{k,lateral} + \varepsilon_k \sigma (T_k^4 - T_{sky}^4) - \dot{q}_s \tag{4.15}$$

- For the internal interfaces,

  $$-\lambda_{(i,j,k)-1} \frac{\partial T_{(i,j,k)-1}}{\partial n} = -\lambda_i \frac{\partial T_{(i,j,k)}}{\partial n} \tag{4.16}$$

- For the bottom surface, $T = T_{soil}$ (soil temperature is from at some distance from the surface).

In summary, the model solves the unsteady evolution of the thermal and fluid dynamic behaviour of the tank considering in a couple manner the contribution of the different element: tank shell, salt, ullage, outdoor conditions, foundation, etc. The model considers the meteorological information with the outdoor element (unsteady weather data). The foundation can be solved using detailed multidimensional models or an unsteady zonal model, where the passive cooling can be active. The variation of the height of the molten salt is taken into account to use more realistic boundary conditions.

Characteristics	Reference CSP plant
Turbine net capacity (MW_{el})	50
Technology	solar power tower
Operating scenario	Solar only, no hybrid operation
Solar field area (m^2)	630,000
Solar multiple	2
DNI at design	800 W/m^2
Heat transfer fluid	Molten salt (60% $NaNO_3$ and 40% KNO_3)
Receiver outlet temperature ($^\circ C$)	565
Power block efficiency	0.42
Storage capacity (h)	8

Table 4.1: Reference CSP plant.

4.3 Definition of the cases and parametric studies

4.3.1 Definition of the reference case

A reference CSP plant is defined in this section. Parametric studies will be based on this plant. The geometry and configuration of the reference CSP plant is defined with the data given in Table 4.1. In these cases, cooling-down processes of the hot (Tms = 565 $^\circ C$) and cold (Tms = 290 $^\circ C$) storage tanks are considered. The molten salt is a mixture of 60% NaNO3 and 40% KNO3. The tank container is of stainless steel A240gr347, and as insulation material for the lateral and roof walls Spintex 342G-100 is used. Also the insulation material is covered with a thin layer of aluminium 2024-T6.

Details about geometry used in the reference case are given hereafter (see Fig. 4.6 (a)):

- Storage tanks internal height and radii H_{tank} = 12 m; r_1 = 11.80 m; r_2 = 12.205 m and r_3 = 12.45 m.
- The vertical wall has different thicknesses as a function the tank height, e_{vw1} = 0.039 m ($0 \leq z \ll \Delta z$); e_{vw2} = 0.032 m ($\Delta z \leq z \ll 2\Delta z$);
  e_{vw3} = 0.0255 m ($2\Delta z \leq z \ll 3\Delta z$); e_{vw4} = 0.0185 m ($3\Delta z \leq z \ll 4\Delta z$);
  e_{vw5} = 0.0115 m ($4\Delta z \leq z \ll 5\Delta z$); e_{vw6} = 0.010 m ($5\Delta z \leq z \ll 6\Delta z$),
  where Δz = 2.0 m.
- Similar to vertical wall, bottom wall also considers different thicknesses as a function of the distance from the tank centre,
  e_{b1} = 0.014 m ($0 \leq r \ll r_1$); e_{b2} = 0.021 m ($r_1 \leq r \ll r_3$).

Molten salt [13]		
ρ	$2090 - 0.636T$	$[kg\ m^{-3}]$
c_p	$1443 - 0.172T$	$[J\ kg^{-1}\ K^{-1}]$
μ	$2.2714\text{x}10^{-2} - 1.24\text{x}10^{-4}T + 2.281\text{x}10^{-7}T^2 - 1.474\text{x}10^{-3}T^3$	$[kg\ m^{-1}\ s^{-1}]$
λ	$0.443 + 1.9\text{x}10^{-4}T$	$[W\ m^{-1}\ K^{-1}]$
Stainless steel A240gr347		
ρ	8000	$[kg\ m^{-3}]$
c_p	500	$[J\ kg^{-1}\ K^{-1}]$
λ	$14.604 + 0.0151T$	$[W\ m^{-1}\ K^{-1}]$
Insulation Spintex342G-100 [14]		
ρ	100	$[kg\ m^{-3}]$
c_p	1666	$[J\ kg^{-1}\ K^{-1}]$
λ	$3.3453\text{x}10^{-2} + 8.2005\text{x}10^{-5}T + 3.252\text{x}10^{-3}T^2$	$[W\ m^{-1}\ K^{-1}]$
Aluminium 2024-T6 [15]		
ρ	2270	$[kg\ m^{-3}]$
c_p	$663 + 0.6375\hat{T}$	$[J\ kg^{-1}\ K^{-1}]$
λ	$140 + 0.115\hat{T}$	$[W\ m^{-1}\ K^{-1}]$

Table 4.2: Thermo-physical properties of the molten salt and different material used in the tank shell simulation.($\hat{T}(K)$ and $T(^\circ C)$). Stainless steel A240gr347 adapted from ASME 31.1-2001 standart.

- Insulation thickness: e_{aisl} = e_{r2} = 0.4 m (hot tank).
- Foundation thicknesses (Fig. 4.6 (b)) defined as foundation 1 (FDN 1) in the results: dry sand, e_1 = 0.006 m; foam-glass, e_2 = 0.420 m; heavy weight concrete, e_3 = 0.450 m; soil, e_4 = 9.140 m.

The detailed information about the thermo-physical properties of the materials used in the simulation are given in Tables 4.2 and 4.3.

In addition, for the reference case the meteorological information from Sevilla is considered (data base of the software METEONORM version 4.0 [12]). The soil temperature is set at Tsoil = 15 $^\circ C$ at 10 meters. For the parametric studies, the molten salt heaters and the passive cooling in the foundation were disabled. The simulations have been started the 1st day of January at 0:00 a.m.

4.3.2 Operating conditions

The simulations are carried out for a years. With the CSP plant information (Table 4.1), the geometric dimensions of the storage tanks given above, and the meteorolog-

Sand [15]		
ρ	1515	$[kg\ m^{-3}]$
c_p	800	$[J\ kg^{-1}\ K^{-1}]$
λ	0.027	$[W\ m^{-1}\ K^{-1}]$
Foam-glass [15]		
ρ	165	$[kg\ m^{-3}]$
c_p	840	$[J\ kg^{-1}\ K^{-1}]$
λ	0.045	$[W\ m^{-1}\ K^{-1}]$
Heavy weight concrete [15]		
ρ	2300	$[kg\ m^{-3}]$
c_p	1000	$[J\ kg^{-1}\ K^{-1}]$
λ	1.63	$[W\ m^{-1}\ K^{-1}]$
Soil [15]		
ρ	1600	$[kg\ m^{-3}]$
c_p	1435	$[J\ kg^{-1}\ K^{-1}]$
λ	0.99	$[W\ m^{-1}\ K^{-1}]$
Arlita [16]		
ρ	425	$[kg\ m^{-3}]$
c_p	$764.2 + 1.338\hat{T}$	$[J\ kg^{-1}\ K^{-1}]$
λ	if $(\hat{T} <= 673.75K)$ $1.2145\text{x}10^{-2} + 3.18\text{x}10^{-4}\hat{T}$	$[W\ m^{-1}\ K^{-1}]$
	if $(\hat{T} > 673.75K)$ $-0.54879 + 1.5\text{x}10^{-3}\hat{T}$	$[W\ m^{-1}\ K^{-1}]$

Table 4.3: Thermo-physical properties of the different material used in the foundation simulation.($\hat{T}(K)$ and $T(^{\circ}C)$).

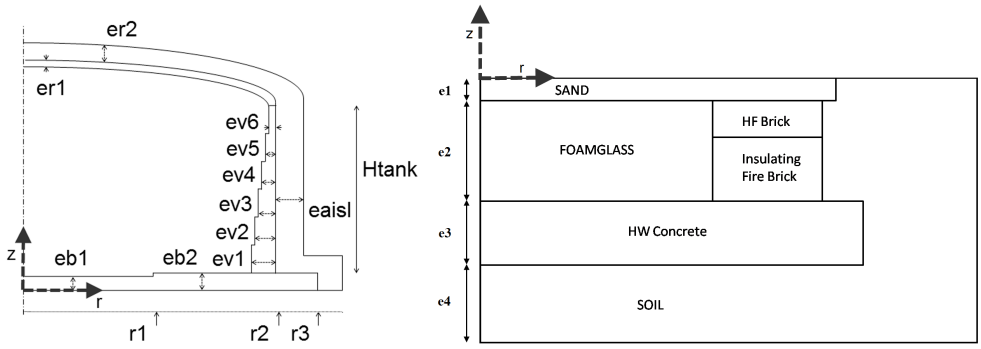

Figure 4.6: Schematic representation of: (a) the storage tank; (b) the reference foundation.

ical data obtained from the software METEONORM [12], the operating conditions of the storage tanks (inlet and outlet mass flow rate) are calculated. The following is an explanation of how the operating conditions are calculated in the two-tank direct system.

For determining the power coming from the solar field, the following equation is used:

$$\dot{Q}_{SF} = DNI.A_{SF}.\eta_{SF} \tag{4.17}$$

where the direct normal irradiance (DNI) is multiplied by the solar field area (A_{SF}) and the overall efficiency of the solar field (η_{SF}), which in these cases are taken as 0.475. The mass flow coming from the solar field is calculated:

$$\dot{m}_{SF} = \frac{DNI.A_{SF}.\eta_{SF}}{c_p.\Delta T_{SF}} \tag{4.18}$$

The hot fluid coming out of the SF is set at a fixed temperature of $565°C$, while the cold fluid entering the SF, coming from the cold tank and has a variable temperature.

For determining the power coming from the hot tank and the mass flow necessary for generating nominal power in the power block (PB), the following equations are used:

$$\dot{Q}_{PB} = \frac{\dot{W}_e^g}{\eta_{PB}} \tag{4.19}$$

$$\dot{m}_{PB} = \frac{\dot{Q}_{PB}}{c_p.\Delta T_{PB}} \tag{4.20}$$

The hot fluid coming from the hot tank out has a variable temperature. It is calculated during the simulation, while the temperature of the fluid that going out of the power block is set at a fixed temperature of 290$^{\circ}C$.

To avoid starts and stops at small time intervals, are defined a criteria for the start and stop of the pumps. The pumps start when the height of molten salt in the hot tank is more than 2.4 m; the pumps stop occurs when the height of molten salt in the hot tank reaches a minimum or maximum level defined, 0.7 m and 10.9 m, respectively.

4.3.3 Parameter candidates

Three main aspects have been selected in this parametric study: meteorological data, insulation thickness of the storage tank and configuration of the foundation. To illustrate the influence of the meteorological data, four locations of interest in the CSP field were selected: Sevilla (Spain), Ouarzazate (Morocco), Las Vegas (United States) and Upington (South Africa), see Table 4.4. For each one, the following meteorological information is used: variable solar radiation, wind speed and direction, relative humidity, sky and ambient temperature. Figs. 4.7 and 4.8 show the environment temperature and the direct normal irradiance.

For each location, and taking into account their meteorological data, the inlet and outlet mass flow of the molten salt in the hot and cold tanks were calculated considering base load conditions. The meteorological data for each site for the 8,760 hours in a reference year was generated from the software METEONORM [12]. The essential data of the locations are given in Table 4.4. As mentioned above, the location for the reference case is Sevilla.

The second parameter considered in this study is the insulation thickness of the hot storage tank. Four thicknesses have been considered: 0.2 m, 0.3 m, 0.4 m (reference case) and 0.5 m. The last parameter considered is related to the configuration of the foundation. Fig. 4.9 shows the configuration and dimensions of the foundation of the new case foundation 2 (FDN 2) (the reference case is defined in Fig. 4.6(b)).

For the parametric study of insulation thickness and configuration of the foundations the same meteorological information and the same operating conditions are used in the storage tank, as is shown in Fig. 4.10.

The parametric study is then conducted using the described numerical model by varying one parameter at a time. The objective is to investigate the effect of each parameter on the storage tank performance.

Location	Latitude (°)	Longitude (°)	January			July		
			Tmax ($°C$)	Tmin ($°C$)	DNI (kWh/m^2 day)	Tmax ($°C$)	Tmin ($°C$)	DNI (kWh/m^2 day)
Sevilla, ESP	37.37	5.97	21.1	3.2	4.59	39.9	16.2	7.67
Ouarzazate, MAR	30.93	6.90	20.4	-0.5	4.51	41.8	20.4	6.61
Las Vegas, USA	36.08	115.01	20.7	-9.4	4.71	44.3	21.7	8.29
Upington, RSA	-28.47	-21.27	40.7	14.9	8.32	26.6	0.4	6.62

Table 4.4: Selected locations with basic data.

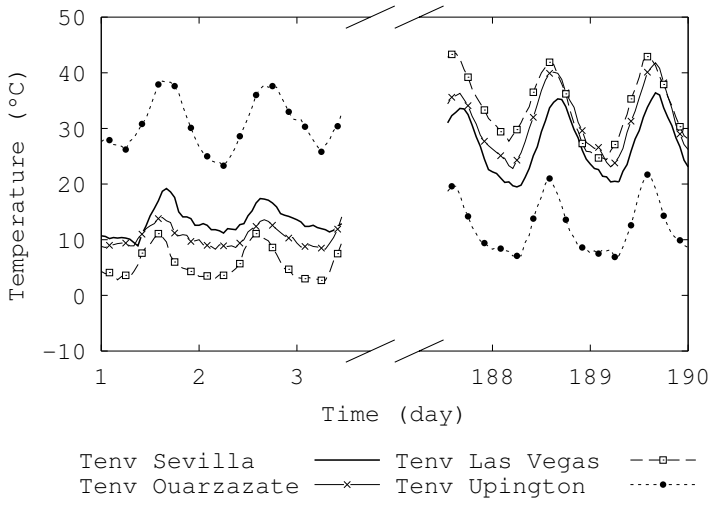

Figure 4.7: Boundary conditions of the storage tank system (for different locations). Input data: ambient temperatures.

4.4 Parametric study

In order to analyse the influence of the selected parameters, different simulations have been carried out taking into account the transient behaviour of the thermal energy storage system. The resulting simulation provides a year of performance data for the storage system. In order to get rid of the initial transient and due to the large thermal inertia of the foundations, four years are previously simulated before the system performance is evaluated. Moreover, selected results are presented considering 3 consecutive days in winter and 3 consecutive days in summer.

4.4.1 Effect of meteorological data

The most important parameter in the meteorological data is the direct normal irradiance (DNI), which is reflected onto the receiver. The heat collected by the solar receiver from the heliostat field strongly affects the mass flow rate of molten salt that goes to the receiver from the hot tank. Four locations with different meteorological data were selected for the study. Global results of the performance of the plant obtained in the simulations are given in Table 4.5.

The results in the Table above correspond with the information given in Table 4.4,

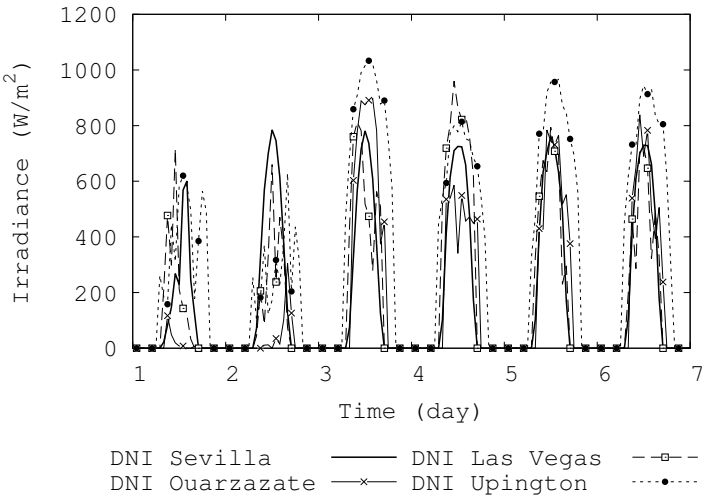

(a)

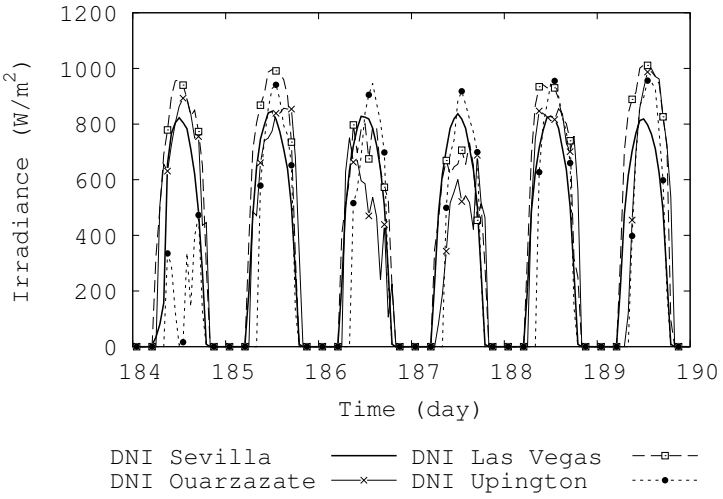

(b)

Figure 4.8: Boundary conditions of the storage tank system (for different locations). Input data: direct normal irradiation. (a) From 1 to 6 of January; (b) From 4 to 9 of July.

Location	Capacity factor (%)	Full load hours (h/y)	Net electric (GWh/y)
Sevilla, ESP	0.55	4815	240.8
Ouarzazate, MAR	0.52	4583	229.2
Las Vegas, USA	0.63	5544	277.2
Upington, RSA	0.67	5880	293.9

Table 4.5: Result of the performance of the two-tanks molten salt storage for different locations.

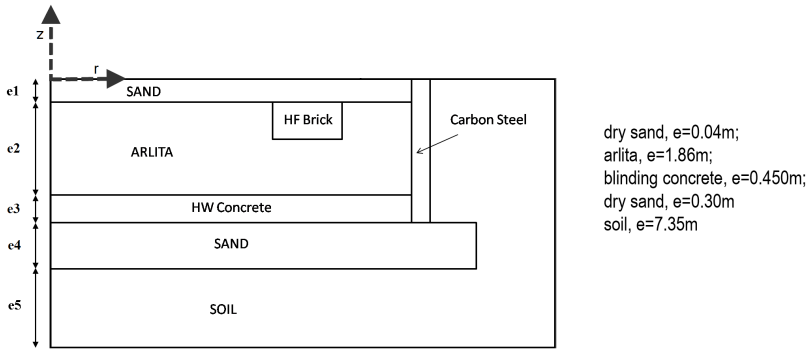

Figure 4.9: Schematic representation of the configuration and dimensions of the foundation is used for the parametric study.

where the DNI for the months of January and July for each location were shown. As expected, the highest the DNI the highest the plant capacity factor. The performance of the CSP plant depends significantly on the DNI, which depends on the geographical location and the meteorological conditions of the site. The results indicate that for the specified operating conditions and plant performance, Upington is more suitable for this specific CSP plant.

Fig. 4.11 shows the transient behaviour of the height of molten salt in the hot tank for the different locations. The greater effect of the DNI on the use of the hot tank can be clearly seen. It is also observed that the use of the tanks are appropriate for the plant performance.

Fig. 4.12 (a) shows the comparison between the molten salt temperatures in the hot tank for the different locations. In Fig. 4.12 (b) the simulated transient evolution of the total heat loss of the molten salt in the hot tank is shown. As can be seen, heat losses vary along the day depending on the level of salt in the tank. The total heat losses throughout the year are very similar for the different locations, as shown in Table 4.6.

4.4.2 Effect of the insulation thickness

The insulation thickness affects the heat losses between the molten salt and the environment. For this study the same meteorological information and the same operating conditions are used in the storage tank. The results of these simulations are shown in Figs. 4.13 and 4.14, and Table 4.7.

Fig. 4.13 (a) shows the transient evolution of temperature in the molten salt for

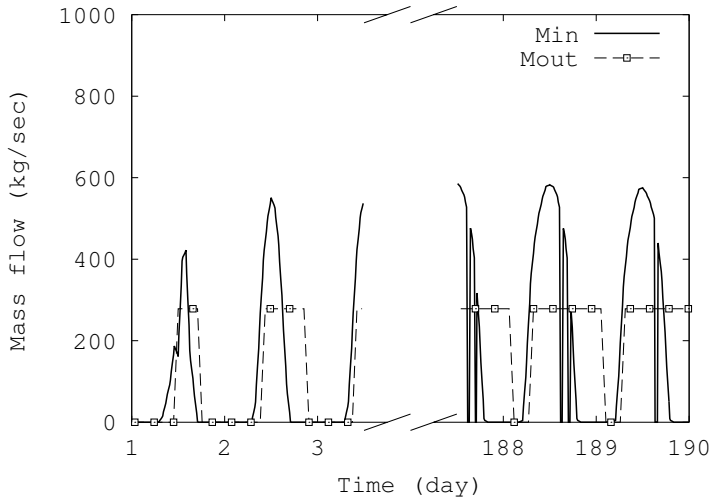

(a)

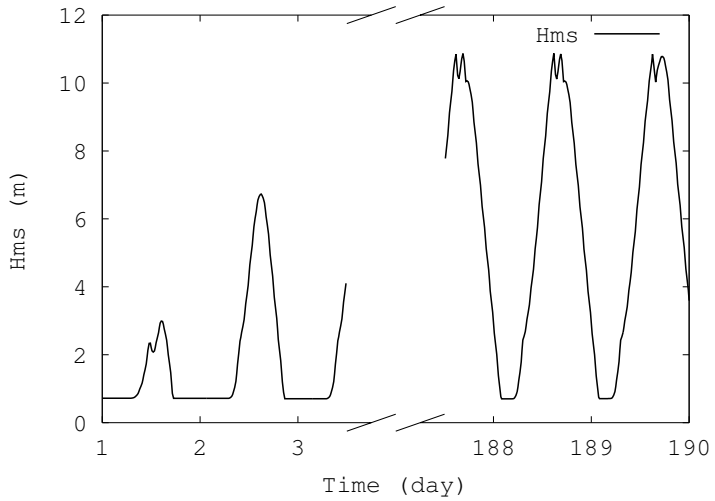

(b)

Figure 4.10: Boundary conditions of the hot storage tank (for the reference case). Input data: (a) Mass flow of molten salt in operating mode; (b) Height of the molten salt.

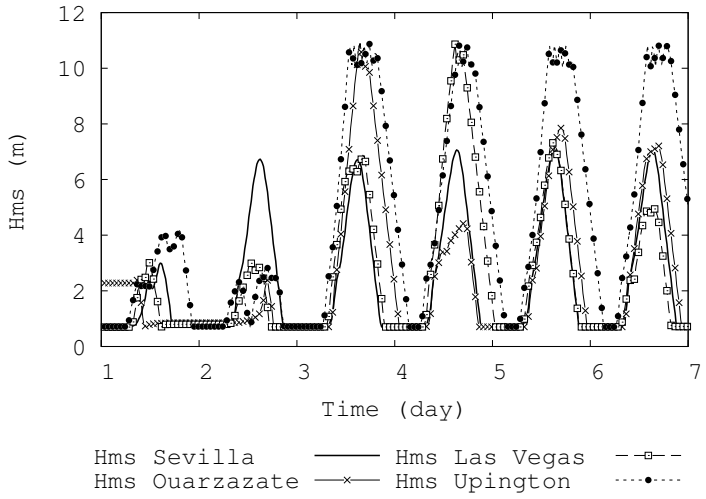

(a)

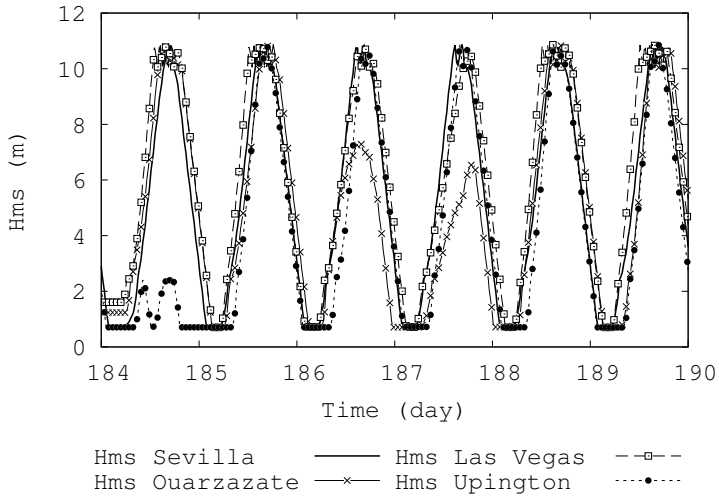

(b)

Figure 4.11: Transient evolution of the height of molten salt in the hot tank for different location: (a) From 1 to 6 of January; (b) From 4 to 9 of July.

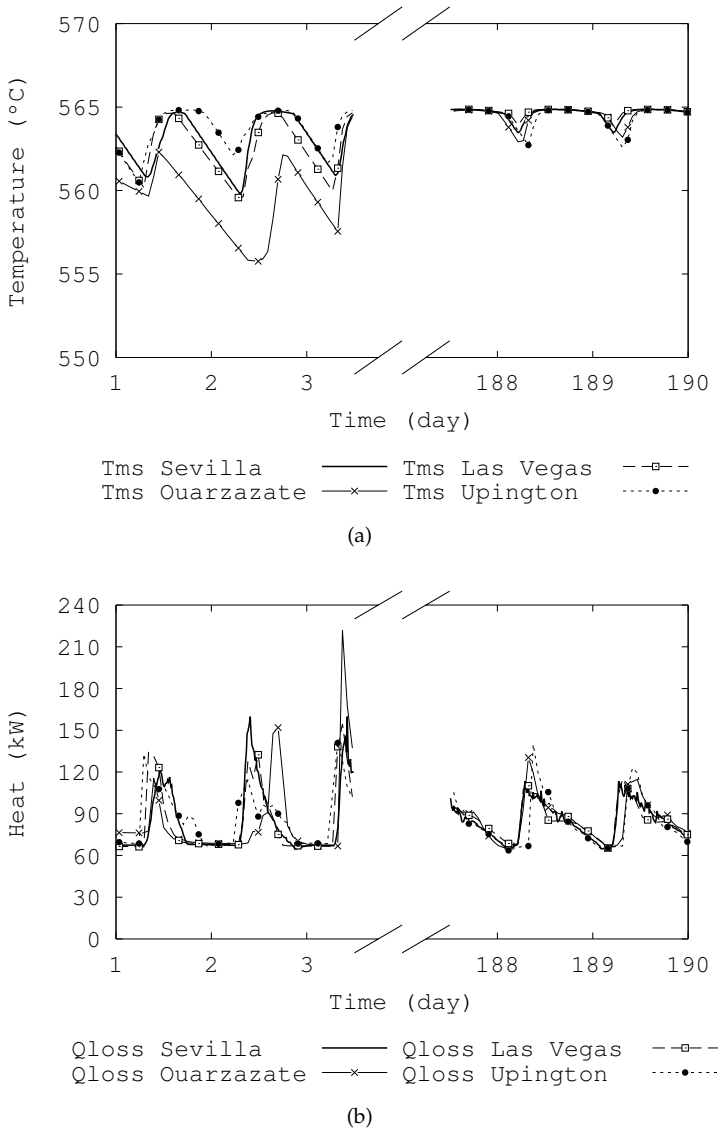

Figure 4.12: Transient evolution of the molten salt in the hot tank for different location: (a) Molten salt temperature; (b) Total heat losses by the molten salt.

Location	Bottom (kW)	Wetted lateral wall(kW)	Gas ullage (kW)	Total (kW)
Sevilla, ESP	17.36	18.97	47.46	83.79
Ouarzazate, MAR	17.35	17.81	48.57	83.73
Las Vegas, USA	17.35	22.23	44.57	84.14
Upington, RSA	17.34	23.64	43.36	84.34

Table 4.6: Average heat losses in the molten salt of the year for different location.

the different insulation thickness. The total heat losses by the molten salt are shown in Fig. 4.13 (b). As expected, when insulation thickness decreases, the heat losses of the storage tank increases and the molten salt temperature decreases.

The heat losses in the molten have been distinguished in location (lateral wall, gas ullage, bottom wall). Fig. 4.14 depicts the influence of the insulation thickness on the heat losses through the vertical wall (a) and the gas ullage (b) locations. These heat losses have a strong dependency of the height of the molten salt. In the case of the heat loss in the lateral wall, is due to the convective heat transfer between the molten salt and the wetted lateral wall and, it is greater with increasing height of the molten salt. On the other hand, the heat loss in the gas ullage location, when the lower height of the molten salt is, the higher is the heat loss, in this case due to the radiation heat transfer. In addition, the greater effect of the insulation thickness on the temperature and the heat losses can be clearly seen. As expected, the heat losses are reduced as the thickness of the insulation is increased, as shown in Table 4.7. The convective heat transfer at the bottom is quite independent of the insulation thickness. In contrast, in the gas ullage location, where the radiation heat transfer is heavily dependent on the insulation thickness. Due to the temperature decrease of the tank in the roof and the no wetted lateral walls.

4.4.3 Effect of the configuration of the foundation

Regarding the configurations and dimensions of the foundation, as aforementioned, two different configurations are considered. Results obtained for two situations considered, FDN 1 (reference case) and FDN 2, are plotted in Fig. 4.15. As can be seen in Table 4.8 and Fig. 4.15 (a), the impact of the change in configuration is of minor relevance when heat losses in the molten salt are analysed as a whole. However, a closer inspection to the heat losses through the bottom wall (Fig. 4.15 (b)) reveals that there exist differences when using the second type of foundation. The heat losses with the tank bottom is reduced by 27.5%. These differences, although small, should be considered when designing the storage as they can lead to a reduction of the operation cost of the whole system.

Figs. 4.16 and 4.17 show the temperature in the ground of the two configurations FDN 1 and FDN 2, respectively, and corresponding to the 29th day of June of each year of operation of the plant. The hot top surface can be easily seen in the close-up of the top part of the domain, which shows how the temperature changes along the depth of the ground.

The most important consideration in the foundation, is the thermal cycling and long-term exposure to elevated temperatures of the materials that compose the foundation. The maximum concrete temperature has been limited to prevent cracking and durability problems [17]. Studies have shown that the long-term durability of certain concretes can be compromised if the maximum temperature after placement

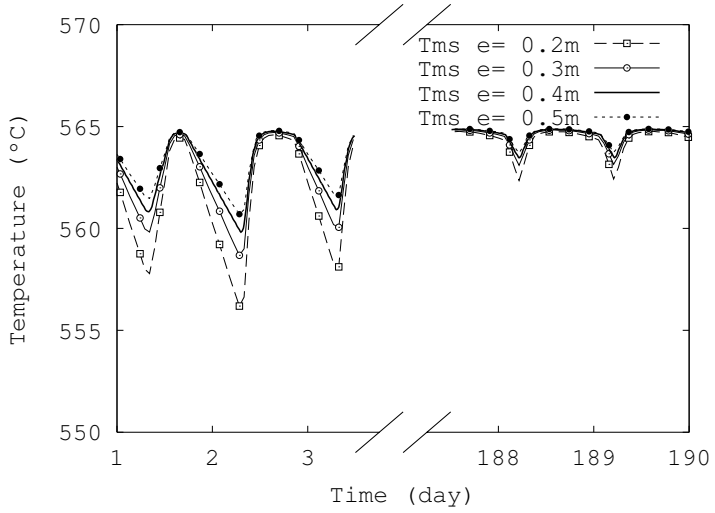

(a)

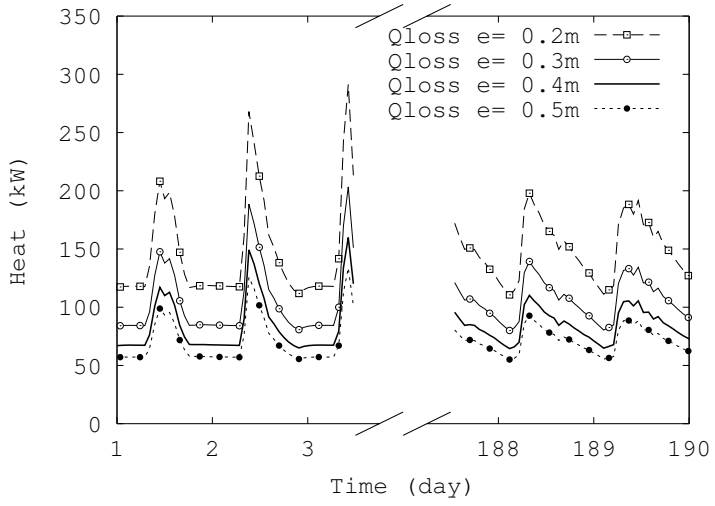

(b)

Figure 4.13: Transient evolution of the molten salt in the hot tank for different insulation thickness: (a) Molten salt and gas ullage temperatures; (b) Total heat losses in the molten salt.

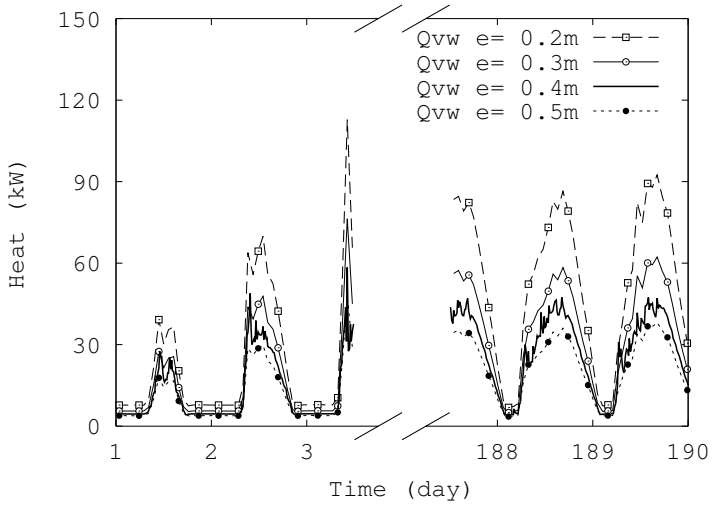

(a)

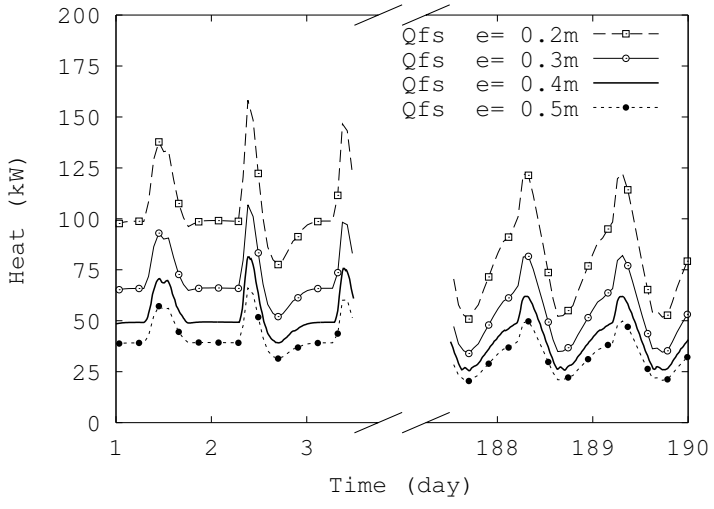

(b)

Figure 4.14: Heat losses in the molten salt for different insulation thickness: (a) through the tank lateral wall; and (b) with the gas ullage.

Thickness (m)	Bottom (kW)	Wetted lateral wall(kW)	Gas ullage (kW)	Total (kW)
0.2	17.88	35.95	94.03	147.86
0.3	17.53	24.62	63.05	105.20
0.4	17.36	18.97	47.46	83.79
0.5	17.26	15.58	38.08	70.92

Table 4.7: Average heat losses in the molten salt of the year for different thickness of insulation.

Configuration	Bottom (kW)	Wetted lateral wall(kW)	Gas ullage (kW)	Total (kW)
FDN 1	17.36	18.97	47.46	83.79
FDN 2	12.58	19.97	47.39	79.93

Table 4.8: Average heat losses in the molten salt of the year for different configuration of the foundation.

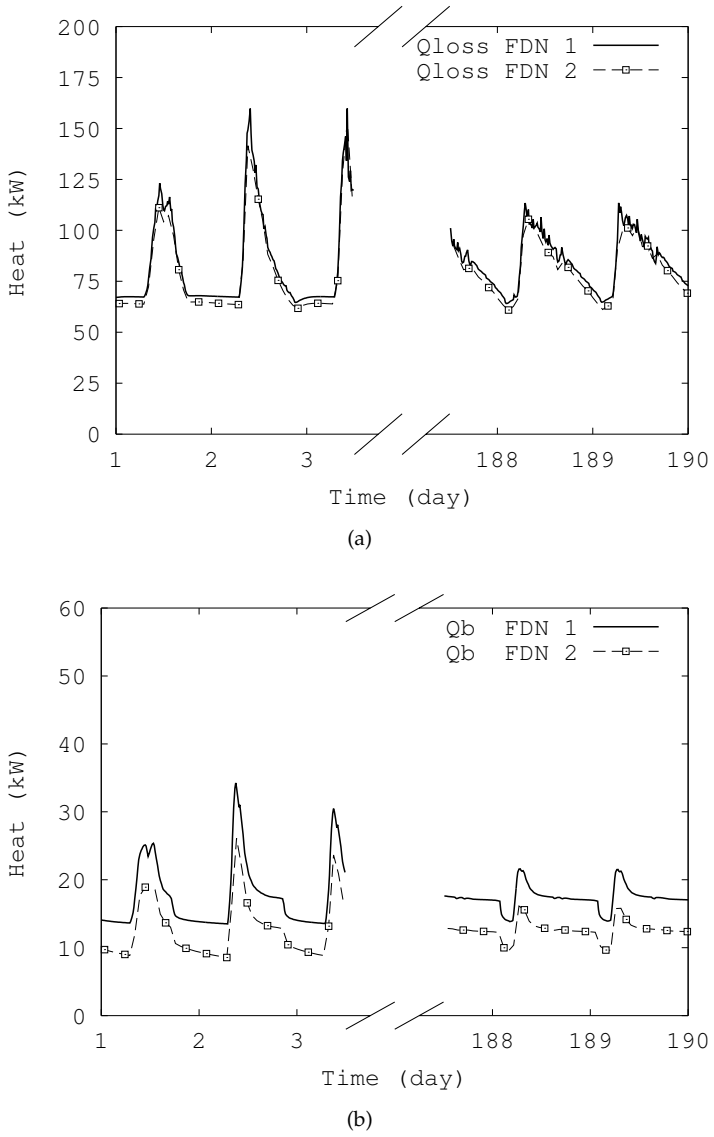

Figure 4.15: (a) Total heat losses in the molten salt; (b) Heat losses in the molten salt with the tank bottom wall.

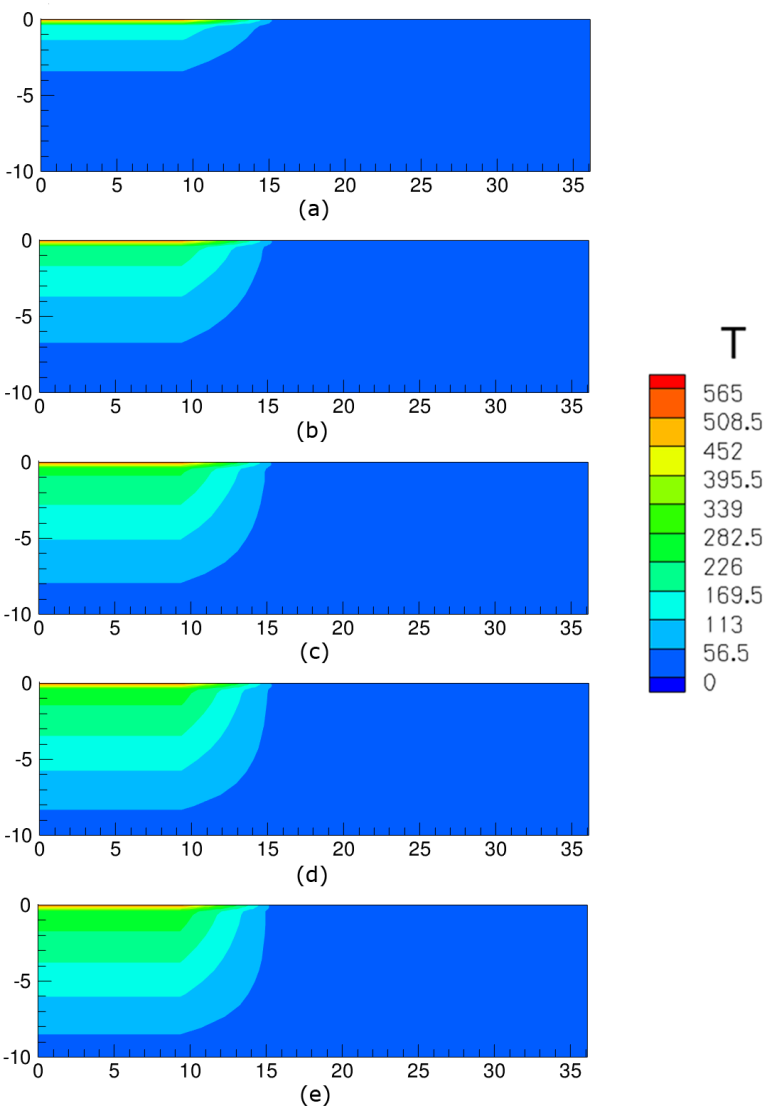

Figure 4.16: Temperature in the ground for the configuration FDN 1 (foam glass; reference case) on June 29 of each year of operation of the plant: (a) year 0; (b) year 1; (c) year 2; (d) year 3; and (e) year 4.

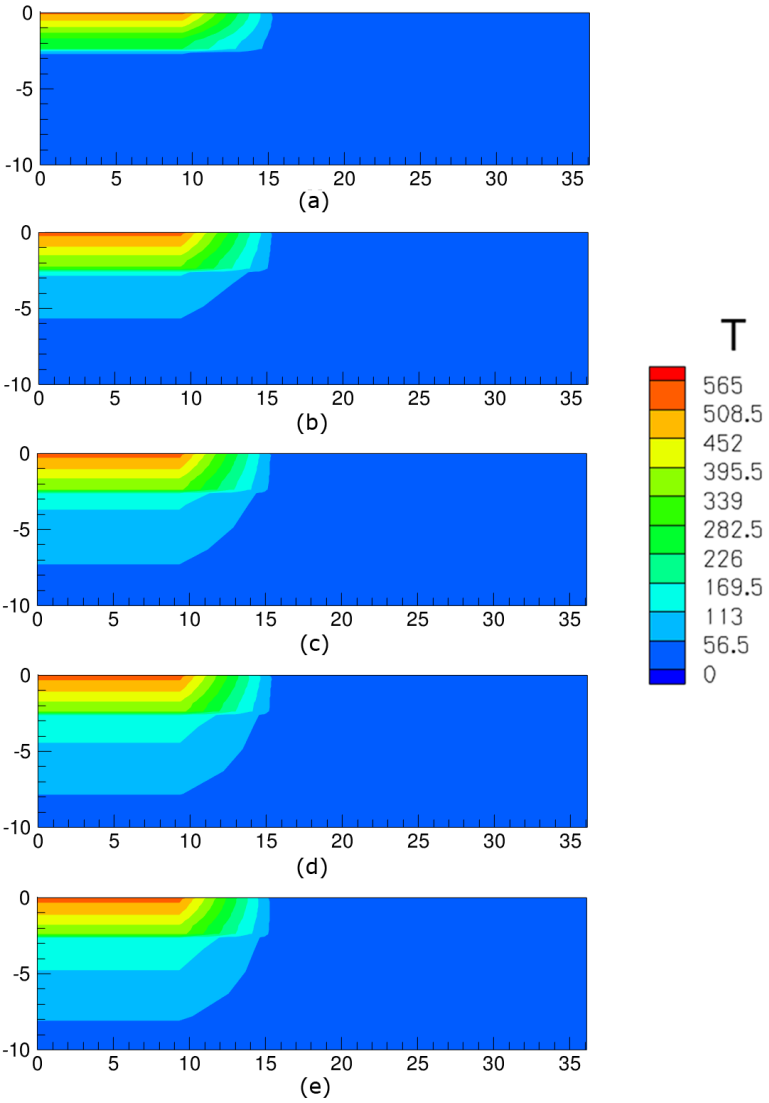

Figure 4.17: Temperature in the ground for the configuration FDN 2 ((arlita) on June 29 of each year of operation of the plant: (a) year 0; (b) year 1; (c) year 2; (d) year 3; and (e) year 4.

exceeds the range of 121 $^{\circ}C$ [18]. The cracking of concrete may not be evident for several years after placement. For this reason, a natural convective air cooling (passive cooling) of the concrete is installed in the foundation, in order to keep the concrete temperature of about 90 $^{\circ}C$. This aspect should also be considered in the configuration FDN 2, but the working temperature range of the concrete is lower. The configuration FDN 2 is currently being used mostly for the foundation in the thermal energy storage system in concentrating solar power (CSP) plants.

4.5 Conclusions

An in-house software called STEScode has been developed. This software has been used for the prediction of direct and indirect two-tank storage systems. The STEScode is based on a modular object-oriented methodology and takes advantage of the existing NEST platform [11]. It allows the detailed thermal and fluid dynamic analysis of sensible TES systems for designing purposes and with a reasonable computational effort.

The mathematical model used in the STEScode considers the transient behaviour of the molten salt fluid, the gas ullage, the tank walls and insulation, different configuration of the foundation, radiation exchange between the salt and the tank walls in the ullage. All the elements of the system are solved subjected to boundary conditions that come from neighbouring elements. Some of these elements have been specifically developed.

A parametric study of the hot storage tank for the hot storage tank for CSP plants has been carried out using the STEScode. Different variables have been considered for studying their effects on the performance of the storage system.

A CSP plant of 50MWe with solar power tower technology was defined and adopted as reference. Three main parameters have been considered in the parametric study: meteorological data, insulation thickness of the storage tank and configuration of the foundation of the storage tank. In order to obtain the influence of the selected parameters, different simulations have been carried out taking into account the transient behaviour of the thermal energy storage system. The resulting simulation provides a year of performance data for the storage system. In order to get rid of the initial transient, four years are previously simulated before the system performance is evaluated.

The influence of the normal direct radiation (DNI) on the operating conditions of the tank, and consequently on the plant behaviour, has been evaluated. The performance of the CSP plant depends significantly on the DNI, which depends on the geographical location and the meteorological conditions of the site. Four locations have been tested: Sevilla, Ouarzazate, Las Vegas and Upington. The results indicate that for the specified operating conditions and plant performance, Upington is more

suitable for this specific CSP plant, because it is the location with the highest capacity factor of the plant. The thickness of the insulation of the tank is an important parameter in the design of the tank in order to reduce the heat losses of the molten salt with the external environment. Four thicknesses have been checked (0.2 m, 0.3 m, 0.4 m and 0.5 m). The heat losses at the bottom are almost independent of the insulation thickness. Contrary, the heat losses in the gas ullage location are heavily dependent on the insulation thickness. Due to the radiation heat transfer effect. Finally, two configuration of the foundation have been employed. It can be said that even though the configuration of the foundation has not a great influence on the heat losses, it is important to take it into account for the design of the storage tank, due to the thermal cycling and long-term exposure to elevated temperatures of the materials that compose the foundation, this is an important issue to prevent cracking and avoid durability problems. The results indicate that the configuration FDN 2 is better for this specific CSP plant, because it gives lower heat losses in the foundation and the temperature of the concrete is lower than the other configuration.

Nomenclature

c_p	specific heat capacity
D	diameter
e	thickness
$\vec{f}$	normal direction vector
$\dot{g}$	irradiation
H	height
$\dot{m}$	mass flow rate
n	normal direction
$\dot{Q}$	heat losses
$\dot{q}$	specific heat flux
$\dot{q}s$	solar radiation
r	radial direction, radius
S	surface area
T	temperature
t	time
u	internal energy
V	volume
$\vec{v}$	velocity vector

Greek symbols

α	superficial heat transfer coefficient

Δ	magnitude increment
ϵ	emissivity in the infrared region
λ	thermal conductivity
μ	dynamic viscosity
ρ	density
σ	Stefan-Boltzmann constant

Subscripts

$aisl$	insulation
b	bottom surface
$conv$	convection
ext	ambient conditions
fin	tank extension
fs	free surface
g	gas ullage
gr	ground
in	inlet conditions
l	lateral
ms	molten salt
out	outlet conditions
rad	radiation
$roof$	tank roof
s	solar radiation
sky	relative to sky radiation
$soil$	relative to soil
t	tank container
u	ullage
v	passive cooling
vw	vertical wall, wetted lateral wall

Superscripts

b	bottom surface
fs	free surface
in	inlet conditions
out	outlet conditions
vw	vertical wall

References

[1] R. Sioshansi, P. Denholm. The value of concentrating solar power and thermal energy storage. Technical Report NREL/TP-6A2-45833. National Renewable Energy Laboratory, Colorado, USA, 2010, www.nrel.gov.

[2] H.L. Zhang, J. Baeyens, J. Degrève, G. Cacères. Concentrated solar power plants: review and design methodology. *Renewable and Sustainable Energy Reviews*, 22:466–481, 2013.

[3] OECD/IEA. Technology roadmap, concentrating solar power, 2010.

[4] U. Herrmann, B. Kelly, H. Price. Two-tank molten salt storage for parabolic trough solar power plants. *Energy*, 29:883–893, 2004.

[5] J. Ortega, J. Burgaleta, F. Tellez. Central receiver system solar power plant using molten salt as heat transfer fluid. *Journal of Solar Energy Engineering*, 130:1–6, 2008.

[6] M. Medrano, A. Gil, I. Martorell, X. Potau, L.F. Cabeza. State of the art on high-temperature thermal energy storage for power generation. Part 2—Case studies. *Renewable and Sustainable Energy Reviews*, 14:56–72, 2010.

[7] S. Relloso, J. Lata. Molten salt thermal storage: a proven solution to increase plant dispatchability. Experience in Gemasolar Tower plant. In *Proceeding of SolarPaces Congress*, 2011.

[8] J. Schulte-Fischedick, R. Tamme, U. Herrmann. CFD analysis of the cool down behaviour of molten salt thermal storage systems. In *Proceeding of Energy Sustainability*, 2008.

[9] I. Rodríguez, C.D. Pérez-Segarra, O. Lehmkuhl, A. Oliva. Modular object-oriented methodology for the resolution of molten salt storage tanks for CSP plants. *Applied Energy*, 109:402–414, 2013.

[10] I. Rodríguez, C.D. Pérez-Segarra, O. Estruch, A. Oliva, O. Lehmkuhl. Towards the high performance computing of molten salt tanks for CSP plants. In *Proceeding of the SolarPACES Congress*, 2012.

[11] R. Damle, O. Lehmkuhl, G. Colomer, I. Rodríguez. Energy simulation of buildings with a modular object-oriented tool. In *Proceedings of the ISES World Conference*, 2011.

[12] METEONORM 4.0. Meteotest Fabrikstrasse 14, CH-3012 Bern, Switzerland, 1999.

[13] R. Ferri, A. Cammi, D. Mazzei. Molten salt mixture properties in RELAP5 code for thermodynamic solar applications. *International Journal of Thermal Sciences*, 47:1676–1687, 2008.

[14] http://www.isover.es

[15] F.P. Incropera, D.P. DeWitt. Fundamentals of Heat and Mass Transfer, 4th ed., volume 10. John Wiley and Sons Inc., 1999.

[16] http://www.weber.es

[17] ACI Committee 207. Effect of restrain, volume change, and reinforcement on cracking of mass concrete. *Materials Journal*, 87:271–295, 1990.

[18] M.K Kassir, K.K Bandyopadhyay, M. Reich. Thermal degradation of concrete in the temperature range from ambient to 315 $^{\circ}C$ (600 $^{\circ}F$ Engineering research and applications division, Departament of Advanced Technology, Brookhaven National Laboratory, 1996.

Chapter 5

Conclusions and further work

5.1 Conclusions

The present thesis was focused on the numerical simulation of different sensible and latent thermal energy storage systems, considering a wide range of sizes, working conditions and industrial applications: from small size domestic drain water heat recovery storage units, and medium term low temperature accumulator prototype used in a in-space cryogenic propulsion systems, to big size two-tank thermal energy storage system in concentrating solar power (CSP) plants. Numerical tools were developed, adapted and implemented within a general purposes platform (NEST [1]) for their evaluation. Different levels of analysis have been carried out, i) within the field of Computational Fluid Dynamic and Heat Transfer (CFD&HT), the coupling between the heat conduction in solid parts and single flow/two phase flow 1D inside the tube, has allowed the accurate transient simulation of the complex heat transfer and fluid dynamics phenomena presented; ii) within thermal energy management, storage tank in CSP like a whole system has been studied; iii) it is interesting to highlight that numerical models have been experimental validated by mean of experimental results from the literature or with specific facilities carried out within the experimental infrastructure developed during this thesis for validation purposes.

In chapter 2, numerical and experimental tools have been used to design and study the performance of a specific drain water heat recovery storage-type. The device has been built and a experimental unit has been constructed. The experimental unit provides data to study the storage capacity and the delivering energy process of the DWHR storage device. The experiments have generated the data for the boundary conditions definition and results for validation of the numerical simulations. The numerical simulation has been performed within the NEST platform [1],where the different elements of the DWHR storage are linked to solve the system. The numerical simulation predict the transient behaviour of the DWHR storage system in the extraction process. A comparison between the numerical and experimental re-

sults has been carried out. The numerical results follow the transient evolution of the temperature correctly. However, the measured values in the upper sensor shows distinctly higher deviations between experiment and simulation. The author leave open the possibility of weaknesses of the numerical models and insufficient mesh refinement in the external boundaries and in the core of the tank. But in general, the numerical results show a good agreement with the experimental data. Different internal flow rates and operational temperatures have been studied. The DWHR storage had the capacity to recover from 60% - 34% of the energy available in the drain water for the investigated flow rates. A heat losses test was conducted on the insulated DWHR storage device, a 50% reduction in stored energy is observed at 24 h, which reveals its limitations for long-term storage applicability. This numerical platform will be applicable to future versions of DWHR storage (geometric configuration and operational condition).

In chapter 3, a methodology for the resolution of Computational Fluid Dynamics and Heat Transfer (CFD&HT) problems in a Low Temperature Accumulator (LTA) prototype of a Low Thrust Cryogenic Propulsion (LTCP) system is presented. The numerical model has been performed within the NEST platform [1]. Two numerical models have been adapted, one to solve the thermal and fluid-dynamic behaviour of the two-phase flow inside ducts working under cryogenic conditions, and another to solve the solid-liquid phase change phenomena using a fixed-grid enthalpy model developed by Galione et al. [2]. The thermal energy storage tank considered is formed by different elements: The two fluids (water and air) inside tank, the tube and the in-tube fluid (nitrogen), which interact with each other through their boundary conditions. Different combinations of single-phase/two-phase (evaporation) flow of the fluid (LN_2/N_2) inside the tube together with different combinations of single-phase (liquid water) / two-phase (water-ice, in process of freezing or melting) of the fluid inside the tank have been tested by DLR [3]. These experiments have been used for the validation of the models proposed. Overall, an acceptable agreement between experiments and numerical results was observed. In some tests, discrepancies were considered to be mainly due to not taking into account a temperature range for the phase change, break up of the ice and to not having very accurately boundary thermal conditions. From the experiments and the numerical simulation have been confirmed that mass flow rate has a significant influence on the flow patterns for cryogenic temperatures. The experimental validation under different working conditions of the cryogenic flow and/or the PCM material, shows the possibilities of this model for design optimization and prediction purposes of such type of devices.

In chapter 4, a numerical models for the simulation of the two-tank thermal energy storage system in concentrating solar power plants has been developed. The numerical simulation has been performed within the NEST platform [1]. A CSP

plant of 50MWe with solar power tower technology (located in Sevilla, Spain) was defined and adopted as reference. A numerical simulations in a realistic behaviour of the two-tank thermal energy storage system in concentrating solar power plants have been carried out. In order to present a parametric study of the hot storage tank for CSP plants. Three parameters have been considered for studying their effects on the performance of the storage system: meteorological data, insulation thickness of the storage tank and configuration of the foundation of the storage tank. The numerical simulations has been obtained for 1 year of operation. From the work by Rodríguez et al. [4] and the work presented in the chapter 4 has been developed an in-house software, called STEScode, with special agreements with the spin-off Termo Fluids S.L. [5], owner of the NEST platform. The STEScode is an interesting software for designing purposes and with a reasonable computational effort. And can also be of use in applications different from CSP.

As a final remark, this thesis has developed a methodology for the numerical simulation of different sensible and latent thermal energy storage systems. These virtual tools can be used for:

- Detailed thermal and fluid dynamic analysis of sensible TES systems for designing purposes, for example, have a sizing analysis.
- Energy analysis of the TES system, to have a basic understanding of how the TES system operates.
- Virtual test of a TES system under different working conditions.
- Thermoeconomic analysis of storage systems, where different control strategies for the thermal storage management can be proved, in order to identify potential cost saving.
- Prediction of transient behaviour of the TES system.

5.2 Further Work

Based on the numerical tools and experimental facilities now available, some future works can be carried out within each one of the storage unit developed:

On the drain water heat recovery storage unit application front, it will be worthwhile to address the following issues:

- Improvements in the mathematical model, with more accurate empirical inputs obtained from experiments and/or CFD simulations.
- Analysis of a new DWHR storage unit (dimensions, geometric configuration and operational condition).

- Improve in the insulation of experimental facilities of the DWHR storage unit in order to obtain a reduction of the heat loss, ii) complement the experimental measures in order to obtain more experimental data in the coiled pipe wall.
- Optimization of the proposed design of DWHR storage unit.

In this work the thermo-hydraulic behaviour of the Low Temperature Accumulator (LTA) prototype of a Low Thrust Cryogenic Propulsion (LTCP) has been presented. As a step further, to improve the simulation program, it will be interesting to take into account aspects like:

- Improvements in the mathematical model: the empirical correlations should be reviewed, including the rewetting temperature.
- Introduce the last available update tools developed by the CTTC researchers [6], for taking into account the change in density and other thermo-physical properties with the temperature and phase.

In reference to the two-tank thermal energy storage system in concentrating solar power (CSP),

- It would be necessary to implement a more complete models of the solar field and power block.
- Improvements in the empirical correlations.
- New materials (insulations and steels) should be added to the library of thermal properties.

Moreover, other thermal storage tanks used in different applications rather than the ones here presented can be studied, such as the small size of thermal ice storage system, the medium-big size of TES tanks that integrate chilled water district cooling system or at college campuses or resorts, government facilities, power plants, and industrial/commercial facilities, etc.

References

[1] R. Damle, O. Lehmkuhl, G. Colomer, I. Rodríguez. Energy simulation of buildings with a modular object-oriented tool. In *Proceedings of the ISES World Conference*, 2011.

[2] P.A. Galione, O. Lehmkuhl, J. Rigola, A. Oliva. Fixed-Grid Modeling of Solid-Liquid Phase Change in Unstructured Meshes Using Explicit Time Schemes. *Numerical Heat Transfer*, 65:27–52, 2014.

[3] J. Leiner, J. Riccius. Experimental investigation of phase-change behavior in a water-ice heat accumulator setup for cryogenic application. In *Proceedings of the Space Propulsion Conference*, 2012.

[4] I. Rodríguez, C.D. Pérez-Segarra, O. Lehmkuhl, A. Oliva. Modular object-oriented methodology for the resolution of molten salt storage tanks for CSP plants. *Applied Energy*, 109:402–414, 2013.

[5] Termo Fluids. Webpage: http://www.termofluids.com.

[6] P.A. Galione, O. Lehmkuhl, J. Rigola, A. Oliva. Fixed-grid numerical modeling of melting and solidification using variable thermo-physical properties – Application to the melting of n-Octadecane inside a spherical capsule. *International Journal of Heat and Mass Transfer*, 86:721–743, 2015.

Appendix A

STEScode

A.1 STEScode

The STEScode is one of the different products resulting from KIC InnoEnergy Tesconsol project (ref. 20_2011_IP16). The STEScode, allows the detailed thermal and fluid dynamic analysis of sensible TES systems for designing purposes and with a reasonable computational effort. Specifically, situations related to active or passive two-tank molten salts systems (the most common approach nowadays).

The engineering design of sensible TES system in CSP plants is a challenge due to the complex physical phenomena involved (unsteady behaviour, turbulent flows, radiation, interaction with mechanical issues, very large geometries which severely limit the possibilities of real life experiments, etc.). This is a problem of multidisciplinary character whose resolution involves complex couplings in the physical description of the system and the necessity of repeated computations (parametric studies) to get the optimum solution according to a specified target.

TES systems in CSP plants need an important effort to optimize existing commercial systems (specially two-tank direct or indirect storage), and to develop promising systems based on sensible storage in concrete, or other materials (for direct steam generation and also using molten salts as heat transfer fluid). The main goal is to develop more efficient and reliable systems from a thermal and also economic point of view.

Currently, the approach of the different players (component manufacturers, engineering companies, project developers, utilities, etc.) is based on trial-and-error analysis together with conservative designs (e.g. Andasol plant is replicated in many other plants with minor additional improvements).

Furthermore, experimental analyses are usually carried out on relatively small units where it is not possible to maintain the characteristic non-dimensional groups of the TES systems. The extrapolation (scale-up) to real life conditions of results obtained in small scale experiments is not immediate.

To improve current TES systems and to create new ones, reliable tools for designing are really needed. These will allow to reduce time-to-market of improved solution, with more reliable and optimized designs together with lower technical risks. The Tesconsol project has created the STEScode to give answer to these challenges.

To be useful for designers, the codes must be fast, e.g. it should allow the computation of many situations as quickly as possible. In this way, optimum solutions can be obtained based on parametric studies. This is a challenging problem that requires the use of different levels of analysis, from lumped models for the molten salt inside the tanks to detailed multidimensional simulation of the conduction heat transfer in the solid elements, and the analysis of the radiation exchange between the free molten salt surface (in case of two-tank systems) and the surroundings. The coupling of the different zones/phenomena in the framework of a global algorithm, where the designer can choose between different levels of analysis, is critical.

The numerical methodology is based on conservative finite volume methods and an object-oriented methodology. The advantages of this approach are:

- Any basic element programmed in a general way can be used in a given configuration and re-used in other systems (e.g. tank walls and insulation materials can be modelled with the same object).
- The elements which form a determined system interact only through their boundary conditions, being solved independently. This allows the direct substitution of a given model by another one (e.g. a one-dimensional approach by a three-dimensional approach), while the rest of the elements which form the system remains unchanged.
- Each element of a given system can be solved using a different parallelism paradigm without any need of re-writing any part of the code.

The main characteristics of these two innovative codes are:

- The code allows the analysis of the dynamics of the system (transient behaviour) under real working conditions.
- Conduction heat transfer can be described at the maximum level (multidimensional analysis with variable thermophysical properties).
- Fluid is characterized using lumped models (e.g. in two-tank systems).
- Fluid-solid interactions are characterized by local heat transfer coefficients and friction factors which are obtained from experiments and/or from advanced multidimensional computational studies (CFD&HT analysis using LES models for turbulent flow behaviour).

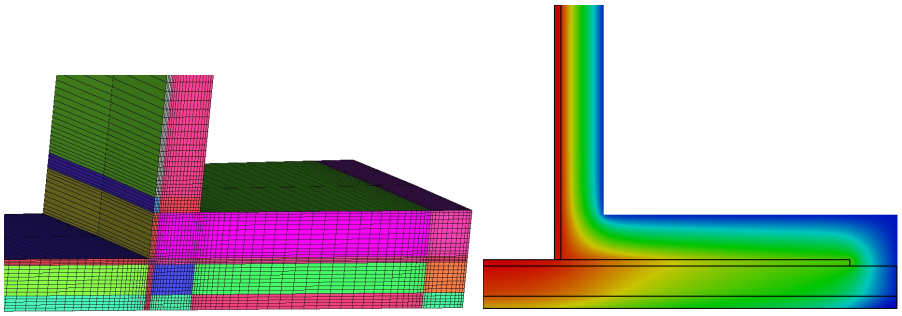

(a) (b)

Figure A.1: Multi-level approach in the tankshell: a) detail of the computational mesh used for the vertical walls, insulation materials and tank foundation; b) illustrative result.

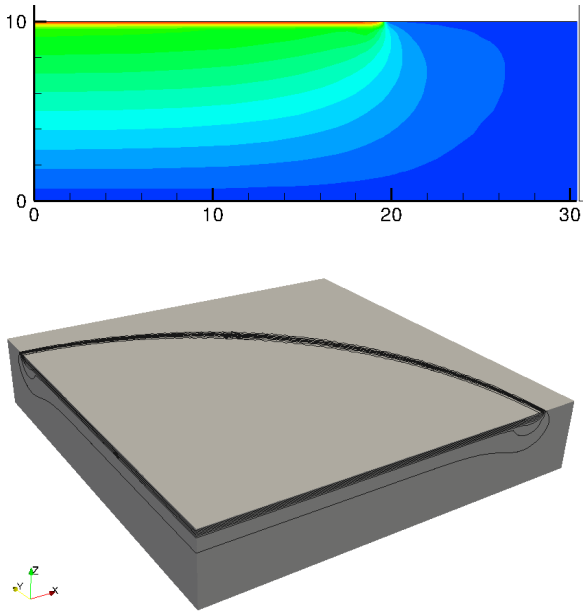

Figure A.2: Multi-level approach in the foundation: illustrative result a) with 2D simulation; b) with 3D simulation.

- Heat losses through the tank walls and insulation can be considered.
- A detailed analysis of the foundation (different materials, passive cooling, etc.) can be carried out;
- All the relevant fluid dynamic and thermal design aspects are considered (e.g. in two-tank systems, the gas ullage or the convection and radiation effects between the molten salt free surface and its surroundings);
- The parallel computational platform is based on NEST software.

The code has a friendly user interface. The code has been conceived as a web-based software for designing purposes.

The STEScode has been developed by the CTTC-UPC, with special agreements with the spin-off Termo Fluids S.L., owner of the Termofluids code and NEST platform.

As was mentioned before, the thermal and fluid dynamic analysis of TES systems in CSP plants is a challenging task due to the huge sizes of the tanks, working conditions (transient behaviour, high temperatures and high mass fluxes, etc.), significant investments, etc. To reduce risks, designers tend to be conservative and small improvements are introduced after several trial-and-error analysis.

The STEScode is focussed on the analysis at component level, where the input data must consider the detail of the system (size of the different elements, kind of materials and their mechanical and thermophysical properties, initial and boundary conditions, etc.).

A.1.1 A brief sample of the STEScode:

When the application is started, an introduction screen is presented to the user, together with the choice of the kind of simulation. It can be either a one tank simulation or a two tank simulation (see Fig. A.3).

The parameters that define the plant are structured into different sections. The parameters include meteorological data, the geometry of the tanks, the composition of the foundations below the tanks, salt and ullage conditions, and so on. Sane default values for the parameters are provided.

The Fig. A.4 shows the section to define the global parameters such as duration and accuracy of the simulation, initial time, add a brief description of the plant and the user can choose which plant model to simulate. There are currently three models, each with its own set of parameters.

The Fig. A.5 shows the outdoor conditions section to define the location, and the meteorological information. The outdoor conditions can be specified in two different ways: either using the application data base or specifying custom data.

Figure A.3: Front page of the STEScode and LTEScode.

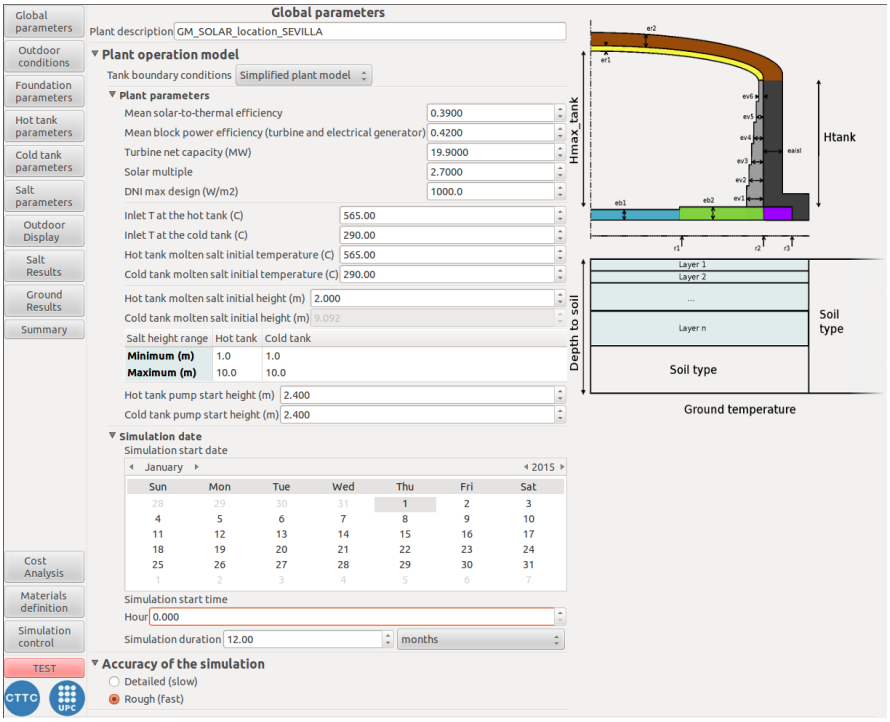

Figure A.4: View of the global parameters section in the STEScode. The model used for this view is the simplified plant model.

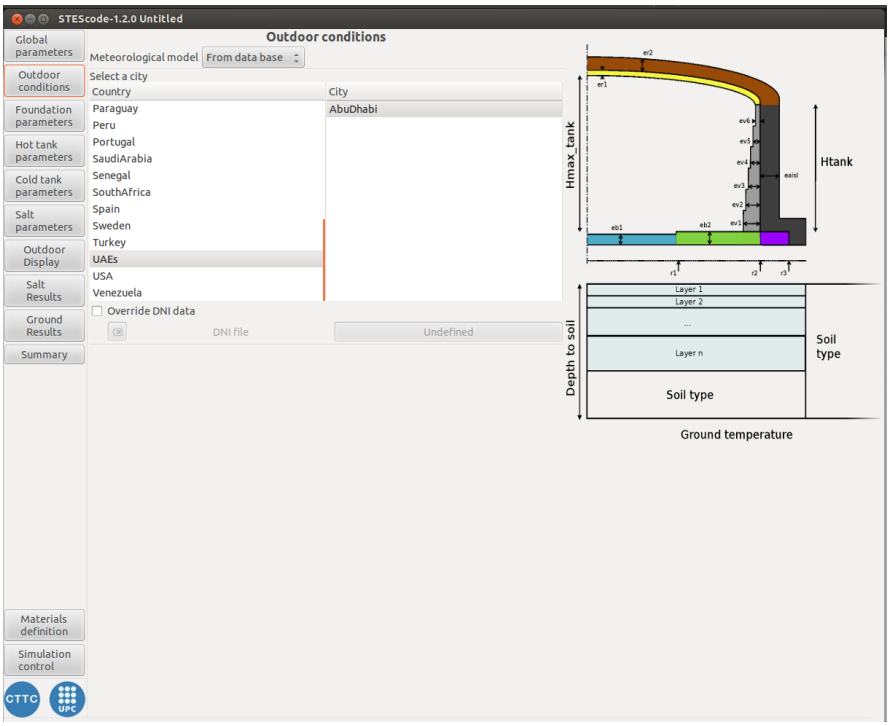

Figure A.5: View of the outdoor conditions section in the STEScode. The meteorological model used for this view is from the data base.

From data base: uses the meteorological data provided with the application, which is available from 77 locations from several countries. Data for the DNI in these locations is provided also, but can be overridden if the user has a specific DNI data which want to use in the simulation.

Custom data: the user can specify the location of the plant (longitude and latitude), the altitude and the time zone, and must provide the meteorological and DNI data files to be used for this location.

The Fig. A.6 shows the section to define the ground (foundation) parameters. It uses a one dimensional model; the ground below the tank can be divided in arbitrary number of layers, each with its own material and thickness. In this section is possible to select the surrounding material, the depth to the ground, and the temperature at this depth and set the soil thermal and solar reflectivity.

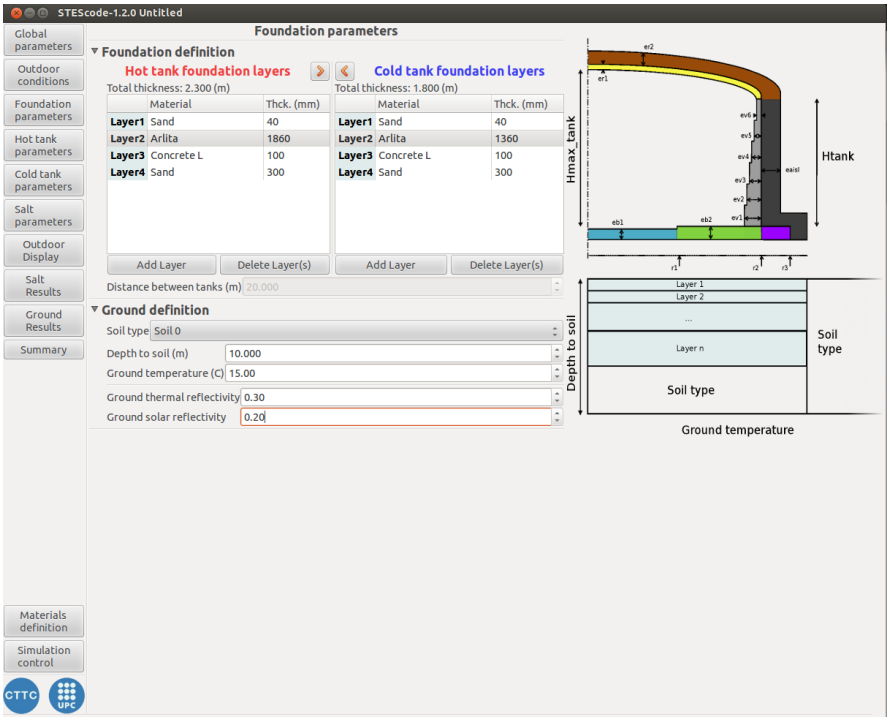

Figure A.6: View of the foundation section in the STEScode.

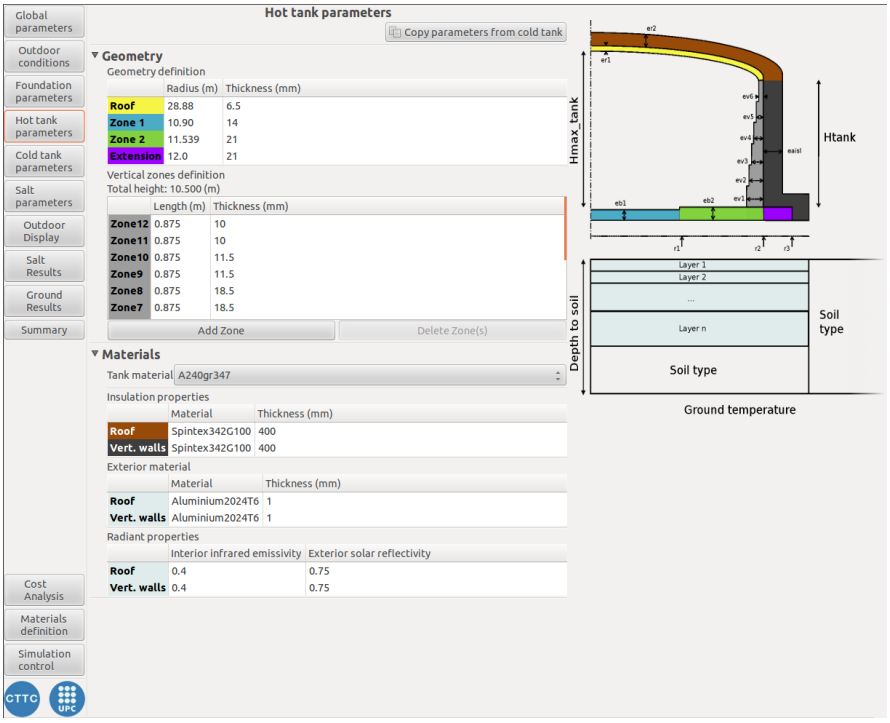

Figure A.7: View of the hot tank section in the STEScode.

The section to define the tank shell parameters is shown in Fig. A.7. The geometry of the tank can be specified, as well as the tank and insulation materials, dimensions, and radiative properties.

In the salt parameters section the interior of the tank is modelled. It is composed by the molten salt and the air above it. Some parameters are defined (see Fig. A.8).

The STEScode user interface (UI) comes with a set of predefined solid and fluid materials. In the case that the use of other materials is required, the user can define new materials in the material definition section. There is room for two kinds of materials: solid and fluid. Solid materials are used in structural elements, while any fluid material can be used as the molten salt. Each material is defined by giving its thermophysical properties.

There is also the possibility of importing the thermal properties from an external. To that effect, click on the Import solid properties from CSV file button, or its

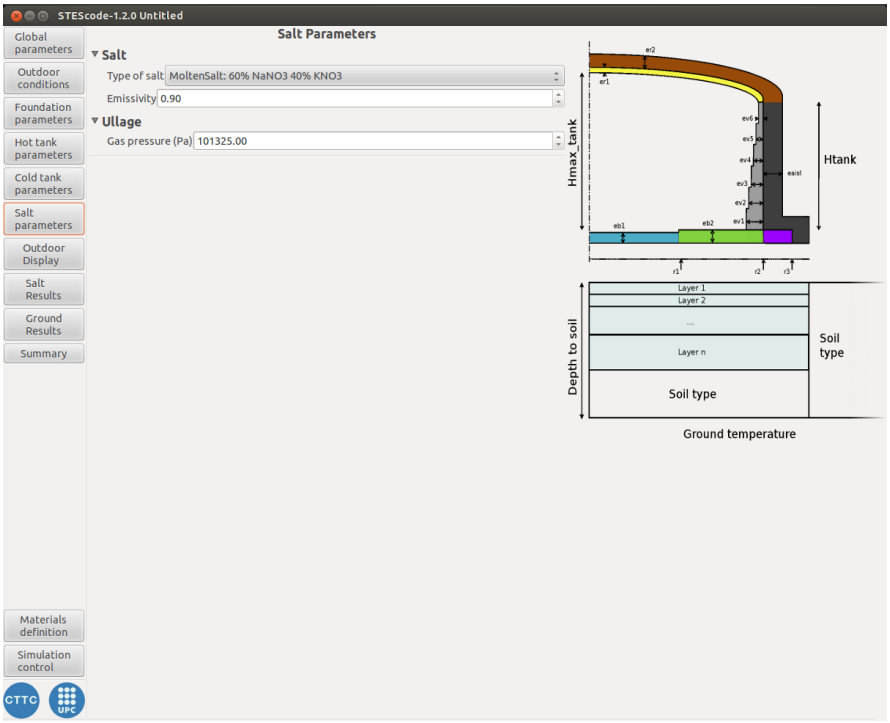

Figure A.8: View of the salt parameters section in the STEScode.

analogous for fluid materials.

When a material is defined, it will be immediately made available to the other sections of the UI where a material is requested. These sections are the ground, tank and salt parameters.

The simulation control section is used to manage the different simulations that the user has sent to the calculation server. In this section is can be seen a list with with current and finished jobs (pending download). Several actions can be performed on the currently selected job, with the action buttons:

- Update, the simulation progress information.
- Cancel the job (remove from execution queue).
- Delete the job (remove from server once it has finished)
- Download data (will be removed from the server automatically)

If the Start simulation buttons are not clickable, it means that the current plant has not been saved, or that there isn't any plant loaded, or that there are several parameters missing or inconsistently set. If this is the case, a list of found problems will appear in this screen just on top of the Start simulation button. When the reported errors are solved the user will be able to send the simulation to the server.

The relevant results in the STEScode have been divided in different sections: outdoor, salt, and ground data.

In the outdoor display, the meteorological and DNI data that were used as input conditions in the simulation are shown in Fig. A.9. The meteorological data include the ambient temperature, the humidity, and the wind speed and direction.

In the salt result section, the data is further divided into four zones displaying temperature, height, mass flow, and power data. The Fig. A.10 shows the most relevant results for the molten salt.

For both the one and two tank simulations, the displayed variables are the same, but in the case of the two tank the amount of displayed information is of course doubled.

In the ground results section, the heat transfer between the ground and different zones are plotted. Also the temperature map of the ground below the tank is shown (see Fig. A.11).

The summary section has been added in the last version of the STEScode. There is a section that summarizes the data obtained in the simulation. It shows several columns of day averaged magnitudes, organized in three groups: Outdoor, Salt, and Ground. It is possible to further narrow the display range (interval) by grouping days into weeks, months or years, or any number of days in between (see Fig. A.12).

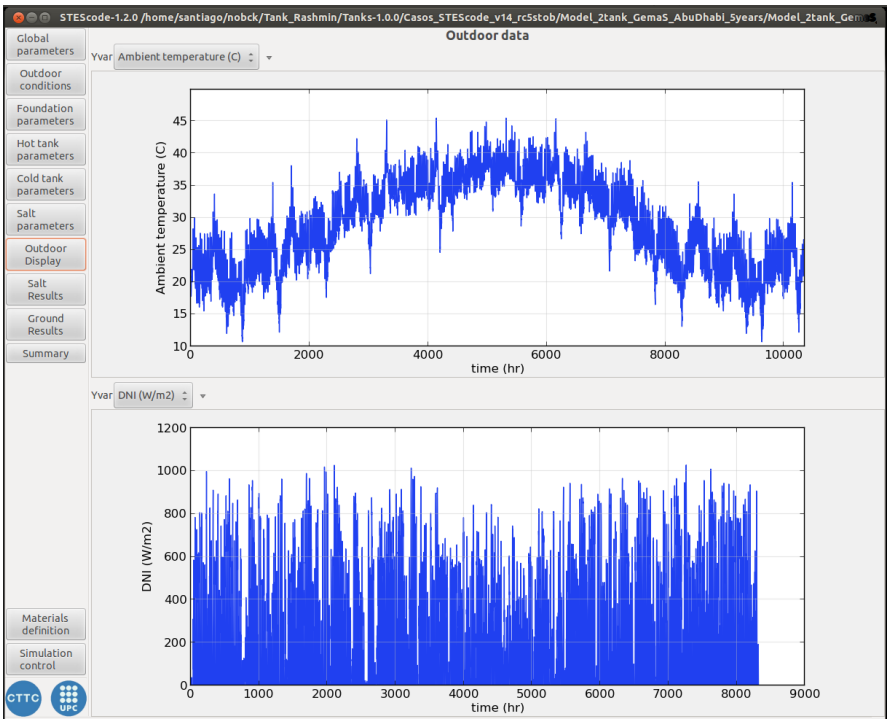

Figure A.9: View of the outdoor display in the STEScode.

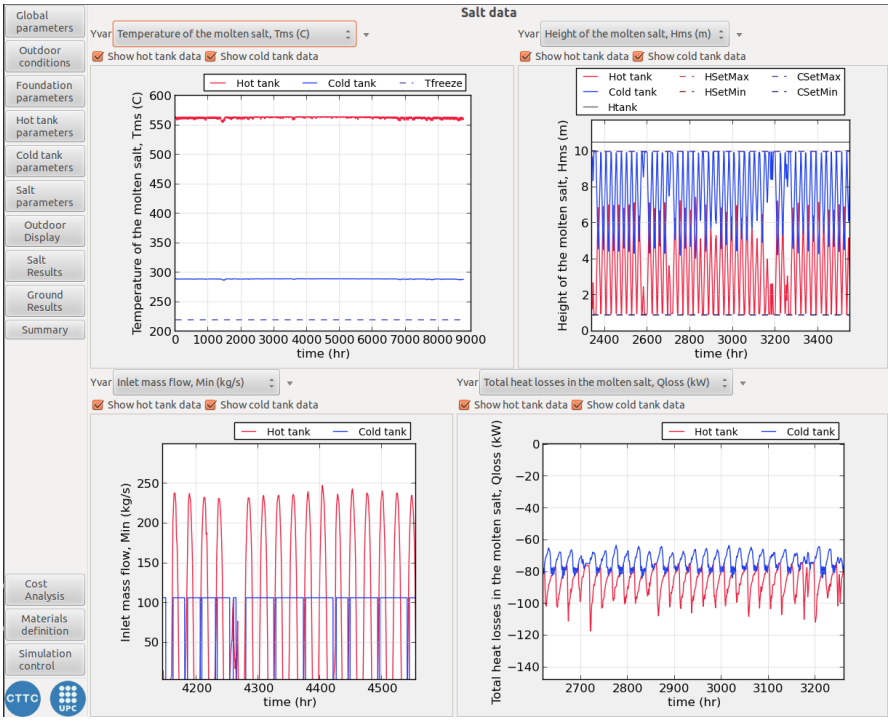

Figure A.10: View of the salt results section in the STEScode.

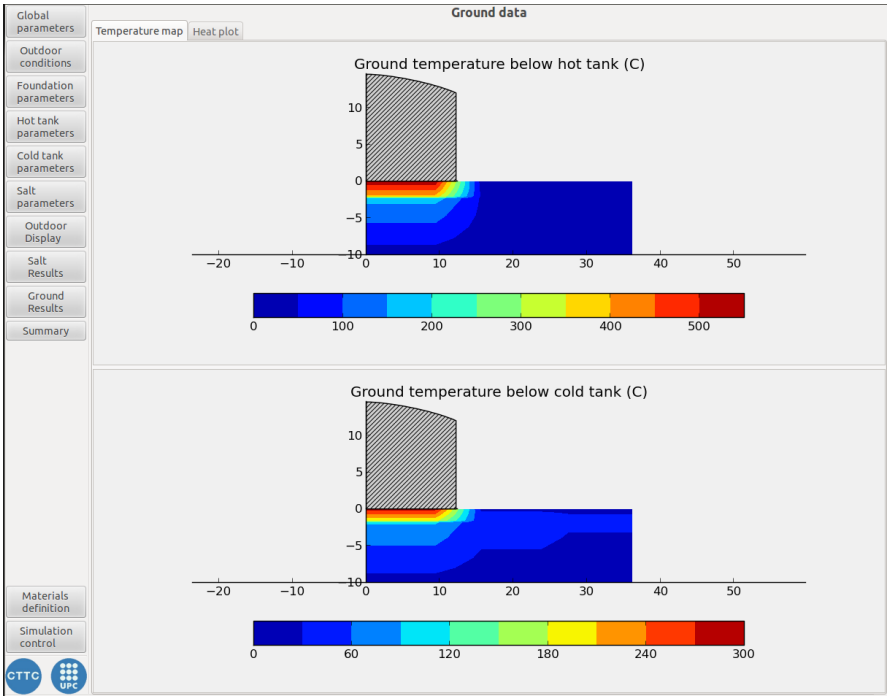

Figure A.11: View of the ground results section in the STEScode.

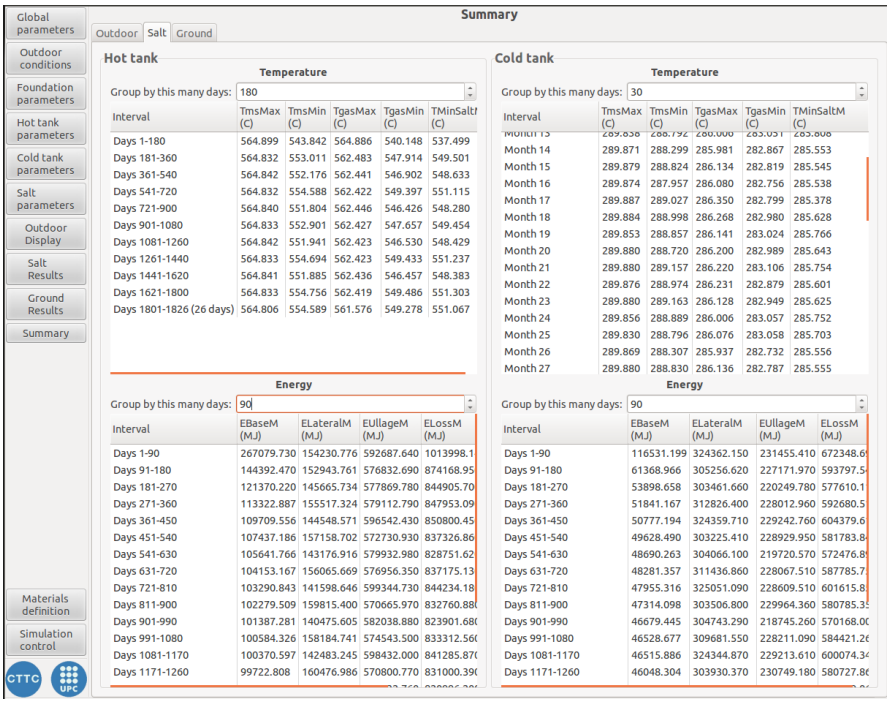

Figure A.12: View of the salt summary in the STEScode.

Appendix B

Main publications in the context of this thesis

International Journal Papers:

- S. Torras, C.D. Pérez-Segarra, I. Rodríguez, J. Rigola and A. Oliva. Parametric study of two-tank TES systems for CSP plants. *Energy Procedia*, 69:1049–1058, 2015.
- P. Galione, C.D. Pérez-Segarra, I. Rodríguez, S. Torras and J. Rigola. Numerical Evaluation of Multi-layered Solid-PCM Thermocline-like Tanks as Thermal Energy Storage Systems for CSP Applications. *Energy Procedia*, 69:832–841, 2015.
- P. A. Galione, C.D. Pérez-Segarra, I. Rodríguez, S. Torras and J. Rigola. Multi-layered solid-PCM thermocline thermal storage for CSP. Numerical evaluation of its application in a 50MWe plant. *Solar Energy*, 19:134–150, 2015.

International Conference Papers:

- S. Torras, O. Lehmkuhl, J. Rigola and A. Oliva. Numerical simulation of heat storage for domestic applications. In *Proceedings of the 23rd IIR International Congress of Refrigeration*, Prague, Czech Republic, 2011.
- A. Oliva, C.D. Pérez-Segarra, I. Rodríguez, O. Lehmkuhl and S. Torras. Modular object-oriented methodology for the resolution of molten salt storage tanks for CSP plants. In *Proceedings of the 12th International Conference on Energy Storage (Innostock 2012)*, Lleida, Spain, 2012.
- C.D. Pérez-Segarra, I. Rodríguez, A. Oliva, S. Torras and O. Lehmkuhl. Detailed numerical model for the resolution of molten salt storage tanks for CSP Plants. In *Proceedings of the ISES Europe Solar Conference (EuroSun 2012)*, Rijeka, Croatia, 2012.

- S. Torras, C. Oliet, O. Lehmkuhl and J. Rigola. Numerical Simulation and Experimental Validation of Sensible Heat Accumulators Oriented to Zero Energy Buildings. In *Proceedings of the 11th REHVA World Congress & 8th International Conference on IAQVEC (CLIMA 2013)*, Prague, Czech Republic, 2013.

- S. Torras, J. Castro, J. Rigola, S. Morales, J. Riccius, J. Leiner. Modelling and experimental validation of the heat accumulator in a low thrust cryogenic propulsion (LTCP) system. In *Proceedings of the 5th European Conference For Aerospace Sciences (EUCASS)*, Munich, Germany, 2013.

- S. Torras, J. Castro, J. Rigola, S. Morales, P. Galione, O. Lehmkuhl and A. Oliva. Numerical modeling and experimental validation of thermal energy storage tanks for propulsion system under cryogenic conditions. In *Proceedings of the Eurotherm Seminar #99 – Advances in Thermal Energy Storage*, Lleida, Spain, 2014.

- S. Torras, C.D. Pérez-Segarra, I. Rodríguez, J. Rigola and A. Oliva. Parametric study of two-tank TES systems for CSP plants. In *Proceedings of the SolarPACES 2014 International Conference*, Beijing, China, 2014.

- P. Galione, C.D. Pérez-Segarra, I. Rodríguez, S. Torras and J. Rigola. Numerical Evaluation of Multi-layered Solid-PCM Thermocline-like Tanks as Thermal Energy Storage Systems for CSP Applications. In *Proceedings of the SolarPACES 2014 International Conference*, Beijing, China, 2014.